Cell

m^{6}A-modified cenRNA stabilizes CENPA to ensure centromere integrity in cancer cells

Graphical abstract

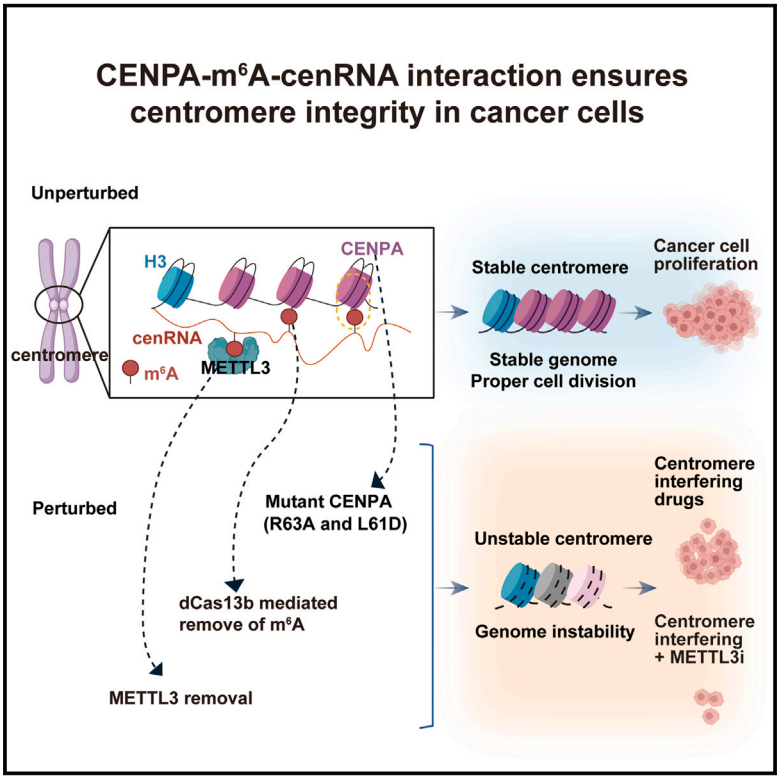

Highlights

- m^{6}A modifications on centromeric RNA (cenRNA) are elevated in cancer cells
- CENPA binding to m^{6}A-cenRNA ensures its centromere association during S phase
- The CENPA residues Leu61 and Arg63 mediate its interaction with m^{6}A-cenRNA
- Disruption of the CENPA-m^{6}A-cenRNA interaction impairs cancer cell centromere integrity

Authors

Zihong Kang, Ruimeng Li, Chang Liu, ..., Huan Wang, Xuerui Yang, Jun Liu

Correspondence

yangxuerui@tsinghua.edu.cn (X.Y.), junliu1223@pku.edu.cn (J.L.)

In brief

CENPA is an m^{6}A reader with specificity for m^{6}A-modified centromeric RNA. The CENPA-centromeric RNA interaction ensures centromere integrity and proliferation in cancer cells.

Kang et al., 2024, Cell *187*, 6035–6054
October 17, 2024
https://doi.org/10.1016/j.cell.2024.08.040

CellPress

Cell

CellPress

Article

m^{6}A-modified cenRNA stabilizes CENPA to ensure centromere integrity in cancer cells

Zihong Kang,[1,2,11] Ruimeng Li,[3,11] Chang Liu,[4] Xiaozhe Dong,[5] Yuxuan Hu,[6] Lei Xu,[7] Xinyu Liu,[1,2] Yunfan Xiang,[1,2] Liming Gao,[8] Wenzhe Si,[9] Lei Wang,[7] Qing Li,[1] Liang Zhang,[10] Huan Wang,[5] Xuerui Yang,[3,*] and Jun Liu[1,2,12,*]

[1]State Key Laboratory of Protein and Plant Gene Research, School of Life Sciences, Peking-Tsinghua Center for Life Sciences, Peking University, 100871 Beijing, China

[2]Beijing Advanced Center of RNA Biology (BEACON), Peking University, Beijing, China

[3]MOE Key Laboratory of Bioinformatics, Center for Synthetic & Systems Biology, School of Life Sciences, Joint Graduate Program of Peking-Tsinghua-National Institute of Biological Science, Tsinghua University, 100084 Beijing, China

[4]Department of Genetics, Stanford University, School of Medicine, Stanford, CA, USA

[5]College of Chemistry and Molecular Engineering, Peking University, 100871 Beijing, China

[6]State Key Laboratory of Natural Medicines, China Pharmaceutical University, 211198 Nanjing, China

[7]Department of Gastroenterology, Nanjing Drum Tower Hospital, The Affiliated Hospital of Nanjing University Medical School, 210008 Nanjing, China

[8]School of Science, China Pharmaceutical University, 211198 Nanjing, China

[9]State Key Laboratory of Vascular Homeostasis and Remodeling, Department of Laboratory Medicine, Peking University Third Hospital, 100191 Beijing, China

[10]Hangzhou Institute of Medicine (HIM), Chinese Academy of Sciences, 310022 Hangzhou, China

[11]These authors contributed equally

[12]Lead contact

*Correspondence: yangxuerui@tsinghua.edu.cn (X.Y.), junliu1223@pku.edu.cn (J.L.)

https://doi.org/10.1016/j.cell.2024.08.040

SUMMARY

m^{6}A modification is best known for its critical role in controlling multiple post-transcriptional processes of the mRNAs. Here, we discovered elevated levels of m^{6}A modification on centromeric RNA (cenRNA) in cancerous cells compared with non-cancerous cells. We then identified CENPA, an H3 variant, as an m^{6}A reader of cenRNA. CENPA is localized at centromeres and is essential in preserving centromere integrity and function during mitosis. The m^{6}A-modified cenRNA stabilizes centromeric localization of CENPA in cancer cells during the S phase of the cell cycle. Mutations of CENPA at the Leu61 and the Arg63 or removal of cenRNA m^{6}A modification lead to loss of centromere-bound CENPA during S phase. This in turn results in compromised centromere integrity and abnormal chromosome separation and hinders cancer cell proliferation and tumor growth. Our findings unveil an m^{6}A reading mechanism by CENPA that epigenetically governs centromere integrity in cancer cells, providing potential targets for cancer therapy.

INTRODUCTION

Centromeres serve as assembly sites for kinetochores and facilitate the interaction between microtubules of the mitotic spindle and sister chromatids, ensuring faithful distribution of chromosomes and cell viability.[1,2] Therefore, disruption of centromere integrity can lead to the rapid accumulation of mis-segregated chromosomes, producing aneuploidy, a hallmark of cancer cells.[3,4] Eukaryotic centromere-specific nucleosomes are distinguished by the histone H3 variant centromere protein A (CENPA).[5–7] Alterations in CENPA levels can influence the assembly of CENPA nucleosomes and centromere functionality.[8–11] Studies have shown that the deposition and maintenance of CENPA in chromatin are controlled in a highly sophisticated manner.[12,13] Unlike the canonical histone H3 that gets incorporated into nucleosomes in S phase of the cell cycle, CENPA is incorporated into nucleosomes in early G1 phase, independently of DNA replication. During the S phase when DNA replication takes place, CENPA is distributed on both the newly synthesized and the parental DNA strands, whereas Histone H3.3 fills the interim nucleosome vacancies.[14,15] Throughout this dynamic process, CENPA nucleosomes exhibit remarkable stability, implying refined machinery for CENPA maintenance.[16,17] While the machinery for CENPA deposition has been extensively elucidated,[18–21] the mechanisms controlling CENPA maintenance at S phase and the reliable transmission of such epigenetic signals during DNA replication remain obscure.

Previous research has unveiled the transcription activation in centromere regions and highlighted the role of transcription-mediated chromatin remodeling in CENPA loading and centromere stability.[22–26] However, it remains unclear how the CENPA

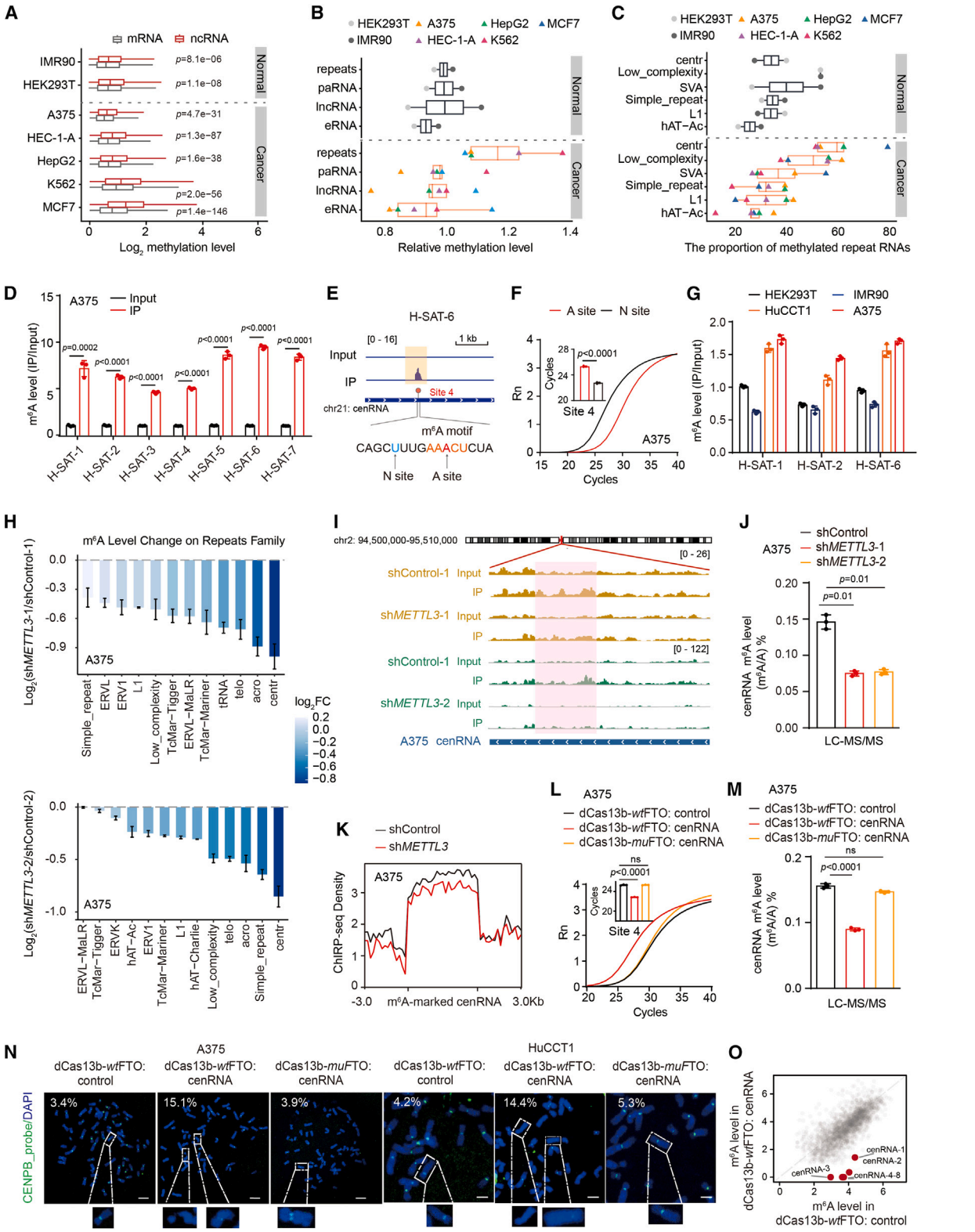

Figure 1. m^{6}A-marked centromeric RNA promotes centromeric stability

(A) The methylation levels of coding RNA and ncRNA in five cancer and two normal cell lines using non-ribosomal chromatin-associated RNA (caRNA) MeRIP-seq datasets (STAR Methods). *p* values were calculated by Wilcoxon test.

(legend continued on next page)

nucleosomes remain centromere-bound during mitosis and accommodate the passage of elongating RNA polymerase II (-RNAPII) during transcription. Cells from multiple tumor types exhibit intrinsic fragility of centromeres; intriguingly, the latter is accompanied by excessive expression of centromeric RNA (cenRNA), which correlates with cancer development and progression.[27–29] Whether and how the elevated cenRNA expression impacts centromere integrity in cancer cells remains elusive.

Recently, RNA N^6-methyladenosine (m^6A) modification has emerged as a key regulator of RNA-related molecular and cellular processes under various physiological contexts. Previous studies have firmly established the critical roles of m^6A modification on mRNAs in almost all steps of mRNA processes, including pre-mRNA processing, degradation, and translation.[30–33] Here, we found that cenRNAs harbor m^6A modification and that its abundance is notably elevated in various cancer cells. Moreover, we demonstrate that CENPA serves as an m^6A reader of cenRNAs, which ensures the retention of CENPA in the centromeric regions during S phase of the cell cycle. The interplay between CENPA and cenRNA methylation facilitates centromere integrity, serving as a critical post-transcriptional mechanism for proper mitosis in cancer cells. In summary, our study has revealed a previously unrecognized role of CENPA, a histone protein and an epigenetic marker, serving as an m^6A reader and playing roles in orchestrating centromere integrity during mitosis, specifically in cancer cells. This CENPA-cenRNA methylation axis could represent an additional aspect of cancer progression, opening up avenues for strategies in cancer therapy.

RESULTS

Elevated m^6A modification on cenRNA is vital for centromere stability in cancer cells

Through a comprehensive analysis of m^6A-methylated RNA immunoprecipitation (IP) sequencing (MeRIP-seq) datasets for chromatin-associated RNAs (caRNAs), we compared the methylation levels of diverse RNA species across five cancer cells (A375, HEC-1-A, HepG2, K562, and MCF7) and two normal cell types (IMR90 and HEK293T).[34–37] Notably, we observed that non-coding RNAs (ncRNAs) displayed relatively higher levels of m^6A methylation compared with coding RNAs within each of the normal and cancer cell lines (Figure 1A). Among these ncRNAs, repeat RNAs exhibited a notably elevated m^6A level (Figure 1B). Specifically, cenRNAs exhibited a higher prevalence (Figure 1C) and overall level (Figure S1A) of m^6A modifications. However, these patterns were unidentified in the two normal cell lines (Figures 1B, 1C, and S1A). Remarkably, approximately 60% of cenRNA species were modified in cancer cell lines, substantially higher than in normal cell lines (Figure 1C).

Based on the MeRIP-seq datasets, the methylated cenRNA peaks enriched GAC and AAC motifs and were relatively conserved across different cell lines (Figures S1B and S1C). Next, m^6A IP (m^6A-IP) followed by RT-qPCR confirmed methylation enrichment on cenRNAs in A375 and HuCCT1 cells (Figures 1D, 1E, S1D, and S1E). We also applied single-base elongation- and ligation-based qPCR amplification (SELECT),[38] which verified m^6A modifications at single-base resolution on specific cenRNAs in these two cell types (Figures 1F, S1F, and S1G). Both assays corroborated the comparatively higher m^6A level of cenRNAs in these two cancer cells relative to the two normal cells (Figures 1G and S1H), indicating a potential role of cenRNA methylation in cancer cells.

As METTL3 is responsible for m^6A installation, we generated two *METTL3* knockdown A375 cells using different shRNAs (Figure S1I). MeRIP-seq analysis revealed predominant hypomethylation of m^6A peaks on caRNAs upon *METTL3* knockdown, which was further supported by liquid chromatography-tandem mass spectrometry (LC-MS/MS) analysis (Figures S1J–S1L). We then ranked the repeat families based on their m^6A level changes upon *METTL3* knockdown, and cenRNA illustrated the most

(B) The relative methylation levels of repeat RNAs (repeats), promoter-associated RNA (paRNAs), enhancer RNAs (eRNAs), and long non-coding RNAs (lncRNAs) in seven cells (STAR Methods). RNA species were ranked based on the mean relative methylation levels in five cancer cell lines. Triangles: cancer cells. Dots: normal cells.
(C) The top six repeat families, from top to bottom ordered by the mean proportion of methylated repeat RNAs (m^6A enrichment $\log_2$[IP/input] > 0.58) of each repeat family in five cancer cells (STAR Methods). Triangles: cancer cells. Dots: normal cells.
(D) The methylation levels of cenRNA were assessed using distinct primers via MeRIP-qPCR in A375 cells ($n = 3$).
(E) m^6A sites and the cenRNA sequences referenced for designing the corresponding primers.
(F) The results of single-base elongation- and ligation-based qPCR amplification (SELECT) for the detection of the cenRNA m^6A site at single-base resolution in A375 cells. "A site" denotes the m^6A site, "N site" represents a non-m^6A-modified site ($n = 3$).
(G) The methylation levels of cenRNA were assessed using 3 distinct primers via MeRIP-qPCR in HEK293T, IMR90, HuCCT1, and A375 cell lines ($n = 3$).
(H) Repeats families (x axis) ranked by m^6A level $\log_2$fold-change (y axis) upon *METTL3* knockdown ($n = 2$).
(I) A representative cenRNA with hypo-methylated peaks (m^6A $\log_2$FoldChange < −0.58) following *METTL3* knockdown in A375 cells.
(J) LC-MS/MS analysis of the m^6A/A ratio in cenRNAs obtained from chromatin isolation by RNA purification (ChIRP) of A375 cells upon *METTL3* knockdown ($n = 3$).
(K) A decreased enrichment over regions marked by m^6A-modified cenRNAs upon *METTL3* knockdown in A375 cells, based on cenRNA ChIRP followed by high-throughput DNA sequencing (ChIRP-seq).
(L) The demethylation efficiency of cenRNA upon dCas13b-FTO treatment by SELECT assay ($n = 3$).
(M) LC-MS/MS analysis of the m^6A/A ratio in cenRNAs obtained from ChIRP of A375 cells upon dCas13b-FTO treatment ($n = 3$).
(N) Representative images of metaphase spread upon dCas13b-FTO treatment in A375 and HuCCT1 cells, with fluorescence *in situ* hybridization (FISH) using centromeric (PNA-green) probes. The enlarged sections show lost and ectopic centromeres. Scale bar, 5 μm.
(O) m^6A methylation level changes upon dCas13b-FTO treatment in A375 cells quantified by MeRIP-seq. Red dots indicate significantly demethylated m^6A peaks ($\log_2$FoldChange < −2.9).
Error bars indicate mean ± SEM (D, F–H, J, L, and M). ns, not significant (L and M).
See also Figure S1.

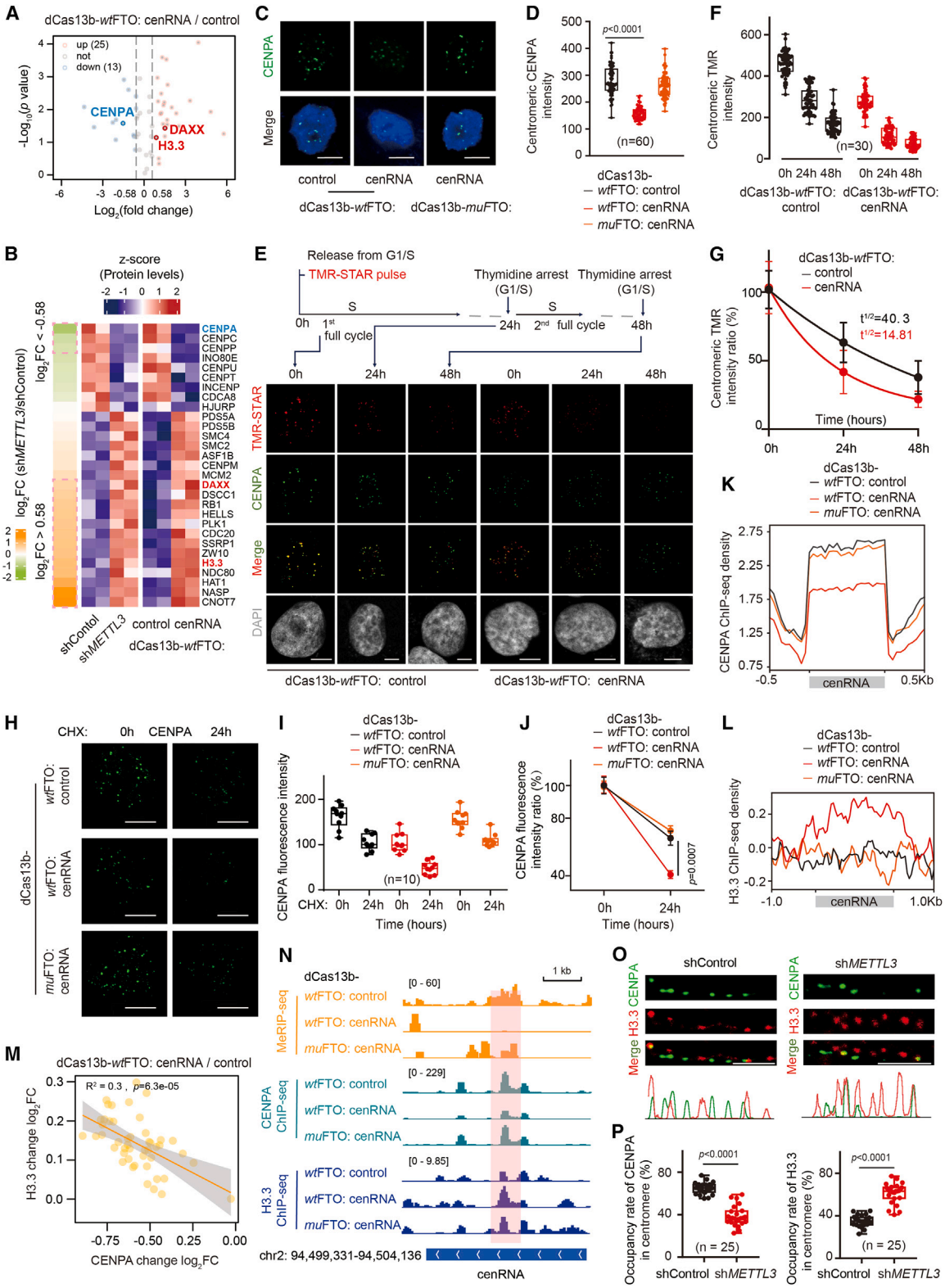

Figure 2. cenRNA methylation stabilizes CENPA maintenance during the S stage

(A) The changes in protein levels upon dCas13b-FTO treatment in A375 cells, quantified by mass spectrometry profiling of the chromatin-enriched proteome. Up in red: log_2FoldChange > 0.58; down in blue: log_2FoldChange < −0.58.

(legend continued on next page)

pronounced reduction in methylation level (Figures 1H and 1I). This was confirmed using MeRIP-qPCR in both A375 and HuCCT1 cells (Figures S1M–S1O). Furthermore, we performed chromatin isolation by RNA purification (ChIRP)[39] to enrich cenRNAs with high efficiency (Figures S1P and S1Q) in A375 cells. Indeed, the following LC-MS/MS exhibited a remarkable reduction in cenRNA methylation levels upon *METTL3* knockdown, demonstrating the critical role of METTL3 in implementing cenRNA methylation (Figure 1J).

To confirm the observed cenRNA methylation occurs at centromere regions, we applied ChIRP to cenRNAs followed by high-throughput DNA sequencing in A375 cells. cenRNAs were verified to be associated with centromeric regions (Figures S1R and S1S), aligning with previous reports of the close association between centromeric loci and their transcribed cenRNAs.[22] Notably, the chromatin binding of cenRNA exhibited a significant reduction at its m^{6}A-modified regions upon *METTL3* knockdown, indicating that METTL3 regulates the chromatin association of methylated cenRNAs within centromere regions (Figure 1K).

cenRNA is involved in regulating centromere stability and function[22]; however, the molecular mechanism remains unclear. Here, we looked into whether this function of cenRNA depends on its highly enriched m^{6}A modification. Notably, we observed remarkable increase in frequency of chromosomal translocations and centromere breaks upon *METTL3* knockdown in both A375 and HuCCT1 cells (Figures S1T and S1U). To further examine whether this is mediated specifically by cenRNA methylation, we took advantage of the CRISPR-dCas13b-FTO system with the dCas13b-*mu*FTO (catalytic-inactive mutant) as a negative control (Figure S1V).[36,40–43] Highly specific guide RNAs (gRNAs) were designed to target the consensus sequence of cenRNAs in A375 and HuCCT1 cell lines. Consistently, we only observed increased chromosomal aberrations with dCas13b-*wt*FTO, along with a substantial decrease in m^{6}A level of the targeted cenRNA, but not with dCas13b-*mu*FTO (Figures 1L–1N and S1W). MeRIP-seq confirmed significantly reduced m^{6}A on cenRNAs targeted by dCas13b-FTO (Figures 1O and S1X) without global methylation changes (also confirmed by LC-MS/MS, Figure S1Y), indicating limited off-target effects. Taken together, these results indicated a critical role of cenRNA methylation in maintaining centromere stability.

cenRNA methylation stabilizes CENPA maintenance during the S phase of the cell cycle

To investigate how chromatin-bound cenRNA m^{6}A affects centromeric stability, we applied a crosslinking-based method to capture the chromatin-associated proteins in control and *METTL3* knockdown A375 cells.[44] We focused on chromatin-associated proteins, which are functionally annotated as histone chaperones,[45] proteins related to centromere complex assembly or chromosome segregation. Intriguingly, among the four proteins exhibiting significant reductions in chromatin binding upon *METTL3* knockdown, three were involved in centromere complex assembly, with CENPA as top hit (Figure S2A). We then examined the chromatin-bound proteins in cells treated with dCas13b-FTO and observed significantly reduced CENPA binding (Figure 2A), together with a pattern of differential protein binding comparable to that with *METTL3* knockdown, underscoring the role of cenRNA methylation in preserving chromatin binding of these proteins (Figure 2B). Fluorescence immunology analysis further demonstrated reduced CENPA within the centromeric loci in A375 cells following *METTL3* knockdown (Figures S2B and S2C) and dCas13b-*wt*FTO targeting (Figures 2C and 2D).

We next applied SnapTag ligand (SNAP-Cell TMR-STAR) system to determine whether the observed CENPA reduction resulted from changes in CENPA synthesis during the G1 phase or its maintenance during the S phase.[10,46] Following the initiating of two complete cell cycles from G1/S blockade, we detected an apparent unsustainable CENPA maintenance during S phase in *METTL3* knockdown A375 and HuCCT1 cells, while the CENPA deposition during early G1 phase remained unchanged (Figures S2D–S2J). Similar effects were observed

(B) The changes in protein levels upon *METTL3* knockdown or dCas13b-FTO treatment in A375 cells, quantified by mass spectrometry profiling of the chromatin-enriched proteome. The leftmost column shows the fold change of protein levels upon *METTL3* knockdown. The dotted pink boxes indicate the differential chromatin-binding proteins.

(C and D) CENPA fluorescence intensity upon dCas13b-FTO treatment in A375 cells was examined by immunofluorescence staining (C) and quantified using ImageJ (D).

(E–G) Cells were synchronized and labeled with SNAP-tagged CENPA (red), total CENPA (green) upon dCas13b-FTO treatment in A375 cells (E). The fluorescence intensity of SNAP-tagged CENPA was quantified using ImageJ (F), and the corresponding degradation rate was calculated and fitted the curves using GraphPad prism (G).

(H–J) CENPA fluorescence intensity upon dCas13b-FTO treatment in A375 cells followed by CHX (5 μg/mL) treatment at different time points was examined. The ratio at 24 h relative to 0 h was calculated using GraphPad prism (J).

(K and L) The enrichment of CENPA (K) and histone H3.3 (L) at methylated cenRNA-expressing loci upon dCas13b-FTO treatment in A375 cells.

(M) The correlation between changes in CENPA binding and changes in histone H3.3 binding at methylated cenRNA-expressing loci upon dCas13b-FTO treatment in A375 cells. These loci were categorized into 50 groups based on the rank of fold change in CENPA binding level upon dCas13b-FTO treatment. R refers to Pearson's correlation coefficient.

(N) The changes in m^{6}A levels, CENPA binding, and histone H3.3 binding within the genomic location encoding a representative cenRNA upon dCas13b-FTO treatment in A375 cells.

(O and P) Chromatin fibers showing the replication of CENPA and histone H3.3 at centromeres. The fibers were labeled with an anti-CENPA (green) and an anti-H3.3 (red). Line plots below depict the relative intensity of CENPA and histone H3.3 along the centromere track (O), and the occupancy rate was quantified by ImageJ (P).

The "*n*" shown in the figures represents the total number of cells randomly selected and used for quantifications (D, F, I, and P). Scale bar: 5 μm in (C), (E), (H) and (O). Error bars indicate mean ± SEM (G and J).

See also Figure S2.

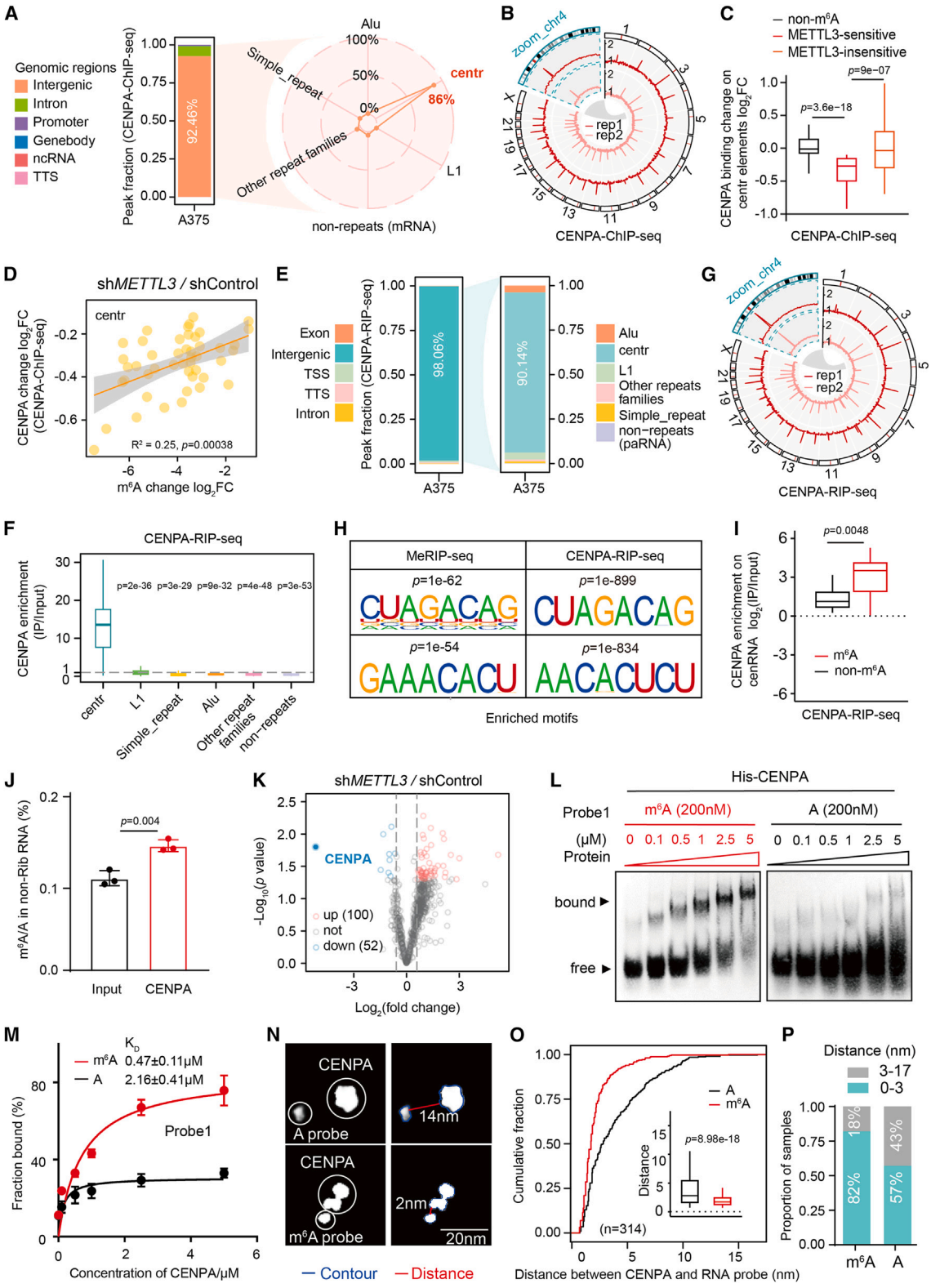

Figure 3. CENPA propensity to bind to m^{6}A-methylated cenRNA

(A) The bar and radar plot showing the fraction of CENPA peaks at distinct genomic regions and regions expressing distinct well-defined RNA species in A375 cells, respectively.

(legend continued on next page)

when cenRNA methylation was targeted by dCas13b-*wt*FTO (Figures 2E–2G). Additionally, we treated A375 cells with cycloheximide (CHX) to inhibit protein synthesis. We observed a more substantially reduced CENPA abundance at the S phase following *METTL3* knockdown or dCas13b-*wt*FTO targeting, again demonstrating the function of cenRNA methylation on the maintenance of CENPA (Figures 2H–2J and S2K–S2M).

Alongside with decreased CENPA in chromatin-enriched proteome, we identified increased histone H3.3 and its chaperone death-domain-associated protein (DAXX) upon *METTL3* knockdown or dCas13b-FTO targeting (Figures 2A, 2B, and S2A). Therefore, given the reduced stability of CENPA on chromosomes upon cenRNA demethylation, we hypothesized that H3.3 nucleosomes may substitute the diminished CENPA nucleosomes during the S phase. The chromatin IP (ChIP)-qPCR results showed a substantial decrease in CENPA binding along with significant increases in H3.3 and DAXX binding upon *METTL3* downregulation (Figure S2N). We then performed ChIP-seq of CENPA and H3.3 during the S phase of A375 cells upon *METTL3* knockdown or dCas13b-FTO targeting. In both scenarios, CENPA binding decreased and H3.3 binding increased in centromere regions encoding methylated cenRNAs, coupled with a negative correlation between the binding level alterations of these two proteins (Figures 2K–2N and S2O–S2R).

Notably, the total protein levels of CENPA and DAXX changed slightly in A375 cells with *METTL3* knockdown or dCas13b-FTO targeting (Figures S2S–S2V). Consistently, we observed accelerated CENPA degradation in A375 cells upon cenRNA hypomethylation with CHX treatment (Figures S2W–S2Z). The CENPA levels did not decline in *METTL3* knockdown A375 cells treated with the proteasome inhibitor MG132 (Figures S2AA and S2AB). These results together indicated that the slightly repressed CENPA expression upon cenRNA demethylation was indeed attributed to the protein degradation, very likely due to the impaired CENPA maintenance on centromeres.

Finally, our TMR-STAR system demonstrated that the newly synthesized H3.3 is highly accumulated during the S phase upon *METTL3* knockdown (Figures S2AC and S2AD). We also visualized reduced CENPA and increased H3.3 with chromatin fiber experiments[15] (Figures 2O and 2P). The results supported that CENPA drop-off during replication results in H3.3 deposition as a placeholder after *METTL3* knockdown. Interestingly, the cenRNA methylation displayed the highest level during S phase in both A375 and HuCCT1 cells (Figure S2AE). Altogether, our results underscore the importance of cenRNA methylation in CENPA maintenance at centromere regions during the S phase.

CENPA preferentially binds to m^{6}A-methylated cenRNA

As revealed by CENPA ChIP-seq data in A375 cells, most CENPA binding peaks were found in the intergenic regions and were predominantly enriched in genomic regions encoding repeat RNAs, particularly in cenRNA regions (Figures 3A and 3B). To test whether such binding pattern of CENPA is related to cenRNA methylation, we categorized different RNA species into METTL3-sensitive, METTL3-insensitive, and non-methylated groups according to the MeRIP-seq data in control and *METTL3* knockdown A375 cells. Strikingly, CENPA binding was only dramatically reduced on the centromeric regions encoding the METTL3-sensitive cenRNA upon *METTL3* knockdown in A375 cells (Figure 3C), a trend not observed for other RNA species (Figure S3A). There also existed a positive correlation between decreased cenRNA methylation and reduced CENPA binding (Figure 3D), suggesting a specific impact for m^{6}A-cenRNA on CENPA binding in centromeres.

CENPA has been reported to bind with cenRNA.[22,27] To test whether such interaction involves cenRNA methylation, we conducted IP followed by RNA sequencing (RIP-seq) of CENPA in A375 cells. RIP-seq analysis presented a significant enrichment of CENPA binding with repeat RNAs, particularly cenRNAs (Figures 3E–3G). The consensus motifs identified from the

(B) Circos plot showing read density along the genome in A375 cells (n = 2). The red rectangles on the chromosome karyotype represent the centromere. The vertical coordinates of two tracks inside indicate the binding enrichment defined as BPM_{IP}/BPM_{Input}. BPM: bins per million mapped reads. zoom_chr4 presents an enlarged display of chromosome 4.

(C) The fold changes in CENPA binding on centr elements upon *METTL3* knockdown. centr elements were categorized into METTL3-sensitive, METTL3-insensitive, or non-methylated (STAR Methods).

(D) The correlation between changes in m^{6}A levels and changes in CENPA binding levels at methylated cenRNA loci upon *METTL3* knockdown based on caRNA MeRIP-seq and ChIP-seq data in A375 cells. The cenRNA loci were categorized into 55 groups based on the rank of CENPA binding level fold change upon *METTL3* knockdown. R refers to Pearson's correlation coefficient.

(E) The distribution of CENPA RIP-seq peaks at distinct genomic regions and at distinct well-defined RNA species in A375 cells.

(F) CENPA enrichment on different RNA species in A375 cells.

(G) Circos plot showing read density along the genome in A375 cells (n = 2). The vertical coordinates of the two tracks inside indicate the binding enrichment defined as BPM_{IP}/BPM_{Input}.

(H) Enriched consensus motifs identified from m^{6}A peaks on methylated cenRNAs, and CENPA RIP-seq peaks in A375 cells.

(I) The CENPA enrichment on methylated (m^{6}A, $\log_2$[IP/input] > 0.58 derived from our MeRIP-seq data) or non-methylated (non-m^{6}A) cenRNA in A375 cells.

(J) The non-ribosomal RNA m^{6}A modification levels in input and CENPA-RIP RNA from A375 cells were quantified using LC-MS/MS analysis (n = 3).

(K) The changes in protein levels upon *METTL3* knockdown in A375 cells, quantified by mass spectrometry post cenRNA ChIRP to profile the cenRNA-enriched proteome. Up: $\log_2$FoldChange > 0.58 and p value < 0.05; down: $\log_2$FoldChange < −0.58 and p value < 0.05.

(L and M) EMSA showing the binding capacity of CENPA with methylated and unmethylated RNA probes (L). The dissociation constants (K_D) were calculated by quantifying the bands with ImageJ and fitting the binding curves using GraphPad prism (M) (n = 3).

(N–P) The distances between two particles when RNA probes and CENPA separated detected by GLC-TEM (N), and cumulative distributions and boxplots (inner) showing the distance between CENPA and methylated or unmethylated RNA probes (probe 1) with quantification according to the 314 frames captured (O). The distances between RNA probes and CENPA were divided into two groups (0–3 nm: closer distances; 3–17 nm: greater distances), and the respective percentages were calculated for each group (P).

p values were calculated by Wilcoxon test (C, F, I, and O). Error bars indicate mean ± SEM (J and M).

See also Figure S3.

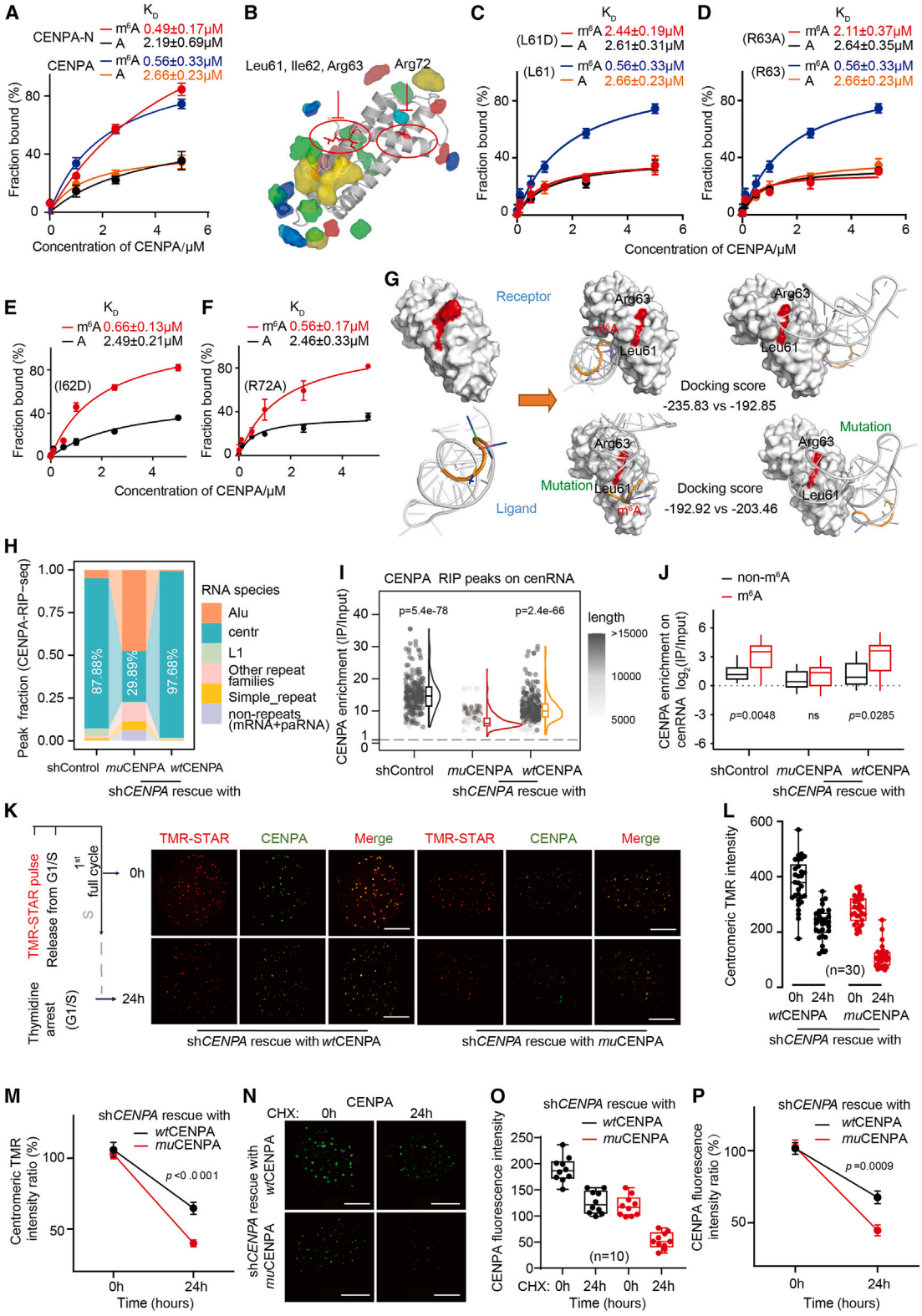

Figure 4. Leu61 and Arg63 are essential residues for the methylated RNA binding of CENPA

(A) The K_D was calculated using GraphPad prism by fitting the curves for the binding affinity of the methylated or unmethylated RNA probes for CENPA-N (N-terminal) or CENPA (full-length) (n = 3).

(legend continued on next page)

CENPA RIP-seq data mirrored those recognized for m^{6}A-modified cenRNAs (Figure 3H), indicating a potential preference for CENPA to bind with m^{6}A-modified cenRNAs. We thus compared the CENPA enrichment on different RNA species based on their methylation status. Strikingly, CENPA strongly preferred to bind m^{6}A-marked cenRNAs relative to the non-m^{6}A group, a pattern not observed for other RNA types (Figures 3I and S3B). Such a preference was further confirmed by CENPA RIP followed by LC-MS/MS detection, which presented a significant enrichment of m^{6}A methylation, rather than other modifications, on the CENPA-bound RNA fraction (Figures 3J and S3C–S3G).

Subsequently, we conducted cenRNA ChIRP followed by protein MS to evaluate the cenRNA-binding proteome alterations in A375 cells. CENPA stands out as the most depleted cenRNA-interaction protein upon *METTL3* knockdown (Figure 3K). Such a depletion of CENPA was confirmed via immunoblotting post cenRNA ChIRP in A375 cells upon *METTL3* knockdown or dCas13b-*wt*FTO targeting, but not dCas13b-*mu*FTO (Figures S3H and S3I). Collectively, these results indicated a strong preference for CENPA to bind with m^{6}A-modified cenRNAs.

To verify if CENPA is a direct reader of m^{6}A methylation, we purified CENPA protein, synthesized pairs of m^{6}A and non-m^{6}A probes incorporating either endogenous methylated cenRNA sequences or an external sequence representing canonical consensus motif of m^{6}A (Figures S3J and S3K). The *in vitro* electrophoretic mobility shift assays (EMSAs) revealed that the binding affinity of CENPA to methylated probe was nearly 5-fold higher than the unmethylated one for all three paired RNA probes (Figures 3L, 3M, S3L, and S3M). We then conducted streptavidin pull-down with synthesized RNA probes, and the following immunoblotting assay showed that m^{6}A probe enriched more CENPA proteins compared with non-m^{6}A probe (Figure S3N). Both experiments demonstrated a clear preference for CENPA to bind the m^{6}A-containing probes *in vitro*.

Furthermore, we directly imaged and quantified the CENPA-m^{6}A/non-m^{6}A RNA interactions at the single-molecule resolution using a graphene liquid cell transmission electron microscopy (GLC-TEM)[47] with nanometer scales. With the obtained 3,957 frames, we observed CENPA and RNA probes recombined to a complex shown as a single particle (at 72.9 s) and their transient dissociation (at 45.9 s) (Figure S3O). Moreover, we observed that the m^{6}A-modified probe maintained statistically shorter distances when dissociating from CENPA than non-modified probe (Figures 3N–3P). All this evidence strongly supported the notion that m^{6}A methylation enhances the RNA-binding affinity of CENPA.

CENPA binds m^{6}A-methylated cenRNAs via two key aa residues

We next aimed to unravel the molecular basis for the CENPA binding preference to m^{6}A-methylated cenRNAs. We first constructed and purified truncated versions of both the N termini (CENPA-N: 1–74 amino acids [aa]) and C termini (CENPA-C: 75–140 aa) of CENPA (Figures S4A and S4B). The EMSA experiments presented that CENPA-N is responsible for RNA binding and has a similar preference to the m^{6}A probes as the full-length CENPA, whereas CENPA-C barely binds RNA (Figures 4A and S4C). Interestingly, GeoBind,[48] based on geometric deep learning, then identified the first 39 aa of the N terminus as the most promising region of CENPA responsible for selective RNA binding (Figure S4D). Thus, we constructed another CENPA truncation spanning aa 40–140 (CENPA-DC), and consistent with the prediction, it no longer binds RNA (Figures S4B and S4C). We then employed NucleicNet[49] to predict the binding preferences of RNA constituents on the surface of CENPA protein. The prediction results identified Leu61, Ile62, Arg63, and Arg72 sites with the highest potential for binding to m^{6}A base (Figure 4B). Subsequently, we created individual mutant variants of CENPA protein at these four aa sites (L61D, I62D, R63A, and R72A) and observed that Leu61 and Arg63 mutation almost completely abolished the preference of CENPA to the m^{6}A probe without affecting its binding affinity for the non-m^{6}A probe (Figures 4C–4F, S4E, and S4F).

Next, we employed molecular docking to validate the impact of Leu61 and Arg63 on the interaction between CENPA

(B) NucleicNet prediction of the RNA-binding sites on the CENPA protein (PDB: 3NQU). Top 10% of the binding sites are depicted on the semitransparent surface. Color code: phosphate-yellow, ribose-green, adenine-blue, cytosine-red, guanine-cyan, uracil-purple, and protein-gray cartoon.

(C–F) The K_D was calculated using GraphPad prism by fitting the curves for the binding affinity of methylated or unmethylated RNA probes for CENPA with mutation at position 61 (C), 63 (D), 62 (E), 72 (F), or wild-type CENPA (n = 3).

(G) Cross-docking experiment showing that the methylation of adenine significantly contributes to the binding affinity of CENPA protein with RNA. Lower docking score refers to a more stable binding status of protein-RNA complex. After mutating two sites (both the L61D and R63A) of CENPA protein, m^{6}A modification of RNA is not more inclined to bind the mutant CENPA compared with the prototype version.

(H) The distribution of CENPA RIP-seq peaks at distinct well-defined RNA species in control A375 cells, as well as *CENPA* knockdown cells followed by expressing wild-type CENPA (*wt*CENPA) or double-mutant CENPA (*mu*CENPA).

(I and J) CENPA enrichment on cenRNA RIP-seq peaks (I) and cenRNA (J) in control A375 cells, as well as *CENPA* knockdown cells followed by expressing *wt*CENPA or *mu*CENPA quantified by CENPA RIP-seq data. Each point represents a peak, with color representing peak length. cenRNA were divided into methylated (m^{6}A, log$_2$[IP/input] > 0.58) or non-methylated (non-m^{6}A) groups. p values were calculated by Wilcoxon test. ns, not significant.

(K–M) Cells were synchronized and labeled with SNAP-tagged CENPA (red), total CENPA (green) in *CENPA* knockdown A375 cells rescued by either *wt*CENPA or *mu*CENPA (K). The fluorescence intensity of SNAP-tagged CENPA was quantified using ImageJ (L), and the ratio at 24 h relative to 0 h was calculated using GraphPad prism (M).

(N–P) CENPA fluorescence intensity (green) in the sh*CENPA*-rescued cells expressing *wt*CENPA or *mu*CENPA following treatment with CHX at different time points were examined (N), the fluorescence intensity of CENPA was quantified using ImageJ (O), and the ratio at 24 h relative to 0 h was calculated using GraphPad prism (P).

Error bars indicate mean ± SEM (A, C–F, M, and P). The n shown in the figures represents the total number of cells randomly selected and used for quantifications (L and O). Scale bar: 5 μm in (K) and (N).

See also Figure S4.

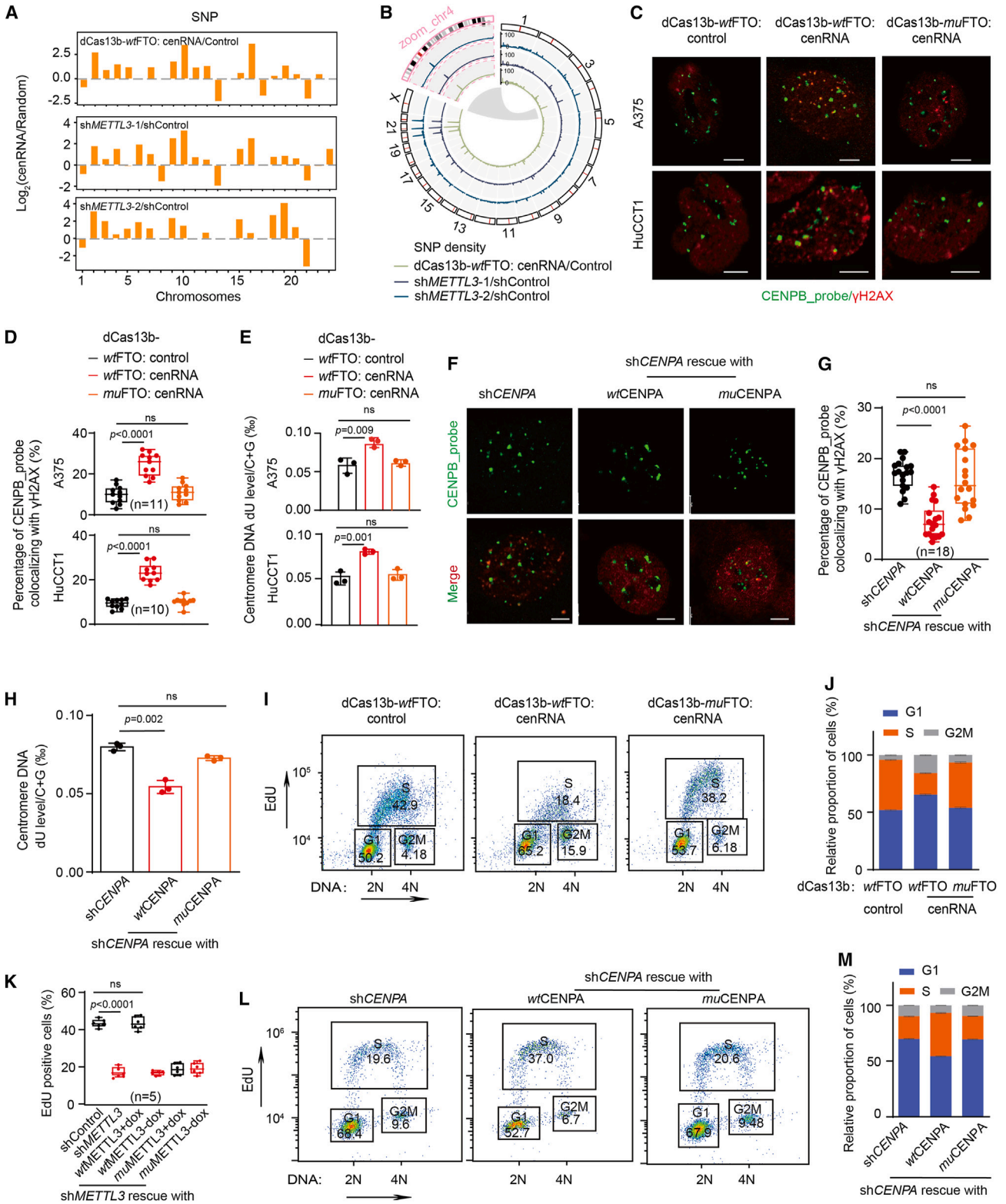

Figure 5. The interaction between CENPA with m^{6}A-cenRNA is critical for preserving centromeric stability

(A) The centromeric instability on each chromosome (log_2[$cenRNA_{mean}$/$random_{mean}$]), measured by single nucleotide polymorphisms (SNPs). A value greater than 0 indicates increased centromere instability on that chromosome (STAR Methods).

(legend continued on next page)

and m^{6}A-modified RNA. The cross-docking process directly confirmed that the adenine methylation significantly enhanced the CENPA binding affinity with RNA, showing the m^{6}A site within 5 Å to Leu61 (Figures 4G and S4G). Strikingly, the double-mutated CENPA protein displayed a reduced propensity to bind with m^{6}A-modified RNA, almost akin to its binding with the non-methylated probe (Figure 4G). These findings strongly supported the pivotal role of these two aa residues on CENPA in preserving its binding preference for m^{6}A.

To determine the impact of CENPA mutations on its *in vivo* binding specificity, we conducted RIP-seq of CENPA in A375 cells following *CENPA* knockdown and subsequent overexpression of either wild-type CENPA (*wt*CENPA) or double-mutant CENPA (*mu*CENPA) (Figures S4H and S4I). As expected, the CENPA binding peaks were enriched in the intergenic regions and predominantly on repeat RNAs, especially cenRNAs, in A375 cells rescued with *wt*CENPA, highly consistent with the results of RIP-seq for the endogenous CENPA (Figures 4H and S4J). By contrast, the CENPA binding peaks were much less in cenRNAs and with lower read densities from RIP-seq of *mu*CENPA compared with *wt*CENPA (Figures 4H, 4I, and S4K). We again categorized various RNA species into m^{6}A-marked and non-m^{6}A groups according to their methylation status. The stronger binding preference of CENPA to m^{6}A-marked cenRNAs than non-m^{6}A cenRNAs was well reproduced by *wt*CENPA but abolished by *mu*CENPA overexpression, a trend not observed in other RNA species (Figures 4J and S4L). Altogether, these results confirmed the *mu*CENPA lost its binding affinity to methylated cenRNAs in A375 cells.

Given the role of methylated cenRNA in maintaining centromere stability, we examined the centromere stability in *CENPA* knockdown A375 cells with overexpression of either *wt*CENPA or *mu*CENPA. The TMR-STAR system first confirmed that *CENPA* knockdown induced CENPA reduction during the S phase, similar to the effects upon cenRNA demethylation. Such effects were well reversed by introducing *wt*CENPA but not *mu*CENPA (Figures 4K–4M). In addition, upon CHX treatment, the fluorescence intensity of CENPA within centromere regions was remarkably decreased in the *CENPA* knockdown cells rescued by *mu*CENPA in comparison with *wt*CENPA during the S phase, reinforcing the crucial role of the interaction between CENPA and methylated cenRNA in maintaining centromeric CENPA stability during the S phase (Figures 4N–4P, S4M, and S4N). Interestingly, we also noticed that Leu61 and Arg63 of CENPA were highly conserved across different species in vertebrates and model organisms, implying the significance of these two aa for CENPA (Figure S4O).

Disruption of the CENPA-m^{6}A cenRNA interaction results in chromosome instability and cell-cycle defects in cancer cells

The dynamic changes in CENPA expression and localization throughout the cell cycle are essential for safeguarding centromere stability and thereby assuring the accurate chromosome segregation during cell mitosis.[27] Given the role of the interaction between CENPA and methylated cenRNA for CENPA maintenance in the centromeric regions, we further assessed its impact on centromere integrity. We performed whole-genome sequencing and observed a global increase in genomic instability events in A375 cells with *METTL3* knockdown or dCas13b-FTO targeting, which were highly enriched in the centromeric regions compared with random regions (Figures 5A, 5B, and S5A). Fluorescence *in situ* hybridization (FISH) and immunofluorescence assays illustrated higher levels of DNA damage in the centromeric region in response to cenRNA hypomethylation (Figures 5C, 5D, S5B, and S5C). LC-MS/MS analysis of dU, the most abundant DNA damage type in centromeric region,[50] also showed a remarkable increase upon downregulated cenRNA methylation (Figures 5E and S5D).

To further investigate whether the increased centromere instability due to cenRNA demethylation is mediated by reduced CENPA binding, we conducted overexpression of *wt*CENPA or *mu*CENPA in A375 cells with *CENPA* knockdown. As expected, the increased centromere damage upon *CENPA* knockdown could only be rescued by *wt*CENPA overexpression rather than *mu*CENPA (Figures 5F–5H). Moreover, the increase in centromere damage induced by cenRNA hypomethylation could be recovered, but only partially, by overexpressing *wt*CENPA instead of *mu*CENPA (Figures S5E–S5G). Altogether, these results emphasize the significance of the interaction between CENPA and cenRNA methylation in centromere stability maintenance.

Elevated DNA damage in centromeric regions could distort cell cycles.[51] As expected, we observed a significant reduction in the population of S phase cells in A375 cells with either *METTL3* knockdown or dCas13b-FTO treatment (Figures 5I, 5J, and S5H–S5M). The disruption caused by *METTL3* knockdown was reversible only by overexpressing wild-type METTL3 rather than the catalytic-inactive mutant (Figures 5K and S5N).

(B) SNP density along the genome that occurred after either *METTL3* knockdown or dCas13b-FTO treatment. The vertical coordinates of the three tracks inside indicate SNP density (STAR Methods). Red rectangle: the centromere.
(C and D) Centromeric immunofluorescence (CIF) upon dCas13b-FTO treatment in A375 cells. Cells were stained with anti-γH2AX and FISH with centromeric probes (C), and the corresponding percentages of γH2AX colocalizing with centromeres were quantified using ImageJ (D).
(E) LC-MS/MS quantifying the levels of dUMP in centromeric DNA extracted from dCas13b-FTO treatment A375 and HuCCT1 cells (n = 3).
(F and G) CIF in A375 cells with *CENPA* knockdown and those rescued with *wt*CENPA or *mu*CENPA.
(H) LC-MS/MS quantifying the levels of dUMP in centromeric DNA extracted from A375 cells with *CENPA* knockdown and those rescued with *wt*CENPA or *mu*CENPA (n = 3).
(I and J) Cell cycle distribution analyzed in A375 cells upon dCas13b-FTO treatment by flow cytometry (I), with the ratio of cells at different stages of cell cycle shown in (J).
(K) Cell cycle distribution analyzed by EdU immunofluorescence in *METTL3* knockdown A375 cells and rescued with wild-type or inactive mutant METTL3 (n = 5).
(L and M) Cell cycle distribution analyzed by flow cytometry in *CENPA* knockdown A375 cells and rescued with *wt*CENPA or *mu*CENPA (n = 3).
Scale bar: 5 μm in (C) and (F). Error bars indicate mean ± SEM (E, H, J, and M). ns, not significant (D, E, G, H, and K). The n shown in the figures represents the total number of cells randomly selected and used for quantifications (D, G, and K).
See also Figure S5.

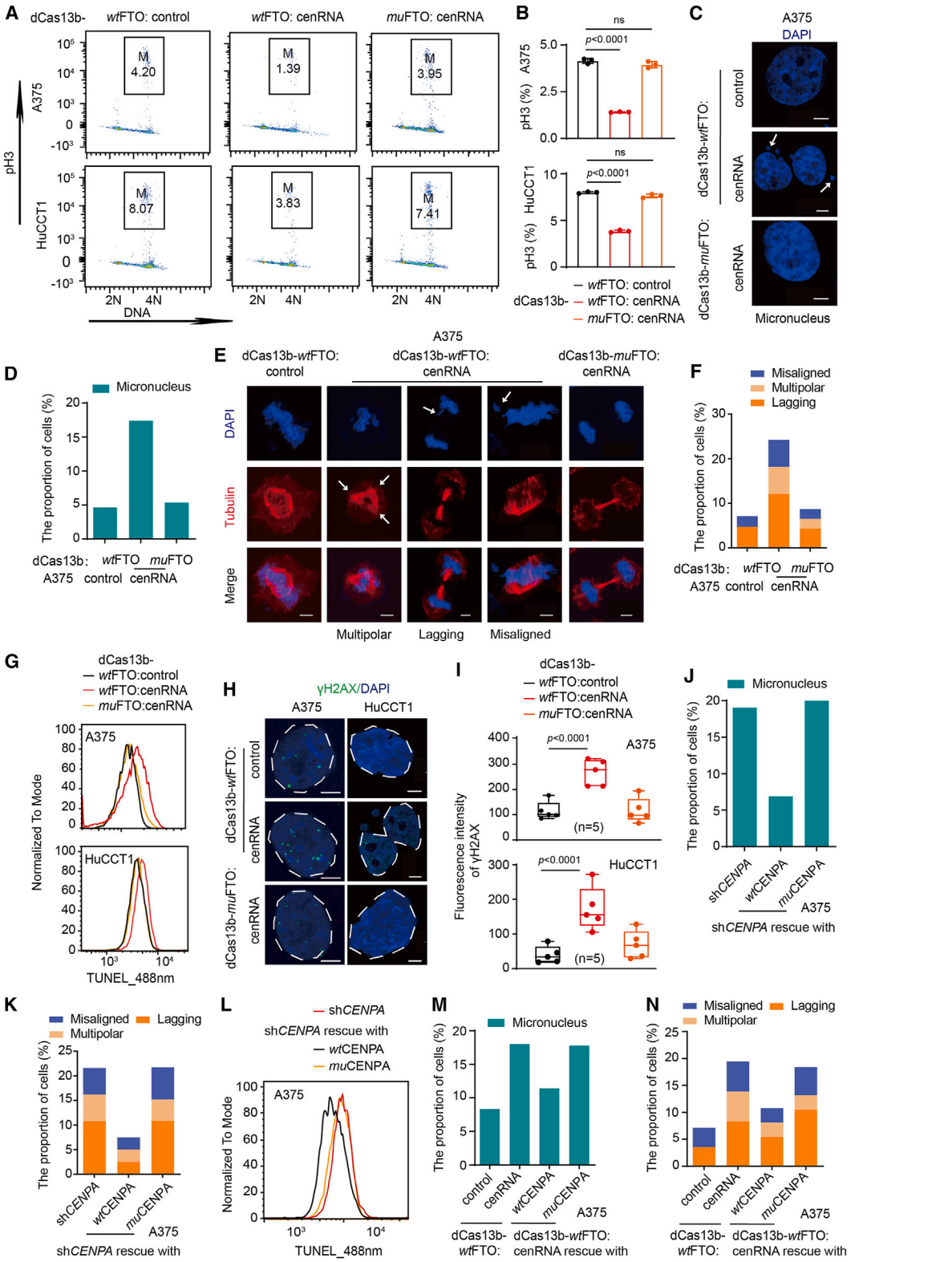

Figure 6. Disruption of CENPA-m^{6}A interaction causes aberrant cell mitosis and genomic instability

(A and B) The number of dividing A375 and HuCCT1 cells upon dCas13b-FTO treatment detected by flow cytometry (A), with the ratio of cells in M phases analyzed in (B) (n = 3). Error bars indicate mean ± SEM. ns, not significant.

(legend continued on next page)

Similarly, we observed reduced S phase cells upon *CENPA* knockdown, which could be only reversed by *wt*CENPA overexpression, not *mu*CENPA (Figures 5L and 5M). These observations confirm that the preferential binding of CENPA with m^{6}A-methylated cenRNAs is essential for maintaining centromere stability and normal cell cycle.

Disruption of the CENPA-m^{6}A cenRNA interaction leads to aberrant cell mitosis and genome instability in cancer cells

We then continued to investigate the function of the CENPA-m^{6}A cenRNA interaction in sustaining cell mitosis and genome stability. We employed flow cytometry to pinpoint the mitotic cells and observed a substantial reduction in cell numbers under division in A375 and HuCCT1 cells targeted by dCas13b-*wt*FTO (Figures 6A and 6B). Live-cell imaging of A375 and HuCCT1 cells expressing histone 2B-mCherry[52] further confirmed a significant mitotic defect upon cenRNA demethylation in A375 and HuCCT1 cells (Videos S1, S2, S3, and S4). The immunofluorescence assays demonstrated a significantly higher frequency of chromosomal missegregations in these mitotic cells with cenRNA hypomethylation, including misaligned chromosomes, lagging chromosomes, multipolar spindles, and micronuclei (Figures 6C–6F and S6A–S6H). CenRNA methylation reduction also resulted in a significant increase in double-stranded DNA breaks in both A375 and HuCCT1 cells (Figures 6G–6I and S6I–S6K). All these results emphasized the crucial role of cenRNA methylation in maintaining genomic stability and proper cell division.

Furthermore, we observed increased severity of chromosomal instability and DNA damage resulting from *CENPA* knockdown, similar to the effects of disrupting cenRNA methylation. These effects could be largely reversed only with the overexpression of *wt*CENPA, not *mu*CENPA (Figures 6J–6L and S6L–S6O). Similarly, in the cells with cenRNA hypomethylation, the elevated chromosome instability could only be partially alleviated by overexpressing *wt*CENPA instead of the mutant (Figures 6M, 6N, and S6P–S6U), emphasizing the importance of m^{6}A binding of CENPA. Altogether, our results have demonstrated the role of cenRNA methylation in safeguarding chromosome and genomic stability through its interaction with CENPA.

Targeting the interaction between CENPA and m^{6}A-modified cenRNA impairs tumor growth

Although chromosome instability is a key contributor to cellular malignancy and therapeutic resistance, excess genomic mutations beyond a certain threshold can hasten cell death. Given that disruption of the interaction between CENPA and m^{6}A-modified cenRNA induces centromeric and genomic instability, we hypothesized that such instability might surpass a lethal threshold, therefore resulting in pronounced cell death and enhancement of cancer therapeutic efficacy. Indeed, cell proliferation and colony growth were largely inhibited by either dCas13b-FTO targeting, *METTL3* knockdown, or downregulation of CENPA (Figures 7A, 7B, S7A, and S7B). Overexpression of *wt*CENPA, but not *mu*CENPA, can reverse such repression on cell growth (Figures 7A and 7B). We then used the A375 cells to establish mouse xenograft tumor growth models. Not surprisingly, we observed a substantial decrease in tumor weight and volume upon reduced cenRNA methylation or CENPA mutation (Figures 7C–7H and S7C). Therefore, both the CENPA mutation and the cenRNA hypomethylation effectively inhibit tumor growth.

Chemotherapeutic agents elicit cytotoxic effects on cancer cells by inducing genomic instability beyond the tolerance threshold of malignant cells. However, development of drug resistance remains a significant challenge to effective cancer treatment. Given the centromere and genomic instability stemming from reduced m^{6}A methylation, we aimed to explore the potential of combination therapeutic strategies. We selected eight drugs interfering with centromere activity and another eight drugs targeting DNA damage repair (Table S3), all of which have been undergoing clinical development. We investigated the efficacy of these 16 drugs when combined with the METTL3 inhibitor STM2457.[53] Intriguingly, most centromere-interfering drugs exhibited superior combinatorial effects with STM2457 compared with the drugs inducing general DNA damage (Figure 7I). For example, the half-maximal inhibitory concentration (IC_{50}) of AZD1152 (Aurora B inhibitor)[54] and Tozasertib (Aurora A/B/C inhibitor)[55] were significantly reduced when combined with *METTL3* knockdown, dCas13b-*wt*FTO targeting, or CENPA mutation compared with controls in A375 and HuCCT1 cells (Figures 7J, 7K, and S7D–S7F). In this way, the disrupted interaction between CENPA and m^{6}A-modified cenRNAs has the potential to synergize with agents that specifically target centromere integrity to overcome drug resistance.

To test the potential of targeting cenRNA methylation as a therapeutic strategy, we also assessed the effects of cenRNA demethylation in two normal cell lines, HEK293T and IMR90. Notably, *METTL3* knockdown in IMR90 cells induced limited changes in either DNA damage level (Figures S7G and S7H) or CENPA expression in centromeric regions (Figures S7I and

(C and D) Immunofluorescence analysis in A375 and HuCCT1 cells upon dCas13b-FTO treatment. Cells were stained with DAPI to perform a micronucleus assay (C) and quantification of cells with micronucleus (D) shown in (C). The arrows indicated the micronucleus of cell.
(E and F) Immunofluorescence analysis in A375 cells upon dCas13b-FTO treatment. Cells were stained with anti-tubulin and DAPI to visualize mitotic defects (E) and quantification of cells with different types of chromosome defects (F) shown in (E). The arrows indicated the specific types of mitotic abnormalities.
(G) Assessment of DNA damage by TUNEL assay in A375 and HuCCT1 cells upon dCas13b-FTO treatment.
(H and I) Detection of γH2AX fluorescence intensity (F) and the corresponding quantification (G) in A375 and HuCCT1 cells upon dCas13b-FTO treatment ($n = 5$).
(J and K) Quantification of cells with micronucleus (J) and other types of chromosome defects (K) in *CENPA* knockdown A375 cells and rescued with *wt*CENPA or *mu*CENPA.
(G) Assessment of DNA damage by TUNEL assay in A375 cells with *CENPA* knockdown and those rescued with *wt*CENPA or *mu*CENPA.
(M and N) Quantification of cells with micronucleus (M) and other types of chromosome defects (N) in A375 cells with dCas13b-FTO treatment followed by overexpressing of *wt*CENPA or *mu*CENPA.
Scale bar: 5 μm in (C), (E), and (H).
See also Figure S6.

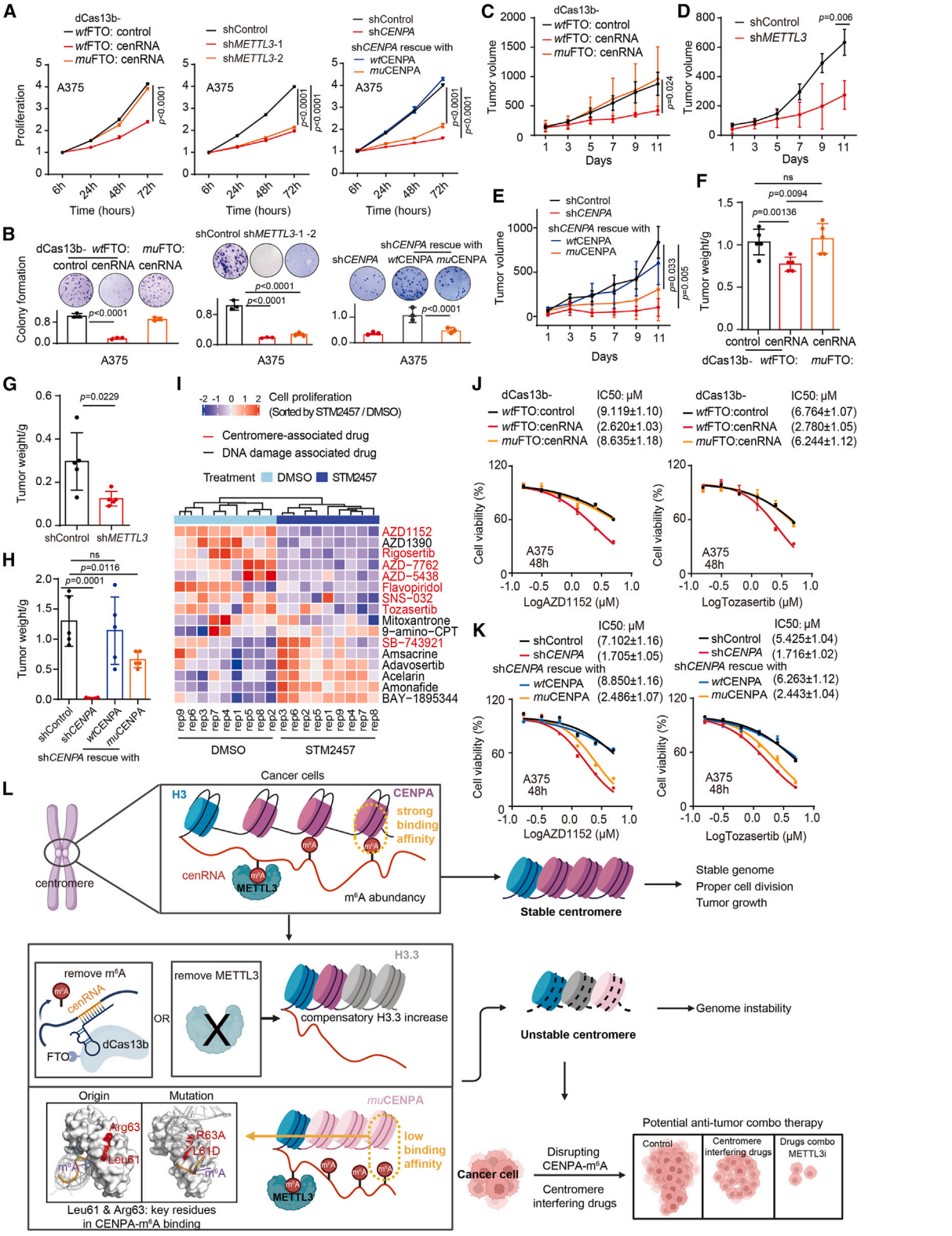

Figure 7. The interaction between CENPA and m^{6}A-modified cenRNA promotes tumor growth

(A and B) The cell viability and clonogenic potential evaluated using CCK-8 assay (A) and crystal violet staining (B) in A375 cells with dCas13b-FTO treatment, *METTL3* knockdown, or *CENPA* knockdown followed by overexpressing *wt*CENPA or *mu*CENPA (n = 3).

(legend continued on next page)

S7J). The abundance of dU and cell cycle dynamics also remained unchanged following *METTL3* knockdown in both IMR90 and HEK293T cells (Figures S7K–S7M). Consistently, the frequency of chromosomal missegregations and double-stranded DNA breaks remained the same (Figures S7N and S7O). Finally, we observed little change in IMR90 cells and only a very mild decrease in HEK293T cells in cell proliferation and colony formation upon *METTL3* knockdown (Figures S7P and S7Q). Altogether, these results demonstrate the minor effects of cenRNA methylation for the viability of normal cells, further supporting the feasibility of targeting the CENPA-m^{6}A cenRNA interaction as a cancer therapeutic strategy.

DISCUSSION

Centromeres are essential for preserving chromosome stability, and their dysregulation impacts diverse aspects of tumor phenotypes.[27,28] Transcribed from centromeres, cenRNA has been shown to be essential to centromere function and proper cell division.[6,56,57] In this study, we uncovered that in cancer cell lines, cenRNAs present the highest enrichment of m^{6}A modifications compared with other RNA species. By contrast, non-cancerous cell lines such as HEK293T and IMR90 (Figure 1C), as well as mouse and human embryonic stem cells (ESCs) (data not shown), did not exhibit such enrichment of cenRNA methylation. Interestingly, the repeat element LINE1 has been reported to be highly methylated in mESCs,[33,39] but not in the cancer and non-cancerous cells we studied (Figure S1A). Such cell context-dependent methylation of repeat RNAs suggest diverse regulation potential of repeat RNA methylation in a range of biological processes.

We demonstrated CENPA as an m^{6}A reader of methylated cenRNA and that the modified cenRNA in cancer cells is essential for maintaining CENPA on centromeres during the S phase of cell cycles. Therefore, the elevated cenRNA methylation may serve as a protective mechanism to maintain centromere and genome integrity during uncontrolled cancer cell proliferation. Disrupting the CENPA-cenRNA interaction, through either mutation of the critical residues in CENPA or reduction of cenRNA methylation, caused centromere-bound CENPA loss during the S phase. This in turn leads to abnormal chromosome separation during mitosis, severe genomic instability, and impaired cancer cell proliferation and tumor growth (Figure 7M).

Maintenance of CENPA in the centromeres depends on the function of CENPA as a reader of m^{6}A on cenRNA

CENPA is a crucial constituent of centromeric chromatin and is responsible for accurate chromosome segregation during cell division.[55,56] While AT-rich repetitive sequences on centromere and the inherently flexible structure of CENPA both add complexity to CENPA maintenance,[58–60] the mechanism ensuring CENPA inheritance under replication and transcription pressures remains unclear. We determined that the interaction between CENPA with methylated cenRNA is responsible for CENPA maintenance during cancer cell division. Specifically, we observed significantly higher m^{6}A level on cenRNAs during the S phase, consistent with the model that m^{6}A cenRNA promotes the engagement of CENPA specifically during this stage. It would also be interesting to explore whether such chromatin regulation related to RNA methylation applies to other histone variant species.

Targeting the interaction between CENPA and methylated cenRNA as a potential cancer therapy

Chromosomal instability is a hallmark of genomic alterations in cancer.[61] However, severe chromosomal instability can result in lethal genomic imbalances, which could potentially be exploited for cancer therapy.[62,63] Our results underscore the importance of the interaction between CENPA and m^{6}A-modified cenRNA in preserving centromeric stability during cancer cell division. Disrupting such interaction can induce lethal chromosome missegregation, ultimately reducing cell proliferation capacity and tumor growth. Recent studies have demonstrated that inhibiting a spindle protein can selectively reduce the viability of tumor cells with high chromosome instability while having minimal effects on diploid cells.[64] Similarly, our findings have shown that the cancer cell growth is much more sensitive to disrupting the interaction between CENPA and m^{6}A-modified cenRNA. Additionally, targeting such interaction dramatically enhances the cytotoxicity of centromere-interfering agents, which could serve as a target in combinational anti-cancer therapy that is worth pursuing via pre-clinical development in the future.

Limitations of the study

Findings of this study raise some questions that are yet to be resolved. First, we showed that cenRNA methylation levels are higher in cancer cells compared with normal cells based on the analysis of MeRIP-seq data and related experiments from five established cancer cell lines (A375, HEC-1-A, HepG2, K562, and MCF7) and two non-cancerous cell types. However, this conclusion may not apply to all cancer types. It remains unclear how these cancer cells implement and maintain such higher levels of m^{6}A modifications on cenRNAs. Currently, the mechanism(s) ensuring CENPA association with centromere in normal cells remain elusive. Second, while we demonstrated the importance of modified cenRNA in ensuring centromere integrity in cancer cells, it remains unclear whether the m^{6}A modifications

(C–H) A375 cells with dCas13b-FTO treatment (C and F), *METTL3* knockdown (D and G), or *CENPA* knockdown followed by overexpressing *wt*CENPA or *mu*CENPA (E and H) were subcutaneously injected into the flank of nude mice. The tumor volume (C–E) and weight (F–H) of the mice were quantified (n = 5).
(I) The effects of the combination of METTL3 inhibitor (STM2457) with 16 centromere interfering or DNA damage drugs. The analysis focused on cell proliferation in both control and STM2457-treated A375 cells subjected to the aforementioned drugs (n = 9).
(J and K) Dose-response curves and corresponding half-maximal inhibitory concentration (IC_{50}) values for AZD1152 and Tozasertib treatment 48 h in A375 cells with dCas13b-FTO targeting or *CENPA* knockdown followed by overexpressing *wt*CENPA or *mu*CENPA (n = 3).
(L) Schematic showing the mechanism underlying how m^{6}A-modified cenRNA regulates centromere homeostasis.
Error bars represent mean ± SEM (A–H, J, and K). ns, not significant (F and H).
See also Figure S7.

are also involved in additional aspects of centromere biology, including centromere-chromatin accessibility and cenRNA homeostasis. Finally, apart from the structural simulation analysis and experimental validation to identify the two key residues of CENPA that recognize methylated cenRNA, structural biology tools will be helpful to resolve the structure details and binding mechanism of the CENPA-cenRNA interaction.

RESOURCE AVAILABILITY

Lead contact

Further information and requests for resources and reagents should be directed to and will be fulfilled by the lead contact, Jun Liu (junliu1223@pku.edu.cn).

Materials availability

This study did not generate new, unique reagents.

Data and code availability

- All sequencing data have been deposited at GEO and SRA and are publicly available as of the date of publication. Accession numbers are listed in the key resources table.
- This paper does not report any original code.
- Any additional information required to reanalyze the data reported in this work paper is available from the lead contact upon request.

ACKNOWLEDGMENTS

We thank Dr. Guohong Li for SNAP-TAG-CENPA and pET-Duet1-CENPA-H4 plasmids, Dr. Peng Du for pTRE 3G-dSpCas9 and pLVX-Tet3G plasmids, and Dr. Yawei Gao and Dr.Zhouliang Yu for valuable suggestions. We thank the National Center for Protein Sciences and the Core Facilities of Life Sciences at Peking University. We also acknowledge the support from the Tsinghua University Branch of China National Center for Protein Sciences (Beijing), including the core facilities of Genome Sequencing and Analysis and Biocomputing. This study received support from the National Key Research and Development Program of China (2023YFC3402200 to J.L. and 2023YFC3043300 to X.Y.), the National Natural Science Foundation of China (32170595 to J.L. and 32330022, W2411012, and 81972912 to X.Y.), the Beijing Nova Program to J.L. (Z211100002121011 and 20230484442), the Clinical Medicine Plus X-Young Scholars Project of Peking University (Fundamental Research Funds for the Central Universities), Funding by Major Program of Shenzhen Bay Laboratory (S241101001), the Center for Life Sciences (CLS), the School of Life Sciences (SLS) of Peking University, the SLS-Qidong Innovation Fund, the Li Ge Zhao Ning Life Science Junior Research Fellowship, the National Special Support Program for High-Level Talents, and the Tsinghua University Initiative Scientific Research Program.

AUTHOR CONTRIBUTIONS

J.L. and Z.K. conceived the original idea and designed original studies. Z.K. performed most experiments with assistance from X.D., L.X., X.L., Y.X., W.S., L.W., and H.W. R.L. performed most bioinformatics analysis with assistance from X.Y. Y.H. performed the AI simulation with assistance from L.G. and L.Z. J.L., X.Y., Z.K., and R.L. wrote the manuscript with help from C.L., Q.L., and input from all authors.

DECLARATION OF INTERESTS

The authors declare no competing interests.

STAR★METHODS

Detailed methods are provided in the online version of this paper and include the following:

- KEY RESOURCES TABLE
- EXPERIMENTAL MODEL AND STUDY PARTICIPANT DETAILS
  - Mice
  - Cell culture
- METHOD DETAILS
  - RNA isolation
  - RT-qPCR
  - CRISPR-dCas13b plasmid transfection
  - m^6A-IP and RT-qPCR
  - SELECT
  - Immunofluorescence and confocal microscopy
  - Metaphase spread and FISH
  - Co-FISH
  - Genomic and centromere DNA extraction
  - LC-MS/MS quantitation of dU in DNA
  - Cell fractionation
  - LC-MS/MS quantitation of the RNA modification
  - Cell cycle analysis
  - Western blot analysis
  - caRNA m^6A-seq
  - CaRNA m^6A-seq data analysis
  - Definition of carRNAs and lncRNAs
  - m^6A levels of distinct RNA species
  - ChIRP probes design for cenRNA
  - ChIRP-seq
  - ChIRP-seq data analysis
  - Whole-genome sequencing
  - Data analysis of whole-genome sequencing
  - Chromatin-bound protein MS analysis
  - SNAP labeling
  - Chromatin fiber assay
  - ChIP-qPCR and ChIP-seq
  - ChIP-seq data analysis
  - RIP-qPCR and RIP-seq
  - CENPA RIP-seq data analysis
  - $CENPA^{wt}$- and $CENPA^{mu}$- H4 bacterial expression
  - RNA-protein EMSA
  - RNA binding protein pulldown
  - Electron microscopy
  - Segmentation of the RNA binding interface
  - Prediction of CENPA-m^6A-RNA binding sites
  - Validation of CENPA-m^6A-RNA binding sites
  - Cross-species conservation of the CENPA
  - TUNEL assay
  - Colony formation assay
  - Cell proliferation assay
  - Drug screening and IC_{50} measurement
- QUANTIFICATION AND STATISTICAL ANALYSIS

SUPPLEMENTAL INFORMATION

Supplemental information can be found online at https://doi.org/10.1016/j.cell.2024.08.040.

Received: December 12, 2023
Revised: January 10, 2024
Accepted: August 20, 2024
Published: September 20, 2024

REFERENCES

1. Cleveland, D.W., Mao, Y., and Sullivan, K.F. (2003). Centromeres and kinetochores: from epigenetics to mitotic checkpoint signaling. Cell *112*, 407–421. https://doi.org/10.1016/s0092-8674(03)00115-6.

2. Walczak, C.E., Cai, S., and Khodjakov, A. (2010). Mechanisms of chromosome behaviour during mitosis. Nat. Rev. Mol. Cell Biol. *11*, 91–102. https://doi.org/10.1038/nrm2832.

3. Gordon, D.J., Resio, B., and Pellman, D. (2012). Causes and consequences of aneuploidy in cancer. Nat. Rev. Genet. *13*, 189–203. https://doi.org/10.1038/nrg3123.

4. Sheltzer, J.M., Blank, H.M., Pfau, S.J., Tange, Y., George, B.M., Humpton, T.J., Brito, I.L., Hiraoka, Y., Niwa, O., and Amon, A. (2011). Aneuploidy drives genomic instability in yeast. Science *333*, 1026–1030. https://doi.org/10.1126/science.1206412.

5. Pesenti, M.E., Raisch, T., Conti, D., Walstein, K., Hoffmann, I., Vogt, D., Prumbaum, D., Vetter, I.R., Raunser, S., and Musacchio, A. (2022). Structure of the human inner kinetochore CCAN complex and its significance for human centromere organization. Mol. Cell *82*, 2113–2131.e8. https://doi.org/10.1016/j.molcel.2022.04.027.

6. Allshire, R.C., and Karpen, G.H. (2008). Epigenetic regulation of centromeric chromatin: old dogs, new tricks? Nat. Rev. Genet. *9*, 923–937. https://doi.org/10.1038/nrg2466.

7. Yatskevich, S., Muir, K.W., Bellini, D., Zhang, Z., Yang, J., Tischer, T., Predin, M., Dendooven, T., McLaughlin, S.H., and Barford, D. (2022). Structure of the human inner kinetochore bound to a centromeric CENP-A nucleosome. Science *376*, 844–852. https://doi.org/10.1126/science.abn3810.

8. McKinley, K.L., Sekulic, N., Guo, L.Y., Tsinman, T., Black, B.E., and Cheeseman, I.M. (2015). The CENP-L-N complex forms a critical node in an integrated meshwork of interactions at the centromere-kinetochore interface. Mol. Cell *60*, 886–898. https://doi.org/10.1016/j.molcel.2015.10.027.

9. Amato, A., Schillaci, T., Lentini, L., and Di Leonardo, A. (2009). CENPA overexpression promotes genome instability in pRb-depleted human cells. Mol. Cancer *8*, 119. https://doi.org/10.1186/1476-4598-8-119.

10. Yu, Z.L., Zhou, X., Wang, W.J., Deng, W.Q., Fang, J.N., Hu, H., Wang, Z.C., Li, S.Z., Cui, L., Shen, J., et al. (2015). Dynamic phosphorylation of CENP-A at Ser68 orchestrates its cell-cycle-dependent deposition at centromeres. Dev. Cell *32*, 68–81. https://doi.org/10.1016/j.devcel.2014.11.030.

11. Renaud-Pageot, C., Quivy, J.P., Lochhead, M., and Almouzni, G. (2022). CENP-A regulation and cancer. Front. Cell Dev. Biol. *10*, 907120. https://doi.org/10.3389/fcell.2022.907120.

12. Black, B.E., and Cleveland, D.W. (2011). Epigenetic centromere propagation and the nature of CENP-a nucleosomes. Cell *144*, 471–479. https://doi.org/10.1016/j.cell.2011.02.002.

13. Holland, A.J., and Cleveland, D.W. (2009). Boveri revisited: chromosomal instability, aneuploidy and tumorigenesis. Nat. Rev. Mol. Cell Biol. *10*, 478–487. https://doi.org/10.1038/nrm2718.

14. Ramachandran, S., and Henikoff, S. (2015). Replicating nucleosomes. Sci. Adv. *1*, 1500587. https://doi.org/10.1126/sciadv.1500587.

15. Dunleavy, E.M., Almouzni, G., and Karpen, G.H. (2011). H3.3 is deposited at centromeres in S phase as a placeholder for newly assembled CENP-A in G_1 phase. Nucleus *2*, 146–157. https://doi.org/10.4161/nucl.2.2.15211.

16. Deal, R.B., Henikoff, J.G., and Henikoff, S. (2010). Genome-wide kinetics of nucleosome turnover determined by metabolic labeling of histones. Science *328*, 1161–1164. https://doi.org/10.1126/science.1186777.

17. Dion, M.F., Kaplan, T., Kim, M., Buratowski, S., Friedman, N., and Rando, O.J. (2007). Dynamics of replication-independent histone turnover in budding yeast. Science *315*, 1405–1408. https://doi.org/10.1126/science.1134053.

18. Dunleavy, E.M., Roche, D., Tagami, H., Lacoste, N., Ray-Gallet, D., Nakamura, Y., Daigo, Y., Nakatani, Y., and Almouzni-Pettinotti, G. (2009). HJURP is a cell-cycle-dependent maintenance and deposition factor of CENP-A at centromeres. Cell *137*, 485–497. https://doi.org/10.1016/j.cell.2009.02.040.

19. Foltz, D.R., Jansen, L.E.T., Bailey, A.O., Yates, J.R., 3rd, Bassett, E.A., Wood, S., Black, B.E., and Cleveland, D.W. (2009). Centromere-specific assembly of CENP-a nucleosomes is mediated by HJURP. Cell *137*, 472–484. https://doi.org/10.1016/j.cell.2009.02.039.

20. Takahashi, K., Chen, E.S., and Yanagida, M. (2000). Requirement of Mis6 centromere connector for localizing a CENP-A-like protein in fission yeast. Science *288*, 2215–2219. https://doi.org/10.1126/science.288.5474.2215.

21. McKinley, K.L., and Cheeseman, I.M. (2016). The molecular basis for centromere identity and function. Nat. Rev. Mol. Cell Biol. *17*, 16–29. https://doi.org/10.1038/nrm.2015.5.

22. Ling, Y.H., and Yuen, K.W.Y. (2019). Point centromere activity requires an optimal level of centromeric noncoding RNA. Proc. Natl. Acad. Sci. USA *116*, 6270–6279. https://doi.org/10.1073/pnas.1821384116.

23. Wong, L.H., Brettingham-Moore, K.H., Chan, L., Quach, J.M., Anderson, M.A., Northrop, E.L., Hannan, R., Saffery, R., Shaw, M.L., Williams, E., and Choo, K.H. (2007). Centromere RNA is a key component for the assembly of nucleoproteins at the nucleolus and centromere. Genome Res. *17*, 1146–1160. https://doi.org/10.1101/gr.6022807.

24. Bergmann, J.H., Jakubsche, J.N., Martins, N.M., Kagansky, A., Nakano, M., Kimura, H., Kelly, D.A., Turner, B.M., Masumoto, H., Larionov, V., and Earnshaw, W.C. (2012). Epigenetic engineering: histone H3K9 acetylation is compatible with kinetochore structure and function. J. Cell Sci. *125*, 411–421. https://doi.org/10.1242/jcs.090639.

25. Carlsten, J.O., Szilagyi, Z., Liu, B., Lopez, M.D., Szászi, E., Djupedal, I., Nyström, T., Ekwall, K., Gustafsson, C.M., and Zhu, X. (2012). Mediator promotes CENP-a incorporation at fission yeast centromeres. Mol. Cell. Biol. *32*, 4035–4043. https://doi.org/10.1128/MCB.00374-12.

26. Quénet, D., and Dalal, Y. (2014). A long non-coding RNA is required for targeting centromeric protein A to the human centromere. eLife *3*, e03254. https://doi.org/10.7554/eLife.03254.

27. Yilmaz, D., Furst, A., Meaburn, K., Lezaja, A., Wen, Y., Altmeyer, M., Reina-San-Martin, B., and Soutoglou, E. (2021). Activation of homologous recombination in G1 preserves centromeric integrity. Nature *600*, 748–753. https://doi.org/10.1038/s41586-021-04200-z.

28. Li, J.S.Z., Abbasi, A., Kim, D.H., Lippman, S.M., Alexandrov, L.B., and Cleveland, D.W. (2023). Chromosomal fragile site breakage by EBV-encoded EBNA1 at clustered repeats. Nature *616*, 504–509. https://doi.org/10.1038/s41586-023-05923-x.

29. Ting, D.T., Lipson, D., Paul, S., Brannigan, B.W., Akhavanfard, S., Coffman, E.J., Contino, G., Deshpande, V., Iafrate, A.J., Letovsky, S., et al. (2011). Aberrant overexpression of satellite repeats in pancreatic and other epithelial cancers. Science *331*, 593–596. https://doi.org/10.1126/science.1200801.

30. Wang, X., Zhao, B.S., Roundtree, I.A., Lu, Z., Han, D., Ma, H., Weng, X., Chen, K., Shi, H., and He, C. (2015). N^6-methyladenosine modulates messenger RNA translation efficiency. Cell *161*, 1388–1399. https://doi.org/10.1016/j.cell.2015.05.014.

31. Wang, X., Lu, Z., Gomez, A., Hon, G.C., Yue, Y., Han, D., Fu, Y., Parisien, M., Dai, Q., Jia, G., et al. (2014). N^6-methyladenosine-dependent regulation of messenger RNA stability. Nature *505*, 117–120. https://doi.org/10.1038/nature12730.

32. Xiao, W., Adhikari, S., Dahal, U., Chen, Y.S., Hao, Y.J., Sun, B.F., Sun, H.Y., Li, A., Ping, X.L., Lai, W.Y., et al. (2016). Nuclear m^6A reader YTHDC1 regulates mRNA splicing. Mol. Cell *61*, 507–519. https://doi.org/10.1016/j.molcel.2016.01.012.

33. Yang, Y., Hsu, P.J., Chen, Y.S., and Yang, Y.G. (2018). Dynamic transcriptomic m^6A decoration: writers, erasers, readers and functions in RNA metabolism. Cell Res. *28*, 616–624. https://doi.org/10.1038/s41422-018-0040-8.

34. Xu, W.Q., He, C.X., Kaye, E.G., Li, J.H., Mu, M.D., Nelson, G.M., Dong, L., Wang, J.H., Wu, F.Z., Shi, Y.G., et al. (2022). Dynamic control of chromatin-associated m^6A methylation regulates nascent RNA synthesis.

Mol. Cell *82*, 1156–1168.e7. https://doi.org/10.1016/j.molcel.2022.02.006.

35. Dou, X.Y., Xiao, Y., Shen, C., Wang, K., Wu, T., Liu, C., Li, Y.N., Yu, X.B., Liu, J., Dai, Q., et al. (2023). RBFOX2 recognizes N^6-methyladenosine to suppress transcription and block myeloid leukaemia differentiation. Nat. Cell Biol. *25*, 1359–1368. https://doi.org/10.1038/s41556-023-01213-w.
36. Liu, J., Dou, X., Chen, C., Chen, C., Liu, C., Xu, M.M., Zhao, S., Shen, B., Gao, Y., Han, D., and He, C. (2020). N^6-methyladenosine of chromosome-associated regulatory RNA regulates chromatin state and transcription. Science *367*, 580–586. https://doi.org/10.1126/science.aay6018.
37. Liu, P.Y., Li, F.M., Lin, J.H., Fukumoto, T., Nacarelli, T., Hao, X., Kossenkov, A.V., Simon, M.C., and Zhang, R.G. (2021). m^6A-independent genome-wide METTL3 and METTL14 redistribution drives the senescence-associated secretory phenotype. Nat. Cell Biol. *23*, 355–365. https://doi.org/10.1038/s41556-021-00656-3.
38. Xiao, Y., Wang, Y., Tang, Q., Wei, L.H., Zhang, X., and Jia, G.F. (2018). An elongation- and ligation-based qPCR amplification method for the radiolabeling-free detection of locus-specific N^6-methyladenosine modification. Angew. Chem. Int. Ed. Engl. *57*, 15995–16000. https://doi.org/10.1002/anie.201807942.
39. Chu, C., Qu, K., Zhong, F.L., Artandi, S.E., and Chang, H.Y. (2011). Genomic maps of long noncoding RNA occupancy reveal principles of RNA-chromatin interactions. Mol. Cell *44*, 667–678. https://doi.org/10.1016/j.molcel.2011.08.027.
40. Wei, J., Yu, X., Yang, L., Liu, X., Gao, B., Huang, B., Dou, X., Liu, J., Zou, Z., Cui, X.L., et al. (2022). FTO mediates LINE1 m^6A demethylation and chromatin regulation in mESCs and mouse development. Science *376*, 968–973. https://doi.org/10.1126/science.abe9582.
41. Li, J.X., Chen, Z.J., Chen, F., Xie, G.Y., Ling, Y.Y., Peng, Y.X., Lin, Y., Luo, N., Chiang, C.M., and Wang, H.S. (2020). Targeted mRNA demethylation using an engineered dCas13b-ALKBH5 fusion protein. Nucleic Acids Res. *48*, 5684–5694. https://doi.org/10.1093/nar/gkaa269.
42. Xu, Y., Wang, Y.F., and Liang, F.S. (2023). Site-specific m^6A erasing via conditionally stabilized CRISPR-Cas13b editor. Angew. Chem. Int. Ed. Engl. *62*, e202309291. https://doi.org/10.1002/anie.202309291.
43. Rauch, S., He, C., and Dickinson, B.C. (2018). Targeted m^6A reader proteins to study epitranscriptomic regulation of single RNAs. J. Am. Chem. Soc. *140*, 11974–11981. https://doi.org/10.1021/jacs.8b05012.
44. Shao, W., Bi, X.J., Pan, Y.X., Gao, B.Y., Wu, J., Yin, Y.F., Liu, Z.M., Peng, M.Y., Zhang, W.H., Jiang, X., et al. (2022). Phase separation of RNA-binding protein promotes polymerase binding and transcription. Nat. Chem. Biol. *18*, 70–80. https://doi.org/10.1038/s41589-021-00904-5.
45. Hammond, C.M., Strømme, C.B., Huang, H., Patel, D.J., and Groth, A. (2017). Histone chaperone networks shaping chromatin function. Nat. Rev. Mol. Cell Biol. *18*, 141–158. https://doi.org/10.1038/nrm.2016.159.
46. Jansen, L.E.T., Black, B.E., Foltz, D.R., and Cleveland, D.W. (2007). Propagation of centromeric chromatin requires exit from mitosis. J. Cell Biol. *176*, 795–805. https://doi.org/10.1083/jcb.200701066.
47. Wang, H., Xu, Z., Mao, S., and Granick, S. (2022). Experimental guidelines to image transient single-molecule events using graphene liquid cell electron microscopy. ACS Nano *16*, 18526–18537. https://doi.org/10.1021/acsnano.2c06766.
48. Li, P.P., and Liu, Z.P. (2023). GeoBind: segmentation of nucleic acid binding interface on protein surface with geometric deep learning. Nucleic Acids Res. *51*, e60. https://doi.org/10.1093/nar/gkad288.
49. Lam, J.H., Li, Y., Zhu, L.Z., Umarov, R., Jiang, H.L., Héliou, A., Sheong, F.K., Liu, T.Y., Long, Y.K., Li, Y.F., et al. (2019). A deep learning framework to predict binding preference of RNA constituents on protein surface. Nat. Commun. *10*, 4941. https://doi.org/10.1038/s41467-019-12920-0.
50. Shu, X., Liu, M., Lu, Z., Zhu, C., Meng, H., Huang, S., Zhang, X., and Yi, C. (2018). Genome-wide mapping reveals that deoxyuridine is enriched in the human centromeric DNA. Nat. Chem. Biol. *14*, 680–687. https://doi.org/10.1038/s41589-018-0065-9.
51. Kabeche, L., Nguyen, H.D., Buisson, R., and Zou, L. (2018). A mitosis-specific and R loop-driven ATR pathway promotes faithful chromosome segregation. Science *359*, 108–114. https://doi.org/10.1126/science.aan6490.
52. Zeng, J.K., Hills, S.A., Ozono, E., and Diffley, J.F.X. (2023). Cyclin E-induced replicative stress drives p53-dependent whole-genome duplication. Cell *186*, 528–542.e14. https://doi.org/10.1016/j.cell.2022.12.036.
53. Yankova, E., Blackaby, W., Albertella, M., Rak, J., De Braekeleer, E., Tsagkogeorga, G., Pilka, E.S., Aspris, D., Leggate, D., Hendrick, A.G., et al. (2021). Small-molecule inhibition of METTL3 as a strategy against myeloid leukaemia. Nature *593*, 597–601. https://doi.org/10.1038/s41586-021-03536-w.
54. Yang, J., Ikezoe, T., Nishioka, C., Tasaka, T., Taniguchi, A., Kuwayama, Y., Komatsu, N., Bandobashi, K., Togitani, K., Koeffler, H.P., et al. (2007). AZD1152, a novel and selective aurora B kinase inhibitor, induces growth arrest, apoptosis, and sensitization for tubulin depolymerizing agent or topoisomerase II inhibitor in human acute leukemia cells in vitro and in vivo. Blood *110*, 2034–2040. https://doi.org/10.1182/blood-2007-02-073700.
55. Martens, S., Goossens, V., Devisscher, L., Hofmans, S., Claeys, P., Vuylsteke, M., Takahashi, N., Augustyns, K., and Vandenabeele, P. (2018). RIPK1-dependent cell death: a novel target of the Aurora kinase inhibitor Tozasertib (VX-680). Cell Death Dis. *9*, 211. https://doi.org/10.1038/s41419-017-0245-7.
56. McNulty, S.M., and Sullivan, B.A. (2018). Alpha satellite DNA biology: finding function in the recesses of the genome. Chromosome Res. *26*, 115–138. https://doi.org/10.1007/s10577-018-9582-3.
57. Hildebrand, E.M., and Biggins, S. (2016). Regulation of budding yeast CENP-A levels prevents misincorporation at promoter nucleosomes and transcriptional defects. PLoS Genet. *12*, e1005930. https://doi.org/10.1371/journal.pgen.1005930.
58. Popchock, A.R., Larson, J.D., Dubrulle, J., Asbury, C.L., and Biggins, S. (2023). Direct observation of coordinated assembly of individual native centromeric nucleosomes. EMBO J. *42*, e114534. https://doi.org/10.15252/embj.2023114534.
59. Xiao, H., Mizuguchi, G., Wisniewski, J., Huang, Y., Wei, D., and Wu, C. (2011). Nonhistone Scm3 binds to AT-rich DNA to organize atypical centromeric nucleosome of budding yeast. Mol. Cell *43*, 369–380. https://doi.org/10.1016/j.molcel.2011.07.009.
60. Kunkel, G.R., and Martinson, H.G. (1981). Nucleosomes will not form on double-stranded RNa or over poly(dA).poly(dT) tracts in recombinant DNA. Nucleic Acids Res. *9*, 6869–6888. https://doi.org/10.1093/nar/9.24.6869.
61. Bielski, C.M., and Taylor, B.S. (2021). Homing in on genomic instability as a therapeutic target in cancer. Nat. Commun. *12*, 3663. https://doi.org/10.1038/s41467-021-23965-5.
62. Andor, N., Maley, C.C., and Ji, H.P. (2017). Genomic instability in cancer: teetering on the limit of tolerance. Cancer Res. *77*, 2179–2185. https://doi.org/10.1158/0008-5472.CAN-16-1553.
63. Andor, N., Graham, T.A., Jansen, M., Xia, L.C., Aktipis, C.A., Petritsch, C., Ji, H.P., and Maley, C.C. (2016). Pan-cancer analysis of the extent and consequences of intratumor heterogeneity. Nat. Med. *22*, 105–113. https://doi.org/10.1038/nm.3984.
64. Marquis, C., Fonseca, C.L., Queen, K.A., Wood, L., Vandal, S.E., Malaby, H.L.H., Clayton, J.E., and Stumpff, J. (2021). Chromosomally unstable tumor cells specifically require KIF18A for proliferation. Nat. Commun. *12*, 1213. https://doi.org/10.1038/s41467-021-21447-2.
65. Zhou, B., Wang, L., Zhang, S., Bennett, B.D., He, F., Zhang, Y., Xiong, C., Han, L., Diao, L., Li, P., et al. (2016). INO80 governs superenhancer-

mediated oncogenic transcription and tumor growth in melanoma. Genes Dev. *30*, 1440–1453. https://doi.org/10.1101/gad.277178.115.

66. Martin, M. (2011). Cutadapt removes adapter sequences from high-throughput sequencing reads. EMBnet J. *17*, 10–12. https://doi.org/10.14806/ej.17.1.200.

67. Bolger, A.M., Lohse, M., and Usadel, B. (2014). Trimmomatic: a flexible trimmer for Illumina sequence data. Bioinformatics *30*, 2114–2120. https://doi.org/10.1093/bioinformatics/btu170.

68. Langmead, B., and Salzberg, S.L. (2012). Fast gapped-read alignment with Bowtie 2. Nat. Methods *9*, 357–359. https://doi.org/10.1038/nmeth.1923.

69. Kim, D., Paggi, J.M., Park, C., Bennett, C., and Salzberg, S.L. (2019). Graph-based genome alignment and genotyping with HISAT2 and HISAT-genotype. Nat. Biotechnol. *37*, 907–915. https://doi.org/10.1038/s41587-019-0201-4.

70. Li, H., and Durbin, R. (2009). Fast and accurate short read alignment with Burrows-Wheeler transform. Bioinformatics *25*, 1754–1760. https://doi.org/10.1093/bioinformatics/btp324.

71. Danecek, P., Bonfield, J.K., Liddle, J., Marshall, J., Ohan, V., Pollard, M.O., Whitwham, A., Keane, T., McCarthy, S.A., Davies, R.M., and Li, H. (2021). Twelve years of SAMtools and BCFtools. GigaScience *10*, giab008. https://doi.org/10.1093/gigascience/giab008.

72. Zhang, Y., Liu, T., Meyer, C.A., Eeckhoute, J., Johnson, D.S., Bernstein, B.E., Nusbaum, C., Myers, R.M., Brown, M., Li, W., and Liu, X.S. (2008). Model-based analysis of ChIP-Seq (MACS). Genome Biol. *9*, R137. https://doi.org/10.1186/gb-2008-9-9-r137.

73. Quinlan, A.R., and Hall, I.M. (2010). BEDTools: a flexible suite of utilities for comparing genomic features. Bioinformatics *26*, 841–842. https://doi.org/10.1093/bioinformatics/btq033.

74. Ramírez, F., Ryan, D.P., Grüning, B., Bhardwaj, V., Kilpert, F., Richter, A.S., Heyne, S., Dündar, F., and Manke, T. (2016). deepTools2: a next generation web server for deep-sequencing data analysis. Nucleic Acids Res. *44*, W160–W165. https://doi.org/10.1093/nar/gkw257.

75. Heinz, S., Benner, C., Spann, N., Bertolino, E., Lin, Y.C., Laslo, P., Cheng, J.X., Murre, C., Singh, H., and Glass, C.K. (2010). Simple combinations of lineage-determining transcription factors prime cis-regulatory elements required for macrophage and B cell identities. Mol. Cell *38*, 576–589. https://doi.org/10.1016/j.molcel.2010.05.004.

76. Liao, Y., Smyth, G.K., and Shi, W. (2014). featureCounts: an efficient general purpose program for assigning sequence reads to genomic features. Bioinformatics *30*, 923–930. https://doi.org/10.1093/bioinformatics/btt656.

77. DePristo, M.A., Banks, E., Poplin, R., Garimella, K.V., Maguire, J.R., Hartl, C., Philippakis, A.A., del Angel, G., Rivas, M.A., Hanna, M., et al. (2011). A framework for variation discovery and genotyping using next-generation DNA sequencing data. Nat. Genet. *43*, 491–498. https://doi.org/10.1038/ng.806.

78. Talevich, E., Shain, A.H., Botton, T., and Bastian, B.C. (2016). CNVkit: genome-wide copy number detection and visualization from targeted DNA sequencing. PLoS Comput. Biol. *12*, e1004873. https://doi.org/10.1371/journal.pcbi.1004873.

79. Chen, K., Wallis, J.W., McLellan, M.D., Larson, D.E., Kalicki, J.M., Pohl, C.S., McGrath, S.D., Wendl, M.C., Zhang, Q., Locke, D.P., et al. (2009). BreakDancer: an algorithm for high-resolution mapping of genomic structural variation. Nat. Methods *6*, 677–681. https://doi.org/10.1038/nmeth.1363.

80. Wang, K., Li, M., and Hakonarson, H. (2010). ANNOVAR: functional annotation of genetic variants from high-throughput sequencing data. Nucleic Acids Res. *38*, e164. https://doi.org/10.1093/nar/gkq603.

81. Robinson, J.T., Thorvaldsdóttir, H., Winckler, W., Guttman, M., Lander, E.S., Getz, G., and Mesirov, J.P. (2011). Integrative genomics viewer. Nat. Biotechnol. *29*, 24–26. https://doi.org/10.1038/nbt.1754.

82. Lin, Y.F., Hu, Q., Mazzagatti, A., Valle-Inclán, J.E., Maurais, E.G., Dahiya, R., Guyer, A., Sanders, J.T., Engel, J.L., Nguyen, G., et al. (2023). Mitotic clustering of pulverized chromosomes from micronuclei. Nature *618*, 1041–1048. https://doi.org/10.1038/s41586-023-05974-0.

83. Tucker, J.B., Bonema, S.C., García-Varela, R., Denu, R.A., Hu, Y., McGregor, S.M., Burkard, M.E., and Weaver, B.A. (2023). Misaligned chromosomes are a major source of chromosomal instability in breast cancer. Cancer Res Commun. *3*, 54–65. https://doi.org/10.1158/2767-9764.CRC-22-0302.

84. Wuarin, J., and Schibler, U. (1994). Physical isolation of nascent Rna chains transcribed by Rna-polymerase-II: Evidence for cotranscriptional splicing. Mol. Cell. Biol. *14*, 7219–7225. https://doi.org/10.1128/mcb.14.11.7219-7225.1994.

85. Gu, Z.G., Gu, L., Eils, R., Schlesner, M., and Brors, B. (2014). circlize Implements and enhances circular visualization in R. Bioinformatics *30*, 2811–2812. https://doi.org/10.1093/bioinformatics/btu393.

86. Sullivan, B.A. (2010). Optical mapping of protein-DNA complexes on chromatin fibers. Methods Mol. Biol. *659*, 99–115. https://doi.org/10.1007/978-1-60761-789-1_7.

87. Dominissini, D., Moshitch-Moshkovitz, S., Schwartz, S., Salmon-Divon, M., Ungar, L., Osenberg, S., Cesarkas, K., Jacob-Hirsch, J., Amariglio, N., Kupiec, M., et al. (2012). Topology of the human and mouse m^6A RNA methylomes revealed by m^6A-seq. Nature *485*, 201–206. https://doi.org/10.1038/nature11112.

88. Jumper, J., Evans, R., Pritzel, A., Green, T., Figurnov, M., Ronneberger, O., Tunyasuvunakool, K., Bates, R., Zídek, A., Potapenko, A., et al. (2021). Highly accurate protein structure prediction with AlphaFold. Nature *596*, 583–589. https://doi.org/10.1038/s41586-021-03819-2.

89. Varadi, M., Anyango, S., Deshpande, M., Nair, S., Natassia, C., Yordanova, G., Yuan, D., Stroe, O., Wood, G., Laydon, A., et al. (2022). AlphaFold protein structure database: massively expanding the structural coverage of protein-sequence space with high-accuracy models. Nucleic Acids Res. *50*, D439–D444. https://doi.org/10.1093/nar/gkab1061.

90. Marklund, E., Ke, Y.X., and Greenleaf, W.J. (2023). High-throughput biochemistry in RNA sequence space: predicting structure and function. Nat. Rev. Genet. *24*, 401–414. https://doi.org/10.1038/s41576-022-00567-5.

91. Sekulic, N., Bassett, E.A., Rogers, D.J., and Black, B.E. (2010). The structure of $(CENP\text{-}A\text{-}H4)_2$ reveals physical features that mark centromeres. Nature *467*, 347–351. https://doi.org/10.1038/nature09323.

92. Yan, Y.M., Tao, H.Y., He, J.H., and Huang, S.Y. (2020). The HDOCK server for integrated protein-protein docking. Nat. Protoc. *15*, 1829–1852. https://doi.org/10.1038/s41596-020-0312-x.

93. Zhang, Y., Xiong, Y.D., and Xiao, Y. (2022). 3dDNA: A computational method of building DNA 3D structures. Molecules *27*, 5936. https://doi.org/10.3390/molecules27185936.

94. Di Tommaso, P., Moretti, S., Xenarios, I., Orobitg, M., Montanyola, A., Chang, J.M., Taly, J.F., and Notredame, C. (2011). T-Coffee: a web server for the multiple sequence alignment of protein and RNA sequences using structural information and homology extension. Nucleic Acids Res. *39*, W13–W17. https://doi.org/10.1093/nar/gkr245.

95. Senderowicz, A.M. (1999). Flavopiridol: the first cyclin-dependent kinase inhibitor in human clinical trials. Invest New Drugs *17*, 313–320. https://doi.org/10.1023/a:1006353008903.

96. Byth, K.F., Thomas, A., Hughes, G., Forder, C., McGregor, A., Geh, C., Oakes, S., Green, C., Walker, M., Newcombe, N., et al. (2009). AZD5438, a potent oral inhibitor of cyclin-dependent kinases 1, 2, and 9, leads to pharmacodynamic changes and potent antitumor effects in human tumor xenografts. Mol. Cancer Ther. *8*, 1856–1866. https://doi.org/10.1158/1535-7163.MCT-08-0836.

97. Jost, M., Chen, Y., Gilbert, L.A., Horlbeck, M.A., Krenning, L., Menchon, G., Rai, A., Cho, M.Y., Stern, J.J., Prota, A.E., et al. (2020).

Pharmaceutical-grade rigosertib is a microtubule-destabilizing agent. Mol. Cell *79*, 191–198.e3. https://doi.org/10.1016/j.molcel.2020.06.008.

98. Conroy, A., Stockett, D.E., Walker, D., Arkin, M.R., Hoch, U., Fox, J.A., and Hawtin, R.E. (2009). SNS-032 is a potent and selective CDK 2, 7 and 9 inhibitor that drives target modulation in patient samples. Cancer Chemother. Pharmacol. *64*, 723–732. https://doi.org/10.1007/s00280-008-0921-5.

99. Bongero, D., Paoluzzi, L., Marchi, E., Zullo, K.M., Neisa, R., Mao, Y., Escandon, R., Wood, K., and O'Connor, O.A. (2015). The novel kinesin spindle protein (KSP) inhibitor SB-743921 exhibits marked activity in in vivo and in vitro models of aggressive large B-cell lymphoma. Leuk. Lymphoma *56*, 2945–2952. https://doi.org/10.3109/10428194.2015.1020058.

100. Zabludoff, S.D., Deng, C., Grondine, M.R., Sheehy, A.M., Ashwell, S., Caleb, B.L., Green, S., Haye, H.R., Horn, C.L., Janetka, J.W., et al. (2008). AZD7762, a novel checkpoint kinase inhibitor, drives checkpoint abrogation and potentiates DNA-targeted therapies. Mol. Cancer Ther. *7*, 2955–2966. https://doi.org/10.1158/1535-7163.MCT-08-0492.

101. O'Leary, J.J., Shapiro, R.L., Ren, C.J., Chuang, N., Cohen, H.W., and Potmesil, M. (1999). Antiangiogenic effects of camptothecin analogues 9-amino-20(S)-camptothecin, topotecan, and CPT-11 studied in the mouse cornea model. Clin. Cancer Res. *5*, 181–187.

102. Durant, S.T., Zheng, L., Wang, Y., Chen, K., Zhang, L., Zhang, T., Yang, Z., Riches, L., Trinidad, A.G., Fok, J.H.L., et al. (2018). The brain-penetrant clinical ATM inhibitor AZD1390 radiosensitizes and improves survival of preclinical brain tumor models. Sci. Adv. *4*, eaat1719. https://doi.org/10.1126/sciadv.aat1719.

103. Palmer, D.H., Ross, P.J., Silcocks, P., Greenhalf, W., Faluyi, O.O., Ma, Y.T., Wadsley, J., Rawcliffe, C.L., Valle, J.W., and Neoptolemos, J.P. (2018). ACELARATE: A phase III, open label, multicentre randomised clinical study comparing Acelarin (NUC-1031) with gemcitabine in patients with metastatic pancreatic carcinoma. J. Clin. Oncol. *36*, TPS537. https://doi.org/10.1200/JCO.2018.36.4_suppl.TPS537.

104. Lheureux, S., Cristea, M.C., Bruce, J.P., Garg, S., Cabanero, M., Mantia-Smaldone, G., Olawaiye, A.B., Ellard, S.L., Weberpals, J.I., Wahner Hendrickson, A.E., et al. (2021). Adavosertib plus gemcitabine for platinum-resistant or platinum-refractory recurrent ovarian cancer: a double-blind, randomised, placebo-controlled, phase 2 trial. Lancet *397*, 281–292. https://doi.org/10.1016/S0140-6736(20)32554-X.

105. Liu, Y., Norton, J.T., Witschi, M.A., Xu, Q., Lou, G., Wang, C., Appella, D.H., Chen, Z., and Huang, S. (2011). Methoxyethylamino-numonafide is an efficacious and minimally toxic amonafide derivative in murine models of human cancer. Neoplasia *13*, 453–460. https://doi.org/10.1593/neo.101738.

106. Wengner, A.M., Siemeister, G., Lücking, U., Lefranc, J., Wortmann, L., Lienau, P., Bader, B., Bömer, U., Moosmayer, D., Eberspächer, U., et al. (2020). The novel ATR inhibitor BAY 1895344 is efficacious as monotherapy and combined with DNA damage-inducing or repair-compromising therapies in preclinical cancer models. Mol. Cancer Ther. *19*, 26–38. https://doi.org/10.1158/1535-7163.MCT-19-0019.

107. Faulds, D., Balfour, J.A., Chrisp, P., and Langtry, H.D. (1991). Mitoxantrone. A review of its pharmacodynamic and pharmacokinetic properties, and therapeutic potential in the chemotherapy of cancer. Drugs *41*, 400–449. https://doi.org/10.2165/00003495-199141030-00007.

108. Ketron, A.C., Denny, W.A., Graves, D.E., and Osheroff, N. (2012). Amsacrine as a topoisomerase II poison: importance of drug-DNA interactions. Biochemistry *51*, 1730–1739. https://doi.org/10.1021/bi201159b.

STAR★METHODS

KEY RESOURCES TABLE

REAGENT or RESOURCE	SOURCE	IDENTIFIER
Antibodies		
Rabbit monoclonal anti-METTL3	Abcam	Cat# ab195352; RRID: AB_2721254
Rabbit monoclonal anti-N^6-Methyladenosine	NEB	Cat# E1610S; RRID: AB_2923416
Rabbit monoclonal anti-CENPA	Abcam	Cat# ab45694; RRID: AB_726799
Rabbit monoclonal anti-CENPA	Beyotime	Cat# AC301; RRID: N/A
Mouse monoclonal anti-gamma H2A.X	Abcam	Cat# ab22551; RRID: AB_447150
Rabbit monoclonal anti-gamma H2A.X	Abcam	Cat# ab81299; RRID: AB_1640564
Mouse monoclonal anti-GAPDH	Proteintech	Cat# HRP-60004; RRID: AB_2737588
Rabbit polyclonal anti-H3	Abcam	Cat# ab1791; RRID: AB_302613
Rabbit polyclonal anti-SNRP70	Abcam	Cat# ab83306; RRID: AB_10673827
Mouse monoclonal anti-β-Actin	CST	Cat# 3700S; RRID: AB_2242334
Mouse monoclonal anti-β-Tubulin	Abmart	Cat# M20005; RRID: AB_2920648
Rabbit monoclonal anti-H4	Beyotime	Cat# AF2581; RRID:N/A
Rabbit monoclonal anti-H3.3	Beyotime	Cat# AF1813; RRID: N/A
Rabbit monoclonal anti-DAXX	Beyotime	Cat# AF2077; RRID: N/A
Rabbit monoclonal anti-H3 (phospho S10)	Abcam	Cat# ab267372; RRID: AB_2934071
Donkey anti-Rabbit Alexa Fluor™ 488	Thermo Fisher	Cat# A-21206; RRID: AB_2535792
Goat anti-Mouse Alexa Fluor™ 594	Thermo Fisher	Cat# A-11005; RRID: AB_2534073
Donkey anti-Rabbit Alexa Fluor™ 647	Thermo Fisher	Cat# A-31573; RRID: AB_2536183
Bacterial and Virus Strains		
BL21	Agilent Technologies	Cat# 230280
DH5α	Sangon Biotech	Cat# B528413
Chemicals, Peptides, and Recombinant Proteins		
DMEM	GIBCO	Cat# 11965
Pen-Strep	Millipore	Cat# TMS-AB2-C
Fetal Bovine Serum	Gemini	Cat# 900-108
L-Glutamine	GIBCO	Cat# 25030081
Trypsin-EDTA	GIBCO	Cat# 15400054
DPBS	GIBCO	Cat# 14190250
Opti-MEM™ I Reduced Serum Medium	GIBCO	Cat# 31985070
Lipofectamine™ 2000 Reagent	Thermo	Cat# 11668019
Bovine Serum Albumin	Sigma	Cat# B2064
Dimethyl sulfoxide	Sigma	Cat# D2650
TRIzol™ Reagent	Invitrogen	Cat# 15596026
Chloroform	Sigma	Cat# C2432-500ML
Doxycycline hyclate	Sigma	Cat# D9891
DTT	Sigma	Cat# D0632
Imidazole	Sigma	Cat# I2399
Protease Inhibitor Cocktail	Sigma	Cat# P8849
Puromycin	Sigma	Cat# 540411
Polybrene	Sigma	Cat# TR-1003
Pierce™ Protein G Magnetic Beads	Thermo	Cat# 88848
Pierce™ Protein A Magnetic Beads	Thermo	Cat# 88846

(*Continued on next page*)

Continued

REAGENT or RESOURCE	SOURCE	IDENTIFIER
AMPure XP	BECKMAN	Cat# A63881
DNA clean beads	Vazyme	Cat# N411-02
Dynabeads™ MyOne™ Streptavidin C1	Invitrogen	Cat# 65002
Dynabeads™ Oligo (dT)	Invitrogen	Cat# 61002
Glycerol	ABCONE	Cat# G46055
HEPES	ABCONE	Cat# H33755
TWEEN® 20	ABCONE	Cat# P87875
Triton™ X-100	Sigma	Cat# X100-500ML
Agarose	ABCONE	Cat# A47902
Ampicillin	Sangon Biotech	Cat# B541011
PMSF	Beyotime	Cat# ST506
Proteinase K	Invitrogen	Cat# 25530015
DNase I	New England Biolabs	Cat# M0303
RNAase A	Thermo	Cat# EN0531
RiboLock RNase inhibitor	Thermo	Cat# EO0384
UltraPure™ DNase/RNase-Free Distilled Water	Invitrogen	Cat# 10977015
Thymidine	Beyotime	Cat# ST1704
M5 Protease Inhibitor Cocktail, EDTA-free	Mei5bio	Cat# MF182
2× RNA Loading Dye	NEB	Cat# B0363S
Ficoll®	Sigma	Cat# F9378
Xylene Cyanol FF	Sigma	Cat# X4126
Bromophenol Blue	Macklin	Cat# B873344
DNA Degradase Plus™	Zymo	Cat# E2021
BsmI	NEB	Cat# R0134L
UDG	NEB	Cat# M0280S
SNAP-Cell® TMR-Star	NEB	Cat# S9105
SNAP-Cell® block	NEB	Cat# S9106
Acetonitrile	Macklin	Cat# A800361
Dynabeads™ MyOne™ Silane	Invitrogen™	Cat# 37002D
Bst 2.0 DNA Polymerase	NEB	Cat# M0537
SplintR® Ligase	NEB	Cat# M0375
Deoxynucleotide (dNTP) Solution Mix	NEB	Cat# N0447
Adenosine 5'-Triphosphate (ATP)	NEB	Cat# P0756
Nuclease P1	Fujifilm Wako	Cat# 145-08221
PEG 8000	Solarbio	Cat# P8260
Bio-N^6-ddATP	ENZO	Cat# ENZ-42809
Terminal Transferase	NEB	Cat# M0315
4% Paraformaldehyde Fix Solution (PFA)	BBI	Cat# E672002-0100
0.1% Crystal Violet	Solarbio	Cat# G1063
Immobilon®-P Membrane, PVDF, 0.45 mm	Millipore	Cat# IPVH07850
HYBOND®-N+	GE	Cat# RPN303B
DSP	BBI	Cat# C110213
BeyoECL Plus	Beyotime	Cat# P0018A
MG-132	MCE	Cat# HY-13259
Cycloheximide	KL	Cat# KL13255
Critical Commercial Assays		
DNA Clean & Concentrator Kits	Zymo	Cat# DP4033
RNA Clean & Concentrator Kits	Zymo	Cat# R1017

(*Continued on next page*)

Continued

REAGENT or RESOURCE	SOURCE	IDENTIFIER
BeyoClick™ EdU Cell Proliferation Kit with Alexa Fluor 488	Beyotime	Cat# C0071
TransNGS® rRNA Depletion Kit (Human/Mouse/Rat)	TransGen	Cat# KD101
DeadEnd™ Fluorometric TUNEL System	Promega	Cat# G3250
VAHTS Stranded mRNA-seq Library Prep Kits	Vazyme Biotech Co.,Ltd	Cat# NR605
Ribo-off Globin & rRNA Depletion Kit (Human/Mouse/Rat)	Vazyme Biotech Co.,Ltd	Cat# N408
Clonech SMARTer® Stranded Total RNA-Seq Kit v2 - Pico Input Mammalian	Takara	Cat# 634413
Chemiluminescent Nucleic Acid Detection Module Kit	Thermo	Cat# 89880
VAHTS Universal Pro DNA Library Prep Kit for Illumina	Vazyme Biotech Co.,Ltd	Cat# ND608
Deposited Data		
caRNA m^{6}A-seq in A375 cells	This paper	GEO: GSE230880
ChIRP-seq in A375 cells	This paper	GEO: GSE230880
ChIP-seq in A375 cells	This paper	GEO: GSE230880
RIP-seq in A375 cells	This paper	GEO: GSE230880
WGS in A375 cells	This paper	SRA: PRJNA962808
caRNA m^{6}A-seq in HEK293T cells	This paper	GEO: GSE230880
H3K27ac ChIP-seq data in A375 cells	Zhou et al.[65]	GEO: GSE82332
H3K27ac ChIP-seq data in HEC-1-A cells	Liu et al.[36]	GEO: GSE140557
caRNA m^{6}A-seq in MCF7 cells	Xu et al.[34]	GEO: GSE196564
caRNA m^{6}A-seq in IMR90 cells	Liu et al.[37]	GEO: GSE159550
caRNA m^{6}A-seq in HepG2 cells	Dou et al.[35]	GEO: GSE205709
caRNA m^{6}A-seq in K562 cells	Dou et al.[35]	GEO: GSE205709
caRNA m^{6}A-seq in HEC-1-A cells	Liu et al.[36]	GEO: GSE140557
Experimental Models: Cell Lines		
HEK293T	N/A	N/A
A375	N/A	N/A
HuCCT1	N/A	N/A
IMR90	N/A	N/A
Oligonucleotides		
shRNA target sequences: h*METTL3* shRNA1: CCGGGCCAAGGAACAATCCATTGTTCTCGAGAACAATGGATTGTTCCTTGGCTTTTTG	This paper	N/A
shRNA target sequences: h*METTL3* shRNA2: CCGGGCTGCACTTCAGACGAATTATCTCGAGATAATTCGTCTGAAGTGCAGCTTTTTG	This paper	N/A
shRNA target sequences: h*CENPA* shRNA1: CCGGCCTCTGTAACAGAGGTAATATCTCGAGATATTACCTCTGTTACAGAGGTTTTTG	This paper	N/A
shRNA target sequences: h*CENPA* shRNA2: CCGGGCAGCAGAAGCATTTCTAGTTCTCGAGAACTAGAAATGCTTCTGCTGCTTTTTG	This paper	N/A
Centromeric probe: ATTCGTTGGAAACGGGA	PNA bio	Cat# F3004
Other primers, probes, and guide RNA sequences, see Table S1 and S2	This paper	N/A
Recombinant DNA		
pLKO.1-TRC	N/A	N/A
pTRE-EGFP	Gift from Peng Du	N/A
pLVX-Tet3G	Gift from Peng Du	N/A
psPAX2	N/A	N/A
pMD2.G	N/A	N/A

(*Continued on next page*)

Continued		
REAGENT or RESOURCE	SOURCE	IDENTIFIER
pTRE-METTL3^{wt}-EGFP	This paper	N/A
pTRE-METTL3^{mut}-EGFP	This paper	N/A
pTRE-CENPA^{wt}-EGFP	This paper	N/A
pTRE-CENPA^{mut}-EGFP	This paper	N/A
pTRE-EGFP	N/A	N/A
dCas13b-FTO-mCherry	Gift from Chuan He	N/A
PspCas13b crRNA backbone	Gift from Chuan He	N/A
PspCas13b centro gRNAs	This paper	N/A
PspCas13b nontarget gRNA	This paper	N/A
Delta 8.9	N/A	N/A
VSV-G	N/A	N/A
SNAP-TAG-CENPA	Gift from Guohong Li	N/A
SNAP-TAG-H3.3	This paper	N/A
pETDuet-6H-CENPA-H4	Gift from Guohong Li	N/A
pETDuet-6H-CENPA^{muts}-H4	This paper	N/A
Software and Algorithms		
GraphPad Prism	https://www.graphpad.com	https://www.graphpad.com
Fiji/ImageJ	https://imagej.net/Fiji	https://imagej.net/Fiji
FastQC v0.11.9	https://www.bioinformatics.babraham.ac.uk/projects/fastqc/	(https://www.bioinformatics.babraham.ac.uk/projects/fastqc/)
Trim Galore! v0.6.6	Martin[66]	https://www.bioinformatics.babraham.ac.uk/projects/trim_galore/
Trimmomatic v0.38	Bolger et al.[67]	http://www.usadellab.org/cms/?page=trimmomatic
Bowtie2 v2.4.2	Langmead and Salzberg[68]	http://bowtie-bio.sourceforge.net/bowtie2/index.shtml
HISAT2 v2.1.0	Kim et al.[69]	https://ccb.jhu.edu/software/hisat2/index.shtml
BWA v0.7.17	Li and Durbin[70]	https://bio-bwa.sourceforge.net/
samtools v1.9	Danecek et al.[71]	http://samtools.sourceforge.net/
macs2 v2.2.7.1	Zhang et al.[72]	https://github.com/macs3-project/MACS/wiki/Install-macs2
bedtools v2.26.0	Quinlan and Hall[73]	https://bedtools.readthedocs.io/en/latest/
Deeptools v3.5.0	Ramirez et al.[74]	https://deeptools.readthedocs.io/en/develop/index.html
Homer v4.11	Heinz et al.[75]	http://homer.ucsd.edu/homer/
featureCounts v2.0.1	Liao et al.[76]	https://subread.sourceforge.net/
picard toolkit v2.26.0	http://broadinstitute.github.io/picard/	http://broadinstitute.github.io/picard/
GATK v4.2.6.1	DePristo et al.[77]	https://gatk.broadinstitute.org/hc/en-us
cnvkit v0.9.9	Talevich et al.[78]	https://cnvkit.readthedocs.io/en/stable/
breakdancer v1.4.5	Chen et al.[79]	https://breakdancer.sourceforge.net/
Annovar (2020-06-07)	Wang et al.[80]	https://annovar.openbioinformatics.org/en/latest/
IGV v2.8.10	Robinson et al.[81]	http://software.broadinstitute.org/software/igv/
R v4.2.3	https://www.r-project.org	https://www.r-project.org/

EXPERIMENTAL MODEL AND STUDY PARTICIPANT DETAILS

Mice

All experiments involving animals were reviewed and approved by the Ethical Committee and Animal Welfare Committee of Nanjing Drum Tower Hospital, the Affiliated Hospital of Nanjing University Medical School. For the xenograft model, male BALB/c nude mice (4-6 weeks old) were purchased from GemPharmatech (Jiangsu, China) and maintained in an SPF environment. A total of 1×10^6 or 2×10^6 A375 cells from various treatment groups were suspended in 100 μL of Matrigel into the flanks. The mice were observed for a period of approximately three weeks. After 3 weeks of treatment the mice were euthanized. Tissues were collected and weighed.

Cell culture

The A375 (female), HuCCT1 (male), IMR90 (female), and HEK293T cell lines used in this study were maintained in DMEM medium (Gibco, 16600) supplemented with 10% FBS (Gibco), 1% penicillin-streptomycin (Gibco, 15140), and 1% glutamine (Meilunbio, MA0155) and cultured at 37°C in 5% CO_2.

To construct the *METTL3*- and *CENPA*-knockdown and control cell lines, we used the TRC Lentiviral Human shRNA system encoding a control shRNA or shRNAs targeting *METTL3* (5'-CCGGGCCAAGGAACAATCCATTGTTCTCGAGAACAATGGATTGTTCCT TGGCTTTTTG-3', 5'-CCGGGCTGCACTTCAGACGAATTATCTCGAGATAATTCGTCTGAAGTGCAGC TTTTTG-3'), targeting *CENPA* (5'- CCGGCCTCTGTAACAGAGGTAATATCTCGAGATAT TACCTCTGTTACAGAGGTTTTTG-3', 5'- CCGGGCAGCAGAAGCATTTCTAGTTCTCGA GAACTAGAAATGCTTCTGCTGCTTTTTG-3'). Lentiviruses were generated by transfecting HEK293T cells with shRNA constructs, psPAX2 and pMD2.G. The viral supernatants were harvested 48 h post-transfection by centrifugation at 4000 *g* and 4°C for 20 min, then filtered and added to the target cancer cells for 6-8 h. A375 cell lines were transfected with a doxycycline (dox)-inducible Tet-On system encoding wild-type METTL3 or catalytically inactive METTL3 (APPW). Similarly, the $CENPA^{WT}$- and $CENPA^{Mut}$-overexpressing cell lines were generated using the Dox-induced Tet-on system. For the dCas13b-FTO-mCherry stable cell line, the lentivirus was generated by transfecting HEK293T cells with pLenti-dCas13b-FTOmCherry, a packaging plasmid (delta 8.9), and an envelope plasmid (VSV-G).

METHOD DETAILS

RNA isolation

Cells were harvested and total RNA was extracted using TRIzol™ reagent (Invitrogen) following the manufacturer's protocol. To isolate mRNA and non-ribosomal (non-Rib) RNA from total RNA, the Dynabeads® mRNA Purification Kit (Invitrogen) and rRNA Depletion Kit were used separately according to the manufacturer's instructions. The RNA concentration was determined using a NanoDrop™ (Invitrogen) by measuring the UV absorbance at 260 nm.

RT-qPCR

The relative abundance of RNA was assessed by reverse transcription (RT)-qPCR. Total RNA or chromatin-associated RNA (caRNA) was reverse-transcribed using HiScript® III RT SuperMix (Vazyme) to obtain cDNA. GAPDH, Histone H3, or the m^6A spike-in from the EpiMark® N^6-Methyladenosine Enrichment Kit (NEB #E1610S) was used as an internal control. RT-qPCR was conducted on a LightCycler® 480 II system (Roche) using ChamQ Universal SYBR® qPCR Master Mix (Vazyme). The primers used for RT-qPCR are listed in Table S1. Relative changes in expression were calculated using the ΔΔCt method.

CRISPR-dCas13b plasmid transfection

CRISPR-dCas13b-FTO plasmid was a gift from Dr. Chuan He, A375 and HUCCT1 cells were transfected with dCas13b-*wt*FTO or dCas13b-*mu*FTO (catalytic-inactive mutant, H231A and D233A) constructs to generate pertinent stable cell lines. The dCas13b-FTO-gRNA plasmids were generated according to previously published procedures.[36] In brief, the specific gRNA for cenRNA was designed to target within the 200 base pair window flanking the m^6A site and verified by BLAT (BLAST-like Alignment Tool)[81] to have no off-target matches in the genome. The length of the gRNA primers typically spans approximately 25 nucleotides, with an additional carrier homologous arm of 15-20 nucleotides appended to the primer flanks. Reverse primers were also designed accordingly. The forward and reverse primers annealed in a 1:1 ratio through gradient cooling from 94 °C to 4 °C at a rate of 1 °C per minute. The gRNA plasmids were constructed using the homologous recombination method and were introduced into the stable expression dCas13b-*wt*FTO or dCas13b-*mu*FTO cell lines to target specific cenRNA. The primers used for constructing dCas13b-gRNA plasmids and the specific cenRNA regions targeted by sgRNAs were listed in Table S1.

m^6A-IP and RT-qPCR

We performed m^6A-IP enrichment followed by RT-qPCR to quantitate the changes in m^6A methylation of a specific target gene. 1 μL aliquot of 1:100 diluted m^6A and 1 μL non-m^6A spike-in from the EpiMark® N^6-Methyladenosine Enrichment Kit (NEB #E1610S) were added to 1 μg non-Rib caRNA extracted from cells. m^6A-IP was performed using the EpiMark® N^6-Methyladenosine Enrichment Kit according to the manufacturer's protocol. The purified RNA samples were used as the template for RT-qPCR.

SELECT

The specific m^{6}A sites on cenRNA were identified using single-base elongation- and ligation-based qPCR amplification (SELECT) procedure.[38] Briefly, 1.5 μg non-Rib caRNA was mixed with 100 nM Up Primer, 100 nM Down Primer, and 5 μM dNTP in 17 μL 1× CutSmart buffer (NEB). The RNA and primers were annealed under a temperature gradient process: 90°C for 1 min, 80°C for 1 min, 70°C for 1 min, 60°C for 1 min, 50°C for 1 min, 40°C for 6 min, 30°C for 1 min, 20°C for 1 min, 10°C for 1 min, and finally a hold at 4°C. Next, 3 μL of a mixture containing 0.01 U Bst DNA polymerase, 0.5 U SplintR ligase, and 10 nmol ATP was added to the solution, bringing the final volume to 20 μL. The reaction mixture was incubated at 40°C for 20 min, denatured at 80°C for 20 min, and kept at 4°C. Subsequently, RT-qPCR was conducted on a LightCycler® 480 II system (Roche) using ChamQ Universal SYBR® qPCR Master Mix (Vazyme).

Immunofluorescence and confocal microscopy

Cells were seeded onto slides, fixed with 4% paraformaldehyde for 15 min, washed three times with 1× PBS, and treated with 0.5% Triton X-100 for a further 15 min. Samples were blocked for 30 min with 5% BSA containing 0.1% Tween-20, after which primary antibodies were added and incubated overnight at 4°C. The following day, a secondary antibody was added and incubated at room temperature for 2 h, after which the slides were stained with DAPI and sealed. Mitotic abnormalities under various categories[82,83] were observed, including: 1) micronuclei, where incorrectly separated chromosomes were wrapped in abnormal nuclear structures; 2) misaligned chromosomes, where chromosomes failed to align at the metaphase plate; 3) lagging, where the chromosomes lagged behind the segregating masses of DNA in late mitosis; and 4) the abnormal multipolar spindles, where more than two spindle poles were observed. We summarized all these phenotypes as mitotic defects and quantified the percentages of different mitotic abnormalities across various treatment groups. Immunofluorescence images were taken using a Leica fluorescence microscope and analyzed using ImageJ. Specifically, to quantify the intensity of targeted proteins, we first extracted a single channel of the image and applied the Freehand selections tool to manually select the cells using ImageJ. For proteins expressed throughout the entire nucleus, we measured the Mean Gray Values of the entire cell nucleus of the samples. For proteins expressed in foci within the cells, we adjusted the threshold and select the appropriate foci regions to capture as much signal as possible but not the background, and the signals were further measured based on the Mean Gray Value of the foci in samples. For all image analysis, we selected a rectangle area without any positive signal to quantify the average background noise, and further subtracted it from the average fluorescence intensity as the final value. The "n" shown in the figures and figure legends represents the total number of cells randomly selected and used for quantifications.

Metaphase spread and FISH

Cells were treated with 0.1 μg/mL colchicine for 3 h, transferred to a 15 mL tube, and centrifuged at 1000 rpm. The supernatant was carefully removed and the cells were resuspended in 2 mL 75 mM KCl. A fixative solution, freshly prepared by mixing methanol and acetic acid at a 3:1 ratio, was added at an equal volume of 2 mL to the cell suspension, which was then kept at -20°C overnight. The next day, samples were centrifuged, resuspended in 200 μL fixative solution, and dropped from a height onto microscope slides, after which the slides were air-dried or baked in an oven at 70°C for 3 h. The prepared slides were fixed with 4% formaldehyde for 4 min at 37°C and then treated with RNaseA+H solution for 1 h at 37°C. After further treatment with 0.005% pepsin for 4 min at 37°C, the slides were fixed again, dehydrated successively in 70%, 80%, and 100% ethanol for 1 min each, and air-dried. The PNA CENPB probe was dissolved in hybridization buffer (20 mM Na_2HPO_4, 20 mM Tris, 60% formamide, 0.1 μg/mL salmon sperm DNA, 2× SSC), denatured for 10 min at 85°C, and hybridized for 2 h at room temperature. The slides were washed twice with 2× SSC/0.1% Tween-20 solution at 55-60°C and subsequently washed once with 2× SSC and once with 1× SSC at room temperature. Samples were stained with DAPI and the intensity was measured using a confocal laser scanning microscope and analyzed using ImageJ.

Co-FISH

Samples were subjected to the immunofluorescence staining process. After incubation with secondary antibodies, samples were washed three times with PBS, incubated successively with ice-cold 70%, 80%, and absolute ethanol for 1 min each, and subject to air-dry. The probe was preheated at 85°C for 5 min and added to the samples, which were incubated at 85°C for 10 min and then at room temperature for a further 2 h. The samples were washed twice with 2× SSC/0.1% Tween-20 solution at 55-60°C, and then once with 2× SSC and once with 1× SSC at room temperature. Subsequently, slides were stained with DAPI, imaged using a Leica fluorescence microscope, and analyzed using ImageJ.

Genomic and centromere DNA extraction

Genomic DNA was extracted using the TIANamp Genomic DNA Kit (DP304, TIANGEN) following the manufacturer's instructions. Centromere DNA was isolated according to a previously published procedure.[50] In brief, 200 μg genomic DNA was digested with *Bsm*I (NEB, R0134L) for 2-3 h at 65°C, and Ampure XP beads were used to enrich DNA fragments less than 250 bp in size to obtain centromeric DNA.

LC-MS/MS quantitation of dU in DNA

The dU level was detected according to a previously published procedure.[50] Briefly, 25 μg centromeric DNA was treated with 10 U UDG (NEB) at 37°C for 2 h, mixed with a 3× volume of pre-cooled acetonitrile, and centrifuged at 16,000 *g* for 20 min at 4°C. The supernatant was transferred to a fresh tube, dried using a rotary dryer, dissolved in 20 μL deionized water, and injected into the LC-MS/MS. Nucleosides were separated by reverse ultra-performance liquid chromatography on a C18 column and detected by a triple-quadrupole mass spectrometer (AB SCIEX QTRAP 6500) in positive ion multiple reaction-monitoring mode (MRM), with a mass transition monitoring of 111.0→42.0 for uracil. To quantitate the dT content, the same centromeric DNA (500 ng) was digested with 2.5 U DNA Degradase Plus (Zymo research) in a total volume of 15 μL at 37°C for 2 h. Then, 48.5 μL ddH2O was added and the solution was centrifuged at 14,800 rpm for 20 min at 4°C. Next, 5 μL supernatant was analyzed by LC-MS/MS using the same procedure described above, except that the positive electrospray ionization mode was used and the mass transition of 243.0→127.0 for dT was monitored.

Cell fractionation

Cells were fractionated according to a previously published procedure.[36,84] In brief, 5 × 10^6-1 × 10^7 cells were collected and washed with 1 mL cold 1× PBS/1 mM EDTA buffer. The cell pellet was collected by centrifugation at 500 *g*, room temperature (RT), resuspended in 200 μL ice-cold lysis buffer (10 mM Tris-HCl, pH = 7.5, 0.05% NP40, 150 mM NaCl), flicked and incubated on ice for 5 min. The cell lysate was then gently pipetted over equal volumes of chilled sucrose cushion (24% RNase-free sucrose in lysis buffer) and centrifuged at 15,000 *g* for 10 min at 4°C. The supernatant was collected as the cytoplasmic fraction. The nuclei pellet was then carefully overlaid with 200 μL ice-cold 1× PBS/1 mM EDTA, which was subsequently aspirated without disturbing the pellet. The nuclear pellet was then resuspended in 100 μL prechilled glycerol buffer (20 mM Tris-HCl, pH = 7.9, 75 mM NaCl, 0.5 mM EDTA, 0.85 mM DTT, 0.125 mM PMSF, 50% glycerol) with gentle flicking of the tube. A double volume of cold nuclei lysis buffer (10 mM HEPES, pH = 7.6, 1 mM DTT, 7.5 mM $MgCl_2$, 0.2 mM EDTA, 0.3 M NaCl, 3 M UREA, 1% NP-40) was added, and the mixture was vortexed vigorously 4 times for 5 s each. The nuclear pellet mixtures were incubated on ice for 2 min and then centrifuged at 15,000 *g* for a further 2 min at 4°C. The supernatant was collected as the nucleoplasm fraction. The pellet was gently rinsed with cold 1× PBS/1 mM EDTA without dislodging and then collected as the chromosome-associated fraction.

LC-MS/MS quantitation of the RNA modification

A total of 20 ng non-Rib RNA or mRNA was digested with 1 U nuclease P1 (Wako) in 17 μL buffer containing 10 mM NH_4Ac (pH = 5.3) at 42°C for 2 h. Next, 1 U rSAP enzyme (NEB) and 2 μL 10× rCutsmart™ buffer (NEB) were added and incubated at 37°C for 6 h or overnight. The digested sample was centrifuged at 13,000 rpm for 10 min at RT, after which 5 μL supernatant was injected into the LC-MS/MS. Nucleosides were separated by reverse ultra-performance liquid chromatography on a C18 column and detected by a triple-quadrupole mass spectrometer (AB SCIEX QTRAP 6500) in positive ion multiple reaction-monitoring mode (MRM). Nucleosides were quantitated by retention time and nucleoside-to-base ion mass transitions (268-136 for A; 282-150 for m^6A, $N^{6,6}mA$ and m^1A; 245-to-179 for Ψ; 256-to-150 for m^5C). Quantitation was performed by comparison with standard curves obtained from pure nucleoside standards in the same batch of samples. The m^6A, $N^{6,6}mA$, m^1A, Ψ, m^5C level was calculated as the ratio of modification/A according to the calibration concentration.

Cell cycle analysis

5-Ethynyl-2'-deoxyuridine (EdU) was utilized to investigate S-phase progression, while a phospho-histone H3 (pH3) antibody was utilized to mark mitotic cells. S-phase analysis entailed EdU incorporation, followed by staining with the BeyoClick™ EdU kit according to the manufacturer's instructions. For the assessment of mitotic cells, the cells were harvested and fixed with 4% paraformaldehyde for 15 min, washed three times with 1× PBS, and permeability's with 0.5% Triton X-100 for 15 min. Samples were incubated with 5% BSA containing 0.1% Tween for 30 min to avoid unspecific signals, followed by overnight incubation of pH3 antibody at 4 °C. The next day, a fluorescent secondary antibody was added, and incubation continued at room temperature for 2 h. Finally, DAPI staining was performed. Subsequent analyses of S-phase and mitotic cells involved flow cytometry using a CytoFLEX instrument (Beckman), with data interpretation facilitated by FlowJo_V10 software.

Western blot analysis

Cells were collected and lysed in RIPA buffer (Solarbio, R0010) containing 1% PMSF (Solarbio, P0100) on ice for 30 min. The protein concentration was measured using a BCA kit (Thermo, 23227) following the manufacturer's protocol. The lysates were mixed with 6× loading buffer (TRANS, Q20921), boiled at 95°C for 5 min, and then stored at -80°C for later use. For electrophoresis, a total of 10 μg protein from each sample was loaded into a 12% SDS-page gel and electrotransferred onto a PVDF membrane (Millipore, IPVH00010). The membranes were blocked in PBST with 5% milk at room temperature (RT) for 30 min, followed by an overnight incubation at 4 °C with a diluted primary antibody solution. After washing, the membranes were incubated with a HRP-conjugated secondary antibody at RT for 1 h. The ECL solution (MA0186) was then added and allowed to react at room temperature for 1-2 min. Protein bands were visualized using a CCD camera (Tanon).

caRNA m^{6}A-seq

Total caRNA was isolated from A375 cells, and 1 μL 1:1000-diluted m^{6}A and non-m^{6}A spike-in from the EpiMark® *N*^{6}-Methyladenosine Enrichment Kit (NEB #E1610S) was added to 1 μg purified non-Rib caRNA, which was then subjected to fragmentation according to previously published protocols.[36] m^{6}A-IP was performed using the EpiMark *N*^{6}-Methyladenosine Enrichment Kit according to the manufacturer's protocol. RNA library construction was carried out using the SMARTer® Stranded Total RNA-Seq Kit v2 (Takara) according to the manufacturer's protocol. Sequencing was performed at Annoroad (China) on an Illumina NovaSeq instrument in paired-end mode with 150-base paired (bp) reads.

CaRNA m^{6}A-seq data analysis

Quality control was performed using FastQC (v0.11.9) (https://www.bioinformatics.babraham.ac.uk/projects/fastqc/). Low-quality bases and adapters were trimmed using Trim Galore (v0.6.6),[66] and ribosomal RNAs were removed by Bowtie2 (v2.4.2).[68] The remaining reads were aligned to the human genome (hg38) along with spike-in genomes, including two control RNAs (one with m^{6}A modification and one without) (NEB #E1610S), using HISAT2 (v2.1.0)[69] with '–rna-strandness RF' parameters. Strand-specific reads were separated using samtools view (v1.9)[71] with flags 99, 147, 83, and 163. m^{6}A peak calling was performed using macs2 (v2.2.7.1)[72] with '–keep-dup 5' parameters. m^{6}A peaks that overlapped in two biological replicates were used for downstream analysis using 'bedtools intersect -f 0.5 -F 0.5 -e -s' (v2.26.0)[73] parameters. The consensus motifs were analyzed using Homer (v4.11).[75] Mapped reads were converted to bigwig format for Integrative Genomics Viewer (IGV)[81] generated by deeptools (v3.5.0)[74] bamCoverage with the parameters '–normalizeUsing RPKM'. The total m^{6}A level for each sample was calculated by dividing the number of reads aligned to the human genome by the number of reads aligned to the m^{6}A-modified spike-in. The m^{6}A level for each replicate was defined as the ratio of the IP sample to the input sample. The m^{6}A-normalized factors of enrichment were quantified with the m^{6}A level values divided by the average m^{6}A level value of control samples.

FeatureCounts (v2.0.1)[76] was utilized to quantitate read counts on m^{6}A peaks and caRNAs, and only those with more than 10 reads in two input samples were retained for downstream analysis. The m^{6}A level for each caRNA and peak was calculated as $(CPM_{IP} + 0.01)/(CPM_{Input} + 0.01)$. The m^{6}A-normalized factors were then multiplied by $(CPM_{IP} + 0.01)/(CPM_{Input} + 0.01)$. The m^{6}A-methylated caRNAs (including cenRNA) were defined as those with an m^{6}A level greater than at least 1.5-fold ($\log_2$[IP/Input] > 0.58) in cells. For caRNA m^{6}A-seq data in A375 cells following *METTL3* knockdown, the differentially m^{6}A-methylated RNAs were identified by the changes (sh*METTL3*/shControl) of normalized m^{6}A level with an m^{6}A-normalized factor > 1.5-fold ($|\log_2$(Fold Change)| > 0.58). We categorized different RNA species into METTL3-sensitive (methylation decreased following knockdown), METTL3-insensitive (methylated in either wild-type or *METTL3*-knockdown A375 cells without hypomethylation following knockdown), and non-methylated (not methylated in either wild-type or *METTL3*-knockdown A375 cells) according to their methylation level in wild-type or *METTL3*-knockdown cells and their changes following *METTL3* knockdown based on MeRIP-seq data.

Definition of carRNAs and lncRNAs

We identified chromatin-associated regulatory RNAs (carRNAs), including repeat RNAs, enhancer RNAs (eRNAs), and promoter-associated RNAs (paRNAs), based on previous work.[36] Annotation of repeat RNAs for the hg38 human genome assemblies was downloaded from the UCSC Table Browser (https://genome.ucsc.edu/cgi-bin/hgTables). H3K27ac peaks were analyzed using H3K27ac ChIP-seq in A375 cells (GSE82332)[65] by Homer (v4.11)[75] with 'findPeaks -style factor -size 1000' parameters. H3K27ac peaks for the MCF7, HEK293T, IMR90, K562, and HepG2 cell lines were downloaded from the ENCODE portal (https://www.encodeproject.org/), while H3K27ac peaks for the HEC-1-A cell line were obtained from the GSE140557 datasets.[36] Annotation of mRNAs and long non-coding RNAs (lncRNAs) was obtained from GENCODE (https://www.gencodegenes.org/).

m^{6}A levels of distinct RNA species

For comprehensive analysis on m^{6}A levels of various RNA species in cancer and normal cell lines, five public non-Rib caRNA m^{6}A-seq datasets for MCF7 (GSE196564), IMR90 (GSE159550), HepG2 (GSE205709), K562 (GSE205709), and HEC-1-A (GSE140557) cell lines,[34–37] along with two in-house generated non-Rib caRNA m^{6}A-seq datasets for A375, and HEK293T cell lines were applied.

To compare the m^{6}A levels between mRNAs and ncRNAs in five cancer and two normal cell lines, 'bedtools intersect' (v2.26.0)[73] was used to assign the m^{6}A peaks (i.e. peak.bed) to the mRNAs (i.e. mRNA.bed) with the parameters '-a peak.bed -b mRNA.bed -f 0.5 -s -wao -u', while the remaining peaks were assigned to the ncRNAs. The methylation level of the mRNAs (or ncRNAs) was defined as the CPM value for IP reads within the peaks assigned to the mRNAs (or ncRNAs) divided by the input reads. To profile the differences in m^{6}A levels of ncRNAs, including carRNAs and lncRNAs, featureCounts (v2.0.1)[76] was utilized to quantify read counts on these RNAs. The m^{6}A level for each carRNA and lncRNA was calculated as $(CPM_{IP} + 0.01)/(CPM_{Input} + 0.01)$. The m^{6}A-methylated carRNAs and lncRNAs were defined as those with an m^{6}A level greater than at least 1.5-fold ($\log_2$[IP/Input] > 0.58) in wild-type samples. When comparing the methylation levels among these RNAs, the relative methylation level was all normalized to the average methylation level of repeat RNAs in normal cell lines (as 1).When comparing various repeat families, the relative methylation level was calculated as taking the average methylation level of the low complexity repeats in normal cell lines as 1 for normalization. The proportion of methylated repeats RNA in each repeat family was defined as methylated repeat RNAs/(methylated repeat RNAs + non-methylated repeat RNAs). The average methylation proportion of each repeat family in five cancer cell lines was taken as the methylation proportion of the repeat family.

ChIRP probes design for cenRNA

To ensure comprehensive enrichment of cenRNAs in the chromatin isolation by RNA purification (ChIRP) assay, we designed RNA probes targeting the transcriptionally active cenRNA species. Specifically, based on the RNA-seq reads aligned to the transcriptome, we first calculated the number of mapped reads of the cenRNAs, and each nucleotide base with more than 5 reads was retained. The neighboring bases passing the filter were merged to define the transcribed cenRNA regions. Within these regions, the actively transcribed cenRNA species were then selected based on the total read count (> 60) and the sequencing coverage (> 0.2). We further performed multiple sequence alignments of these cenRNA species. Considering the repetitive feature of cenRNAs, we designed 32 probes targeting the consensus sequences of the active cenRNA regions, and some other probes targeting the sub-consensus regions. In total, we have collected 46 probes (20-30 nt) along the multiple alignments of the actively transcribed cenRNAs. All the probes designed for ChIRP assays have been summarized in Table S2.

ChIRP-seq

Harvest the 10^7 cells by trypsin digestion, and wash once with 5-10 ml ice-cold PBS. Resuspend the pellet with 5 ml 2 mM DSP crosslinking solution and the suspension was rotated end-to-end at room temperature for 30 minutes. Approximately 0.45 ml of 37% formaldehyde (FMA) was added per 5 ml of DSP crosslinking samples to achieve a final concentration of 3% FMA. The mixture was then rotated end-to-end at room temperature for 15 minutes. To halt the crosslinking process, 1/10 volume of 2.5 M glycine was added, followed by 5 minutes of end-to-end rotation. The pellet was washed twice with 10 ml of 1×PBS on ice.The cells were then snap-frozen in liquid nitrogen and stored at -80°C. For each sample, the pellet was resuspended in 300 μL nuclei lysis buffer (50 mM Tris-HCl, pH 7.5, 10 mM EDTA, 1% SDS) containing 1.5 μL protease inhibitor and 1.5 μL PMSF. After centrifugation at 13,000 rpm for 30 s, the supernatant was removed, and the pellet was resuspended in 200 μL nuclei lysis buffer. Next, the chromatin was sheared by 25 cycles (30 s on/60 s off) of a Bioruptor (Diagenode), and then a 1/30 volume (10 μL) of each sample was added to 90 μL DNA reverse crosslinking buffer (20 mM Tris-Cl, 150 mM NaCl, 10 mM EDTA, 0.5% SDS) containing 2 μL protease K. The samples were incubated overnight at 56°C, and DNA was extracted as the input DNA. The remaining sample was mixed with a 1/4 volume of 5× rRIP Hybridization buffer (50 mM Tris-HCl, pH 7.5, 10 mM EDTA, 1% SDS, 1.5 M NaCl, 50% formamide), biotinylated probes (5-30 pmol) were added to each sample, and the mixture was subjected to end-to-end rotation at 39°C for 2-4 h. Subsequently, 20-80 μL well-washed streptavidin C1 beads were added to each sample (20 μL beads for samples with 5 pmol probes; 40 μL beads for samples with 20 pmol probes), and the samples were mixed by end-to-end rotation at 39°C for 3 h. Following the pulldown, the beads were washed four times with 0.1× SSC wash buffer (0.1× SSC, 1% SDS) at 39°C for 15-30 min each. After the final wash, 100 μL freshly prepared 1× RNase H wash buffer (50 mM Tris-HCl, 75 mM NaCl, 5 mM $MgCl_2$, 0.1% Triton™ X-100) was added, and the mixture was shaken at 37°C for 5 min. The samples were then transferred to a magnetic stand to remove the supernatant. For RNA elution: 0.1× SSC wash buffer was removed on a magnetic stand, and 50 μL 1× nuclei lysis buffer was added. The mixture was then subjected to 95°C heat for 2 min and immediately transferred onto a magnetic strand to enable the transfer of the RNA elution to a fresh tube. Subsequently, 0.5 μL 1M DTT was added, and the solution was boiled at 95°C for 10 min, briefly centrifuged, and then boiled again at 95°C for a further 10 min. Finally, 500 μL TRIzol™ reagent was added, and the sample was stored at -80°C. For protein elution: 30 μL 6× SDS protein loading buffer was added to the beads, and the solution was boiled for 10 min at 98°C. DNA was eluted with twice the bead volume of RNase H elution solution (NEB, M0297S) containing 0.2 U/μL RNase H, with shaking at 37°C for 30 min. The elution tube was placed on a magnetic stand, and the eluate was transferred to a fresh tube. The beads were resuspended in twice the bead volume of RNase H wash buffer containing 1% SDS at RT and briefly vortexed for 5 s. The supernatant was transferred and combined with the eluate mentioned above, to which 5 M NaCl and 0.5 M EDTA were added to a final concentration of 100 mM NaCl and 10 mM EDTA, along with 1 μL 20 mg/mL protease K. Reverse crosslinking was conducted at 56°C overnight. DNA was purified using a PCR product purification kit (ZymoDNA Clean & Concentrator-500) following the manufacturer's instructions. Purified DNA samples were prepared for sequencing using the VAHTS Universal Pro DNA Library Prep Kit for Illumina.

ChIRP-seq data analysis

Paired-end read quality control was performed by FastQC (v0.11.9) (https://www.bioinformatics.babraham.ac.uk/projects/fastqc/). Low-quality bases and adapters were trimmed using Trim Galore (v0.6.6),[66] and trimmed reads were aligned to the human genome (hg38) using Bowtie2 (v2.4.2).[68] PCR duplicates were removed using picard (v2.26.0) (http://broadinstitute.github.io/picard/) MarkDuplicates. Peak calling was performed by macs2 (v2.2.7.1),[72] and the distribution of peaks in genomic regions was analyzed using Homer (v4.11).[75] Mapped reads were converted into bigwig format using deeptools (v3.5.0)[74] bamCompare with parameters '–operation log_2 –binSize 5 –normalizeUsing RPKM'. Profile plots over m^6A-marked cenRNAs were generated by deeptools (v3.5.0)[74] computeMatrix and plotProfile.

Whole-genome sequencing

Genomic DNA from A375 cells was extracted using a genomic DNA isolation kit (TIANGEN, DP304) and fragmented into 200-500-bp fragments for sequencing by ultrasonication (Bioruptor, Diagenode). The DNA library was constructed and sequenced at Annoroad (China) on an Illumina NovaSeq instrument in paired-end mode with 150-bp reads.

Data analysis of whole-genome sequencing

Quality control on paired-end reads was performed by FastQC (v0.11.9) (https://www.bioinformatics.babraham.ac.uk/projects/fastqc/). Low-quality bases and adapters were trimmed using Trimmomatic (v0.38)[67] and aligned to the human genome (hg38) using BWA-mem (v0.7.17).[70] Duplicates were marked using picard (v2.26.0) (http://broadinstitute.github.io/picard/) MarkDuplicates. GATK (v4.2.6.1)[77] BaseRecalibrator and ApplyBQSR were used for base recalibration. Somatic single-nucleotide polymorphisms (SNPs) were called using GATK (v4.2.6.1)[77] Mutect2. GATK (v4.2.6.1)[77] FilterMutectCalls and SelectVariants were applied to filter and obtain SNPs, respectively. Copy number variations (CNVs) and structural variations (SVs) were identified using cnvkit (v0.9.9)[78] and breakdancer (v1.4.5),[79] respectively. Variant annotations were performed using Annovar (2020-06-07)[80] annotate_variation.pl with '–regionanno' parameters. We scanned the genome using a 1,000,000-nt window to visualize SNPs on a genome-wide scale. SNP sites in each window were counted and visualized using R package circlize (v0.4.16).[85]

To evaluate centromere stability, random regions were selected using 'bedtools shuffle' (v2.26.0)[73] based on the location and length of cenRNAs. The number of variants occurring in the centromeric regions that encoded cenRNA or in random regions after either *METTL3* knockdown or dCas13b-FTO treatment were counted for each variant type, including CNVs, SNPs, and SVs (inversions [INV] and deletions [DEL]); and for each chromosome, centromere stability was calculated as $\log_2(cenRNA_{mean}/Random_{mean})$. $cenRNA_{mean}$ represents the average number of variants that occurred in all centromeric regions encoding cenRNA on each chromosome. A $\log_2(cenRNA_{mean}/Random_{mean}) > 0$ indicates increased centromere instability on that chromosome.

Chromatin-bound protein MS analysis

Cells were treated according to a previously published procedure.[44] In brief, 1×10^7 cells were harvested and lysed in 200 μL ice-cold NP-40 lysis buffer (10 mM Tris-HCl, pH = 7.5, 0.05% NP40, 150 mM NaCl) to disrupt the cytoplasmic membrane by incubation on ice for 5 min. Subsequently, the lysate was resuspended, gently pipetted over a layer of chilled sucrose cushion (24% RNAse-free sucrose in lysis buffer), and centrifuged at 15000 *g* for 10 min at 4°C. The pelleted nuclei were then crosslinked with 1% formaldehyde for 10 min, and the reaction was stopped by incubation with a 1/20 volume of 2.5 M glycine for 5 min. The crosslinked nuclei were resuspended in twice the pellet volume of nuclei lysis buffer (50 mM Tris-HCl, 10 mM EDTA, 1% SDS, pH 8.1) and incubated on ice for 10 min. Next, a 0.5 volume of ethanol was added to the lysate, and the DNA-protein complexes were precipitated at -20°C for 1 h and then centrifuged at 5,000 *g* at 4°C for 20 min. Next, the pellet was washed with ice-cold 75% ethanol and resuspended in 50 mM Tris-HCl buffer, to which 8 M urea and 2% SDS were added and the mixture was incubated at 37°C for 30 min with gentle shaking. An equal volume of 5 M NaCl was added, and the mixture was incubated at 37°C for a further 30 min, after which a 0.1 volume of 3 M sodium acetate and 3 volumes of ice-cold ethanol were added to reprecipitate the DNA and its associated proteins. The precipitated DNA and DNA-protein complexes were collected by centrifugation at 5,000 *g* for 5 min at 4°C and then washed twice with ice-cold 75% ethanol to eliminate salts and detergents. The pellet was air-dried and resuspended in DNase digestion buffer (100 μL/10 cm dish) containing DNase I (10 U, Takara) and incubated at 37°C for 1 h. EDTA (final concentration of 10 mM) was added to stop the reaction, and the pellet was centrifuged at 13,000 rpm for 20 min at 4°C. The supernatant was collected and subjected to SDS-PAGE and subsequent MS analysis. The chromatin-associated proteins were collected based on subcellular location data from UniProt database (https://www.uniprot.org/), and were functionally annotated as histone chaperones,[45] proteins related to centromere complex assembly (GO: 0034508) or chromosome segregation (GO: 0007059) for differential protein analysis.

SNAP labeling

Cells were treated according to a previously published procedure.[10] To detect the deposition of CENPA or H3.3 at G1 phase: cells were synchronized at G1/S phase by treatment with 2.5 mM thymidine, after which pre-existing CENPA and H3.3 were blocked by treatment with 10 μM SNAP-cell block (New England Biolabs) at 37°C for 30 min. Cells were then washed three times with PBS and incubated at 37°C for 30 min. After a further three PBS washes, cells were labeled with 2 μM SNAP-TMR-Star for 15 min, washed three times with PBS, and then incubated with 2 μM SNAP-TMR-Star for a further 30 min. The slides were fixed in 4% paraformaldehyde for 15 min at RT, treated with 0.2% Triton™ X-100 for a further 15 min, and subjected to immunofluorescence assays.

To detect the maintenance of old CENPA during S phase: cells were synchronized at G1/S phase by thymidine treatment and then labeled with 2 μM SNAP-TMR-Star for 30 min as described above. Samples were washed three times with PBS and subjected to either pulse-chase labeling or immunofluorescence staining. Slides were fixed in 4% paraformaldehyde for 15 min at RT, treated with 0.2% Triton™ X-100 for a further 15 min, and then analyzed.

Chromatin fiber assay

The chromatin fiber assay was performed following a previously described procedure.[86] In brief, cells were resuspended in 75 mM KCl buffer for 10 min at 37°C and centrifuged for 8 min at 300 *g*. Subsequently, slides were incubated in lysis buffer (2.5 mM Tris HCl, pH 7.5, 0.5 M NaCl, 1% Triton™ X-100, 0.4 M urea) for 15 min at 37°C and subjected to immunofluorescence assays.

ChIP-qPCR and ChIP-seq

Cells were crosslinked with 1% formaldehyde for 15 min at RT, and 0.125 M glycine was added to stop the reaction. Cells were snap-frozen in liquid nitrogen and stored at -80°C. Next, 5×10^6 cells were resuspended in 1 mL ice-cold lysis buffer (50 mM HEPES, pH 7.9, 5 mM $MgCl_2$, 0.2% Triton™ X-100, 20% glycerol, 300 mM NaCl, proteinase inhibitor) and incubated on ice for 10 min. Cells were

pelleted by centrifugation at 500 *g* for 5 min at 4°C, resuspended in 900 μL SDS lysis buffer (50 mM HEPES, pH 7.4, 150 mM NaCl, 1 mM EDTA, 1% Triton™ X-100, 0.1% sodium deoxycholate, 0.1% SDS, proteinase inhibitor), and incubated on ice for 30 min. The chromatin was sheared with 25 cycles (30 s on/60 s off) of a Bioruptor (Diagenode). Protein A beads were washed twice with 60 μL SDS lysis buffer, and half of the beads were saved for preclearance. The remaining beads were resuspended in 200 μL SDS lysis buffer, to which 7.5 μg antibody was added, and the samples were rotated at 4°C for at least 2 h. The cell lysate was centrifuged at 15,000 rpm for 10 min at 4°C and then cleared using 30 μL protein A beads for 1 h at 4°C. The flowthrough was saved, and the precleared lysate was mixed with antibody-coated beads and rotated at 4°C overnight. The next day, the flowthrough was saved, and the beads were washed twice with 1 mL SDS lysis buffer, twice with 1 mL high-salt wash buffer (50 mM HEPES, pH 7.5, 350 mM NaCl, 1 mM EDTA, 1% Triton™ X-100, 0.1% sodium deoxycholate, 0.1% SDS), twice with 1 mL LiCl buffer (10 mM Tris-HCl, pH 8.0, 250 mM NaCl, 1 mM EDTA, 0.5% NP-40, 0.5% sodium deoxycholate), and once with TE buffer (10 mM Tris-HCl, pH 8.0, 1 mM EDTA, 0.2% Triton™ X-100). During each wash, the sample was rotated for 5 min at 4°C. The beads were then resuspended in 240 μL elution buffer (100 mM $NaHCO_3$, 1% SDS) and shaken at 30°C for 1 h. The supernatant was collected, 14.4 μL 5 M NaCl was added, and the sample was shaken at 65°C for 4 h. After the addition of 4 μL RNase A, the sample was shaken at 37°C for 15 min. Next, 4 μL proteinase K was added, and the sample was shaken at 65°C for a further 2 h. DNA was then purified by DCC with 5× binding buffer. Purified DNA samples were used as templates for ChIP-qPCR analysis or prepared for sequencing using the VAHTS Universal Pro DNA Library Prep Kit for Illumina.

ChIP-seq data analysis

Paired-end read quality control was performed by FastQC (v0.11.9) (https://www.bioinformatics.babraham.ac.uk/projects/fastqc/). Low-quality bases and adapters were trimmed using Trim Galore (v0.6.6)[66] and aligned to the human genome (hg38) and *Drosophila melanogaster* (dm6) genome using Bowtie2 (v2.4.2).[68] PCR duplicates were removed using picard (v2.26.0) (http://broadinstitute.github.io/picard/) MarkDuplicates. Mapped reads were converted into bigwig format using deeptools (v3.5.0)[74] bamCoverage with parameters '–binSize 5 –normalizeUsing RPKM' or deeptools (v3.5.0)[74] bamCompare with parameters '–operation log_2 –binSize 5'. The average normalized read densities of CENPA and histone H3.3 over cenRNA loci were generated by deeptools (v3.5.0)[74] computeMatrix and plotProfile. The whole genome was divided into many 1,000,000-bp bins, and the average normalized read densities in each bin were calculated by deeptools (v3.5.0)[74] and visualized by R package circlize (v0.4.16).[85]

Histone H3.3 peaks were called using macs2 (v2.2.7.1)[72] and CENPA peaks were identified by scanning the whole genome using 5000-nt sliding windows. Windows with $CPM_{IP}/CPM_{Input} > 4$ and a Fisher's exact $P < 0.05$ were retained. Adjacent windows were merged using 'bedtools merge' (v2.26.0),[73] and merged windows were identified as CENPA peaks. Only peaks that overlapped in two biological replicates were used for downstream analysis with 'bedtools intersect -f 0.5 -F 0.5 -e' (v2.26.0)[73] parameters. Peak annotation was performed by the annotatePeaks.pl script from Homer (v4.11).[75] 'bedtools intersect' (v2.26.0)[73] was used to assign the ChIP peaks to the distinct RNA species. ChIP-seq signal on distinct RNA loci was quantified by deeptools (v3.5.0),[74] and the CENPA binding level was calculated as IP/Input.

RIP-qPCR and RIP-seq

Protein A/G magnetic beads were washed twice with Buffer B (50 mM HEPES, pH 7.5, 10% (V/V) glycerol, 150 mM KCl, 2 mM EDTA, 0.5% (v/v) NP40, 0.5 mM DTT, Halt protease, and phosphatase inhibitors) and resuspended in 200 μL Buffer B. Half of the beads were used for immunoprecipitation (IP) by adding the appropriate antibody and rotating at 4°C for 2 h; the other half were used for preclearance of the cell lysate by rotating at 4°C for 30 min. The supernatant was transferred to a fresh tube after magnetic separation of the beads. The antibody-coupled beads were washed three times with IP wash buffer (50 mM HEPES-KOH, pH 7.5, 300 mM KCl, 0.05% (v/v) NP40, 0.5 mM DTT, complete EDTA-free protease inhibitor cocktail) and added to the cleared cell lysate. The mixture was rotated at 4°C overnight. The supernatant was then discarded, and the beads was washed three times. Thereafter, the beads was then resuspended in 500 μL TRIzol™ reagent (Invitrogen) and the RNA was extracted. Notably, all consumables and buffers used were guaranteed to be RNA enzyme-free and were supplemented with RNA enzyme inhibitors. The primers used for RIP-qPCR assays are listed in Table S1, and the relative expression was calculated using the ΔΔCt method. For RIP-seq of non-Rib RNA from total RNA, the library was prepared using the SMARTer® Stranded Total RNA-seq Kit v2 (Takara) following the manufacturer's instructions. Sequencing was performed at Annoroad (China) on an Illumina NovaSeq instrument in paired-end 150-bp mode.

CENPA RIP-seq data analysis

Quality control was performed using FastQC (v0.11.9) (https://www.bioinformatics.babraham.ac.uk/projects/fastqc/). Low-quality bases and adapters were trimmed using Trim Galore (v0.6.6),[66] and ribosomal RNAs were removed by Bowtie2 (v2.4.2).[68] The remaining reads were aligned to the human genome (hg38) using HISAT2 (v2.1.0)[69] with '–rna-strandness RF' parameters. Strand-specific reads were separated using samtools view (v1.9)[71] with flags 99, 147, 83, and 163. Mapped reads were converted into bigwig format using deeptools (v3.5.0)[74] bamCoverage with parameters '–binSize 20'. We divided the human genome into many 1,000,000-bp bins, and the average normalized read densities in each bin were calculated by deeptools (v3.5.0) and visualized by R package circlize (v0.4.16).[85]

According to the read distribution across the genome inspected by the IGV genome browser, the search for enriched peaks in the RIP samples compared with the input controls was performed by scanning the whole genome using 5000-nt sliding windows, with slight modifications from a previous study.[87] Windows with $CPM_{IP}/CPM_{Input} > 4$ and a Fisher's exact $P < 0.05$ were retained. Adjacent

windows were merged using 'bedtools merge' (v2.26.0),[73] and merged windows were identified as CENPA RIP peaks. Peaks that overlapped in two biological replicates were used for downstream analysis using 'bedtools intersect' (v2.26.0).[73] The RIP peak on genomic regions was annotated by Homer (v4.11).[75] 'bedtools intersect' (v2.26.0)[73] was used to assign the RIP peaks to the distinct RNA species, including carRNAs and mRNAs. Read counts of carRNAs, mRNAs and peaks were quantitated by featureCounts (v2.0.1)[76] and then normalized to CPM. CENPA enrichment for each RNA and peak was calculated as (CPM_{IP} + 0.01)/(CPM_{Input} + 0.01). Consensus motifs were called using Homer (v4.11)[75] findMotifsGenome.pl with the parameter '-rna'.

CENPA^{wt}- and CENPA^{mu}- H4 bacterial expression

BL21-CodonPlus competent cells were transformed with the pET-Duet1 expression plasmid, spread onto LB/amp agar plates, and incubated overnight at 37°C. A single colony was picked and cultured in 10 mL LB/amp medium overnight at 37°C and then scaled up to a 1 L LB/amp culture. Subsequently, protein expression was induced with 1 mL 1 M IPTG and incubated in an 18°C shaker at 220 rpm overnight. Cells were harvested by centrifugation at 5,000 *g* for 10 min, and the pellets were resuspended in binding buffer (20 mM Tris-HCl, 400 mM NaCl, 200 mM imidazole, 100 mM PMSF, 100 mM DTT, β-mercaptoethanol) and sonicated (2 s on, 5 s off, 200 W power) on ice for 35 min until the solution was no longer viscous. Debris was removed by centrifugation at 18,000 rpm for 20 min, and the target protein was subsequently purified using the AKTA protein purification system with a Ni-NTA column.

RNA-protein EMSA

Purified protein was diluted into a series of concentrations in 1× binding buffer (10 mM HEPES, 50 mM KCl, 1 mM EDTA, 0.05% Triton™ X-100, 5% glycerol, 0.01 mg/mL BSA, 1 mM DTT, 40 U/mL RNase inhibitor). Next, 1 μL RNA probe (final concentration of 200 nM) and 1 μL protein (taken from the serial dilution) were mixed, and 1× binding buffer was added to a final volume of 10 μL and incubated on ice for 30 min. After incubation, 2 μL 5× TBE high-density loading buffer was mixed with each reaction and centrifuged gently. Proteins were separated by native gel electrophoresis, transferred to nylon membrane, and labeled with biotin, after which RNA-protein interactions were detected by chemiluminescence.

RNA binding protein pulldown

A 5× packed-cell volume of cold lysis buffer (10 mM NaCl, 2 mM EDTA, 0.5% Triton™ X-100, 0.5 mM DTT, 10 mM Tris-HCl, pH 7.5) was added to each cell sample along with 1× protease and phosphatase inhibitors. The mixture was incubated for 15 min on ice, centrifuged at 10,000 *g* for 15 min at 4°C, and then the supernatant was collected. Next, 100 μL streptavidin-conjugated magnetic beads were washed twice with binding buffer (150 mM KCl, 1.5 mM $MgCl_2$, 0.05% NP-40, 0.5 mM DTT, 10 mM Tris, pH 7.5) and resuspended in 100 μL binding buffer. The cell lysate was added, and the mixture was incubated for 1 h at 4°C with slow rotation. The precleared cell lysate was then divided into two tubes, and 1 U/100 μL RNase inhibitor and 2 μg biotinylated RNA probes (m^6A or non-m^6A labeled) were added to each. The mixture was rotated for 30 min at RT and then incubated for a further 2 h at 4°C. Meanwhile, 200 μL streptavidin-conjugated magnetic beads were washed three times with binding buffer and pre-blocked with BSA (1%) and tRNA (50 μg/mL) for 2 h at 4°C with rotation. The beads were then washed three times with binding buffer, resuspended in 40 μL binding buffer, and transferred into the precleared cell lysate samples. The mixture was then rotated for 2 h at 4°C and washed thoroughly four times with 500 μL binding buffer. Finally, 50 μL 2× SDS loading dye containing DTT was added to the beads, after which the beads were boiled at 95°C, centrifuged immediately, and stored at -80°C for immunoblotting.

Electron microscopy

To prepare the graphene liquid cell, graphene copper foil was cut into 1 × 1 cm squares and flattened with clean glass slides. The EM grid was loaded onto each piece of copper foil, with the carbon film facing down. A small droplet of isopropanol was added to the grid/foil surface and allowed to dry by natural evaporation for up to 30 min. The foil was turned 90° and placed into 0.1 M ammonium persulfate solution for 8 h to allow the copper to be etched away. The excess graphene around the grid was removed, and the grid was gently placed onto clean filter paper with the graphene facing up to permit drying. The sample solution was added to the center of the graphene side of the grid, and the grid was gently placed onto 2 layers of pre-etched, free-floating graphene with the droplet side facing down. The grid was removed and incubated at RT for 20 min to allow liquid pockets to form. Two TEM instruments were employed: a JEM-2100 TEM at the Analytical Instrumentation Center of Peking University and a Talos F200A TEM at Synfuels China Technology Co. Ltd. The JEM-2100 was used with an electron acceleration voltage of 80 keV and an electron dose rate of 10 e•Å−2•s−1, with a temporal resolution of 0.16 s and no lag between frames. The pixel size was 0.36 × 0.36 nm. The Talos F200A was used with an electron acceleration voltage of 200 keV and an electron dose rate of 20–25 e•Å−2•s−1, with a temporal resolution of 0.25 s and no lag between frames. The pixel size was 0.45 × 0.45 nm. All data collected from both TEM experiments were included in the statistical analysis.

Segmentation of the RNA binding interface

GeoBind,[48] a geometric-focused deep learning tool designed to predict protein functional binding sites, was utilized to identify potential RNA binding sites on the surface of the CENPA protein. The full-length CENPA protein structure was predicted using AlphaFold,[88,89] after which the PDB file was uploaded to the GeoBind website (http://www.zpliulab.cn/GeoBind/) with the ligand type set as RNA.[90] NucleicNet[49] was then employed to predict the binding sites on the CENPA protein surface.

Prediction of CENPA-m^{6}A-RNA binding sites

The X-ray co-crystal structure of CENPA (PDB ID: 3NQU)[91] was downloaded from the Protein Data Bank (https://www.rcsb.org/). The structure-based computational framework NucleicNet[49] was used to predict the binding preferences of RNA constituents, including phosphate, ribose, A (Adenine), U (Uracil), C (Cytosine), and G (Guanine), on the surface of the CENPA protein. The "Protein Surface Analysis" module was used to predict the top m^{6}A binding sites in various CENPA structures, including the $(CENPA/H4)_2$ heterotetramer and CENPA/H4 heterodimer.

Validation of CENPA-m^{6}A-RNA binding sites

Molecular docking was applied to evaluate the interaction between the CENPA protein and RNA. The HDOCK server[92] (http://hdock.phys.hust.edu.cn/), which incorporates a hybrid algorithm of template-based modeling and *ab initio* free docking, was selected to simulate CENPA/RNA complexes and calculate the associated docking scores. The RNA structure was predicted using the 3dRNA/DNA Web Server (http://biophy.hust.edu.cn/new/3dRNA).[93] For docking purposes, the CENPA/H4 heterodimers (with the L61D and R63A mutations and prototype established by the point mutation function in the Pymol software) were designated as receptors, and the RNA probes (m^{6}A-modified and prototype) were set as the ligands. Binding site information: receptor binding site residue(s) 61, 63: A; ligand binding site residue(s) 25: A.

Cross-species conservation of the CENPA

The amino acid sequences of CENPA across different species were downloaded from the UniProt database (https://www.uniprot.org), and multiple sequence alignment was performed using the T-Coffee tool.[94]

TUNEL assay

Cells were fixed with 4% paraformaldehyde for 15 min and subsequently permeabilized with 0.5% Triton™ X-100 for a further 10 min. The TUNEL assay was then performed using the DeadEnd™ Fluorometric TUNEL System Kit (Promega, G3250) according to the manufacturer's instructions. Flow cytometry was performed on a CytoFLEX instrument (Beckman), and data were analyzed using the FlowJo_V10 software.

Colony formation assay

A total of 100 cells per well were seeded in 6-well culture dishes. After 7-14 days, the culture medium was removed and the cells were washed twice with PBS, fixed with 4% paraformaldehyde for 15 min, stained with 0.1% crystal violet (in 25% methanol) for 20 min, washed with water, and dried. The colonies were counted manually.

Cell proliferation assay

A total of 5,000 cells per well were seeded in a 96-well plate. Cell proliferation was determined at various time points using a Cell Counting Kit-8 (CCK8, Meilun) according to the manufacturer's protocol.

Drug screening and IC_{50} measurement

A375 cells were incubated with either DMSO or METTL3 inhibitor STM2457, followed by treatment with 16 different agents targeting centromere-interfering[54,55,95–100] (AZD1152, Rigosertib, AZD-7762, AZD-5438, Flavopiridol, SNS-032, Tozasertib, SB-743921) or DNA damage[101–108] (AZD1390, Mitoxantrone, 9-amino-CPT, Amsacrine, Adavosertib, Acelarin, Amonafide, BAY-1895344). Details regarding the names of the drugs and the the target genes have been summarized in Table S3. Cell viability was evaluated using the CCK8 method after incubation the cells with 5μM of each compound and 5μM of STM2457 for 24 hours, following the manufacturer's protocol. The IC_{50} values were measured based on a gradient treatment (0, 0.15625, 0.3125, 0.625, 1.25, 2.5, and 5.0 μM) of AZD1152 and Tozasertib in combination with reduced centromere RNA methylation by *METTL3* knockdown or dCas13b-FTO targeting, or with *CENPA* knockdown followed by overexpression of either *wt*CENPA or *mu*CENPA. Data were analyzed using GraphPad Prism software, and the IC_{50} values were calculated from the dose-response curve visualized using nonlinear regression (curve fitting). Drug sensitivity was evaluated by the dose-response curve of cell viability and the IC_{50} value.

QUANTIFICATION AND STATISTICAL ANALYSIS

The statistical details and methods are indicated in the figure legends or STAR Methods. Statistical analysis and plots were generated using the GraphPad Prism or R software version 4.2.3 unless otherwise stated. For comparisons between two groups, two-tailed unpaired Student's *t*-tests or Wilcoxon-Mann-Whitney tests were performed. *P* values less than 0.05 were considered significant and exact *p* values are provided for each analysis unless they were exceedingly small (in which case *p* values were represented as a "lower-than" range).

The open-source ImageJ software was used to quantitate the immunoblotting and immunofluorescence data. The normalized intensities, represented as bar graphs, were calculated by comparing the intensity of the proteins of interest to that of GAPDH or H3.

CellPress

Supplemental figures

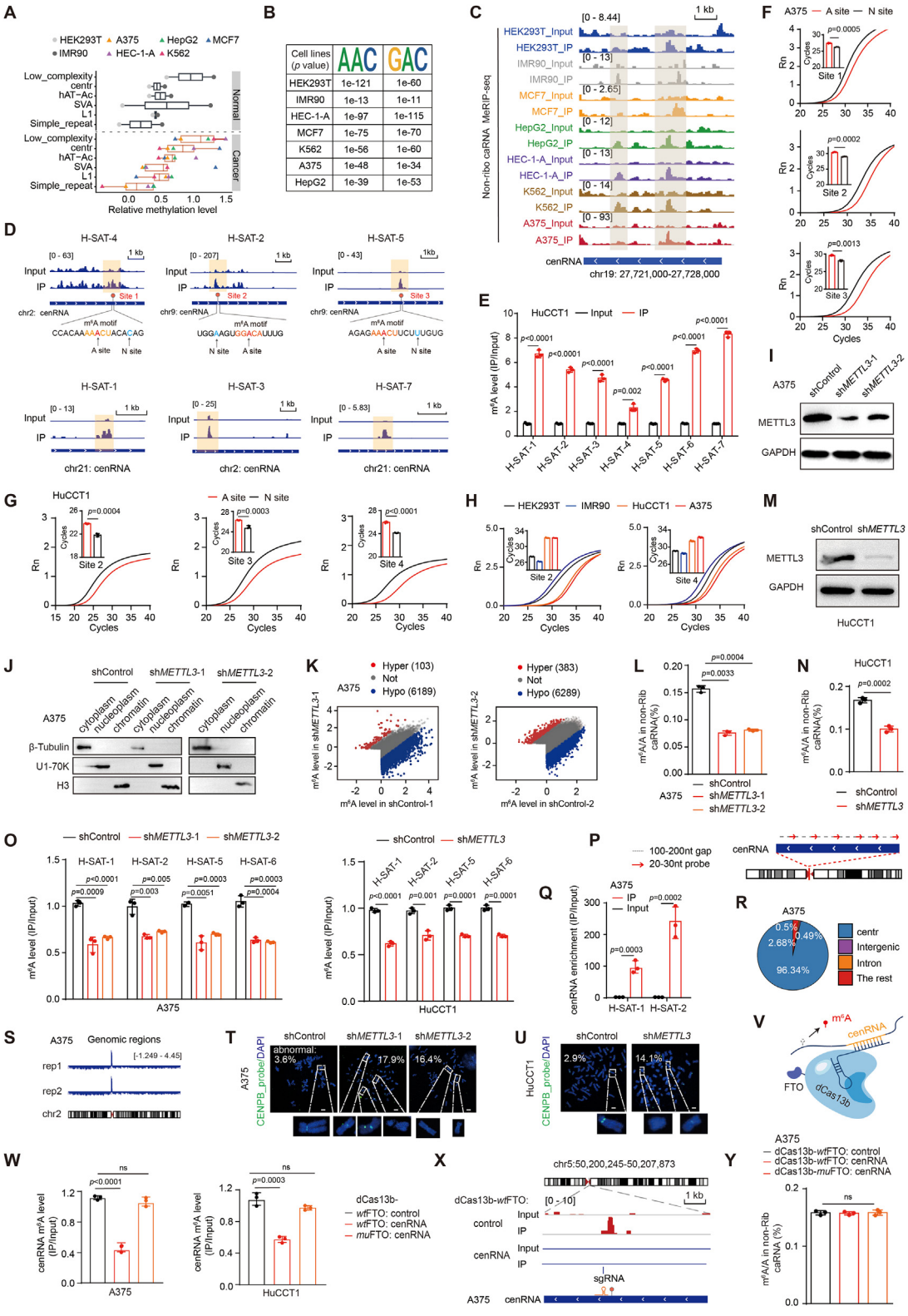

(legend on next page)

Figure S1. The abundant cenRNA methylation safeguard centromeric stability in cancer cells, related to Figure 1

(A) The relative methylation levels of top six repeat families (STAR Methods). Repeat families were ranked based on the mean relative methylation levels in five cancer cell lines. Triangles: cancer cells. Dots: normal cells.

(B) Enriched consensus motifs of methylated cenRNA identified in seven cell lines.

(C) The relatively conserved m^6A peak located on cenRNA in seven cell lines.

(D) m^6A sites and the cenRNA sequences referenced for designing the corresponding primers (bottom).

(E) MeRIP-qPCR assessing the methylation levels of cenRNA using distinct primers in HuCCT1 cells ($n = 3$).

(F and G) The results of single-base elongation- and ligation-based qPCR amplification (SELECT) for the detection of the cenRNA m^6A site at single-base resolution in A375 (F) and HuCCT1 (G) cells ($n = 3$). "A site" denotes the m^6A site, while "N site" represents a non-m^6A-modified site.

(H) The results of SELECT for the detection of the cenRNA m^6A site at single-base resolution in HEK293T, IMR90, HuCCT1, and A375 cell lines ($n = 3$).

(I) *METTL3* knockdown efficiency at the protein level in A375 cells.

(J) Immunoblotting confirming cell fractionation in *METTL3* knockdown and control A375 cells.

(K) m^6A levels in control and *METTL3* knockdown A375 cells. Each point represents a peak. Red: hyper-methylated peaks (m^6A $\log_2$FoldChange > 0.58). Blue: hypo-methylated peaks (m^6A $\log_2$FoldChange < -0.58).

(L) LC-MS/MS quantification of the m^6A/A ratio in non-ribosomal chromatin-associated RNA (caRNA) of control or *METTL3* knockdown A375 cells ($n = 3$).

(M) *METTL3* knockdown efficiency at the protein level in HuCCT1 cells.

(N) LC-MS/MS quantification of the m^6A/A ratio in non-ribosomal caRNA of control or *METTL3* knockdown HuCCT1 cells ($n = 3$).

(O) MeRIP-qPCR assessing the methylation levels of cenRNA using distinct primers in control and *METTL3* knockdown A375 and HuCCT1 cells ($n = 3$).

(P) The position of the probe used for chromatin immunoprecipitation by RNA purification (ChIRP) on centromeric RNA. Red: probes. Gray: gaps.

(Q) The immunoprecipitation efficiency of cenRNA was assessed by RT-qPCR for enriched cenRNAs using the ChIRP method ($n = 3$).

(R) The distribution of cenRNA-binding sites on chromatin based on ChIRP-seq data of control A375 cells.

(S) The chromatin regions bound by cenRNA are predominantly located at the centromeric regions.

(T and U) Representative images of metaphase spread from *METTL3* and control A375 (T) and HuCCT1 (U) cells after fluorescence *in situ* hybridization (FISH) with centromeric (PNA-green) probes. The enlarged section shows lost and ectopic centromeres. Scale bar, 5 μm.

(V) Schematic model of the dCas13b-FTO site-specific demethylation system.

(W) Quantification of cenRNA methylation level via MeRIP-qPCR upon dCas13b-FTO treatment in A375 and HuCCT1 cells ($n = 3$).

(X) One significantly demethylated peak on cenRNA by dCas13b-*wt*FTO targeting in A375 cells with a designed gRNA.

(Y) LC-MS/MS quantification of the m^6A/A ratio in non-ribosomal caRNA from A375 cells upon dCas13b-FTO treatment ($n = 3$).

Error bars indicate mean ± SEM (E–H, L, N, O, Q, W, and Y). ns, not significant (W and Y).

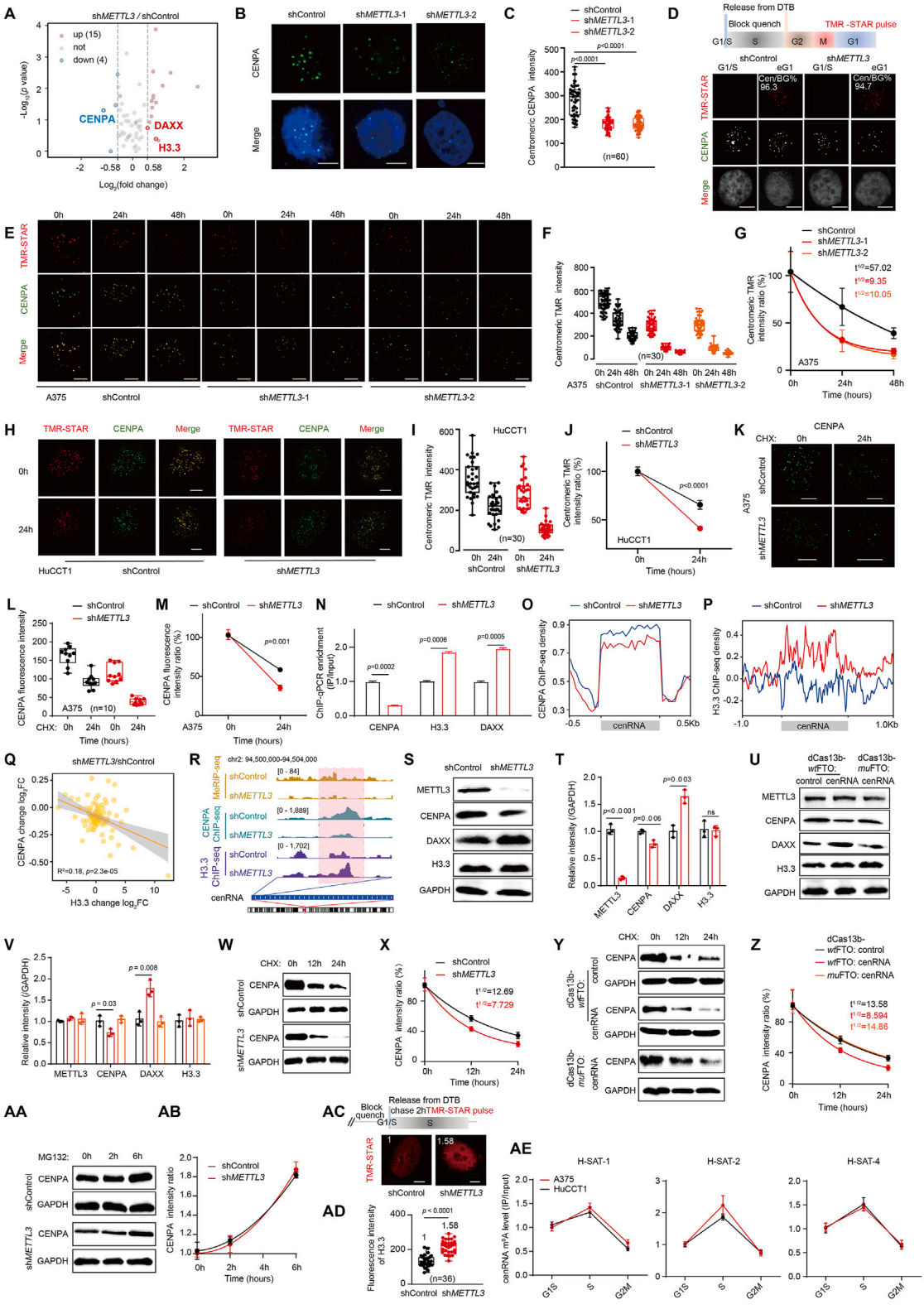

(legend on next page)

Figure S2. Decreased cenRNA methylation induces diminished CENPA nucleosomes and substituted histone H3.3 nucleosomes, related to Figure 2

(A) The changes in protein levels upon *METTL3* knockdown in A375 cells, quantified by mass spectrometry profiling of the chromatin-enriched proteome. Up in red: log_2FoldChange > 0.58; down in blue: log_2FoldChange < −0.58.

(B and C) Representative images depicting the fluorescence intensity of CENPA (green) in control and *METTL3* knockdown A375 cells (B) and quantification using ImageJ (C).

(D) Cells were synchronized, and newly synthesized CENPA protein was labeled with SNAP-tagged CENPA (red) in control and *METTL3* knockdown A375.

(E–J) Cells were synchronized and labeled with SNAP-tagged CENPA (red), total CENPA (green) in control, and *METTL3* knockdown A375 (E) and HuCCT1 (H) cells, the fluorescence intensity of SNAP-tagged CENPA was quantified using ImageJ (F and I), and the corresponding degradation rate was calculated (J) and fitting the curves using GraphPad prism (G).

(K–M) CENPA fluorescence intensity (green) in control and *METTL3* knockdown A375 cells treated with CHX (5 μg/mL) at different time points were examined (K). The fluorescence intensity of CENPA was quantified using ImageJ (L), and the ratio at 24 h relative to 0 h was calculated using GraphPad prism (M).

(N) ChIP-qPCR quantification revealed alterations in CENPA, histone H3.3, and DAXX levels at the centromeric locus between control and *METTL3* knockdown A375 cells (n = 3).

(O and P) The enrichment of CENPA (O) and histone H3.3 (P) at methylated cenRNA-expressing loci in A375 cells upon *METTL3* knockdown, based on MeRIP-seq and ChIP-seq data.

(Q) The correlation between changes in CENPA binding and changes in histone H3.3 binding at methylated cenRNA-expressing loci upon *METTL3* knockdown. These loci were categorized into 100 groups based on the rank of histone H3.3 level fold change upon *METTL3* knockdown. R refers to Pearson's correlation coefficient.

(R) The changes in m^6A levels, CENPA binding, and histone H3.3 binding levels upon *METTL3* knockdown within the genomic location encoding a representative cenRNA.

(S–V) The protein level changes of METTL3, CENPA, DAXX, and histone H3.3 upon *METTL3* knockdown (S) or dCas13b-FTO treatment (U) in A375 cells were detected by western blot and quantified by normalized to GAPDH protein level using ImageJ, respectively (T and V) (n = 3). ns, not significant.

(W–Z) Western blot showing the CENPA protein levels at different time points upon CHX (5 μg/mL) treatment in A375 cells following *METTL3* knockdown (W) or dCas13b-FTO targeting (Y), and the corresponding degradation rate for CENPA was calculated by quantifying the band intensity using ImageJ and fitting the curves using GraphPad prism (X and Z) (n = 3).

(AA and AB) Western blot showing the CENPA protein levels at different time points upon MG132 (5 μM) treatment in A375 cells following *METTL3* knockdown (AA), and the corresponding protein level changes were calculated by quantifying the band intensity and fitting the curves using GraphPad prism (AB) (n = 3).

(AC and AD) Cells were synchronized, and newly synthesized H3.3 histone protein was labeled with SNAP-tagged H3.3 (red) in control and *METTL3* knockdown A375 (AC). The fluorescence intensity of SNAP-tagged H3.3 was quantified using ImageJ (AD).

(AE) MeRIP-qPCR detecting the m^6A modification levels of cenRNA during various cell cycle stages (n = 3).

Scale bar: 5 μm in (B), (D), (E), (H), (K), and (AC). Error bars indicate mean ± SEM (G, J, M, N, T, V, X, Z, AB, and AE). The n shown in the figures represents the total number of cells randomly selected and used for quantifications (C, F, I, L, and AD).

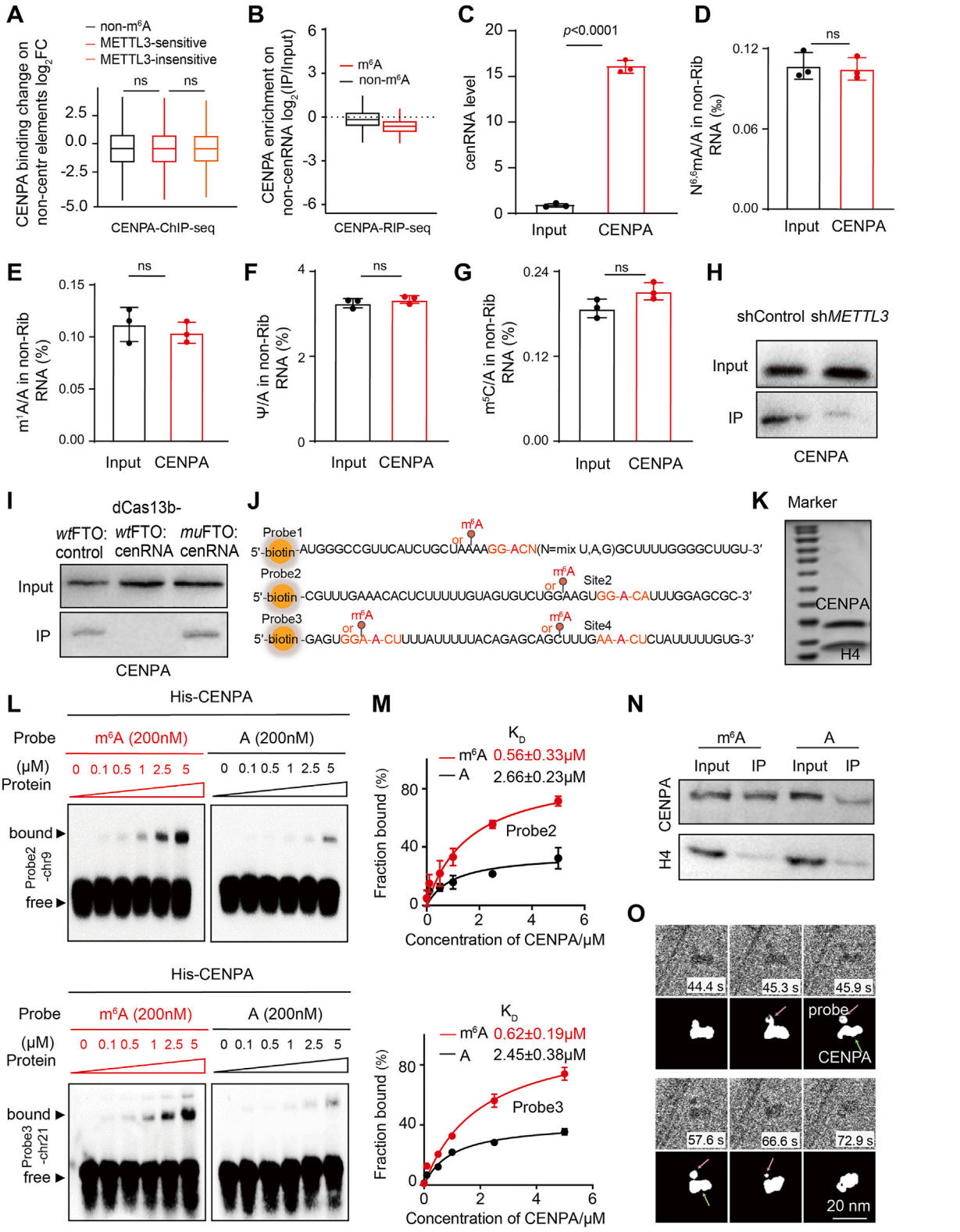

Figure S3. CENPA prefers to bind to methylated cenRNA, related to Figure 3

(A) The fold changes in CENPA binding on distinct RNA species (centr excluded: non-centr) loci upon *METTL3* knockdown. RNAs were categorized into METTL3-sensitive, METTL3-insensitive, or non-methylated groups (STAR Methods). *p* value was calculated by the Wilcoxon test.

(legend continued on next page)

(B) The CENPA enrichment on distinct RNA species (centr excluded: non-centr). RNAs were categorized into methylated (m^6A, log_2[IP/input] > 0.58) or non-methylated (non-m^6A) groups based on our A375 MeRIP-seq data.
(C) The immunoprecipitation efficiency of cenRNAs was assessed by RT-qPCR for enriched cenRNAs using the CENPA-RIP method (n = 3).
(D–G) LC-MS/MS quantitation of the non-ribosomal RNA modification levels in input and CENPA-RIP RNA from A375 cells (n = 3).
(H and I) Western blots of the immunoprecipitated CENPA post cenRNA ChIRP in A375 cells followed by *METTL3* knockdown (H) or dCas13b-FTO treatment (I).
(J) Sequencing information for RNA probes applied for EMSA assay.
(K) *In vitro* His-CENPA protein purification confirmed by colloidal Coomassie brilliant blue staining.
(L and M) EMSA evaluating the binding capacity of CENPA with methylated and unmethylated RNA probes (L). The dissociation constant (K_D) was calculated by quantifying the bands with ImageJ and fitting the binding curves using GraphPad prism (M) (n = 3).
(N) The CENPA pull-down assay was performed by incubating A375 cell lysates with biotinylated RNA probes (m^6A or non-m^6A), and the enriched protein band was subsequently analyzed by immunoblotting.
(O) An exemplary dual-molecular system. At the inception of the video, there is only one particle, presumed to be a composite of CENPA and the RNA probe. At 45.3 s of this video, the RNA probe (denoted by the pink arrow) underwent a morphological transformation reminiscent of budding, culminating in its dissociation from CENPA (denoted by the green arrow) at 45.9 s. Subsequently, the CENPA and RNA probe particles reconverged. At 72.9 s, they fused into one particle.
ns, not significant (A and D–G). Error bars indicate mean ± SEM (C–G and M).

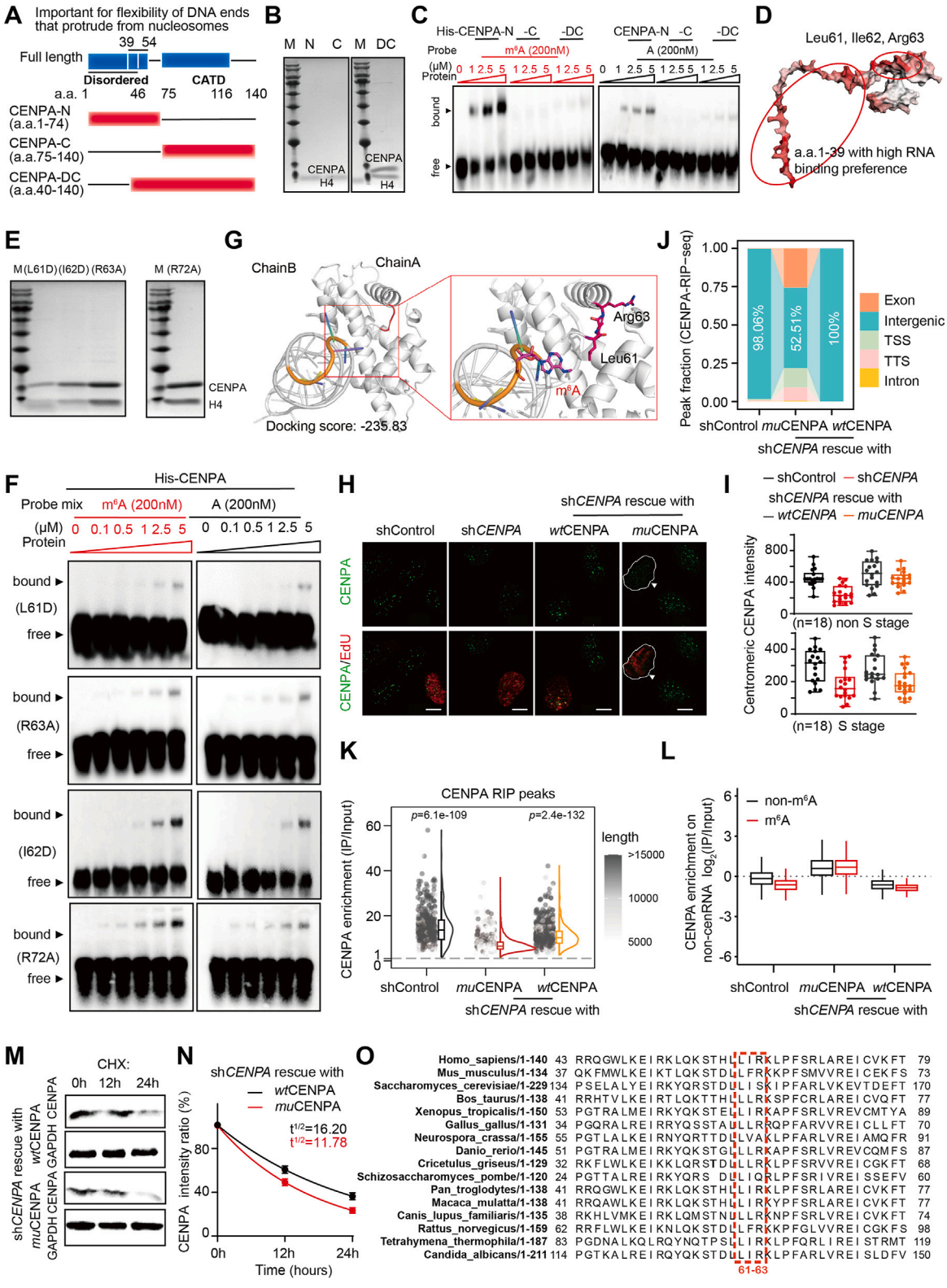

Figure S4. CENPA selectively binds to methylated cenRNA via the amino acids Leu61 and Arg63, related to Figure 4

(A) Diagram depicting various CENPA truncation constructs.

(B) The *in vitro* purification of CENPA-truncated proteins confirmed by colloidal Coomassie brilliant blue staining. CENPA-N: N-terminal; CENPA-C: C-terminal; CENPA-DC: 40–140 amino acids.

(legend continued on next page)

(C) EMSA evaluating the binding capacity of His-tagged CENPA-N, CENPA-C, and CENPA-DC with methylated and unmethylated RNA probes.
(D) Segmentation of the RNA-binding interface. The binding interface on the surface is colored red. The darker color shading represents higher predicted binding preference.
(E) The *in vitro* purification of CENPA mutants with individual sites confirmed by colloidal Coomassie brilliant blue staining.
(F) EMSA evaluating the binding capacity of CENPA with mutation at positions 61, 62, 63, and 72 to methylated and unmethylated RNA probes.
(G) Predicted binding mode of CENPA protein and m^6A-modified RNA. The distance between m^6A site and Leu61 is less than 5 Å, and a hydrophobic interaction is formed between adenine methylation and Leu61.
(H and I) Representative images showing the CENPA fluorescence intensity in control A375 cells, as well as *CENPA* knockdown cells followed by expressing wild-type CENPA (*wt*CENPA) or double-mutant CENPA (*mu*CENPA), which has lost the selectivity for methylated RNA binding (H). CENPA fluorescence intensity by immunofluorescence staining was quantified using ImageJ (I). Scale bar, 5 μm. The *n* shown in the figures represents the total number of cells randomly selected and used for quantifications. The *n* shown in the figures represents the total number of cells randomly selected and used for quantifications.
(J) The distribution of CENPA RIP-seq peaks at distinct genomic regions in control A375 cells, as well as *CENPA* knockdown cells followed by expressing *wt*CENPA or *mu*CENPA.
(K and L) CENPA enrichment on global RIP-seq peaks (K) or distinct RNA species (cenRNA excluded: non-cenRNA) (L) in control A375 cells, as well as *CENPA* knockdown cells followed by expressing *wt*CENPA or *mu*CENPA quantified by CENPA RIP-seq data. Each point represents a peak, with color representing peak length. RNAs were divided into methylated (m^6A, $\log_2$[IP/input] > 0.58) or non-methylated (non-m^6A) groups. *p* values were calculated by Wilcoxon test.
(M and N) CENPA protein levels in the sh*CENPA*-rescued A375 cells expressing *wt*CENPA or *mu*CENPA following treatment with CHX (5 μg/mL) at different time points detected via immunoblotting (M). The corresponding degradation rate for CENPA was calculated by quantifying the band intensity using ImageJ and fitting the curves using GraphPad prism (N) ($n = 3$). Error bars indicate mean ± SEM.
(O) Cross-species conservation of CENPA protein, generated by the T-Coffee tool.

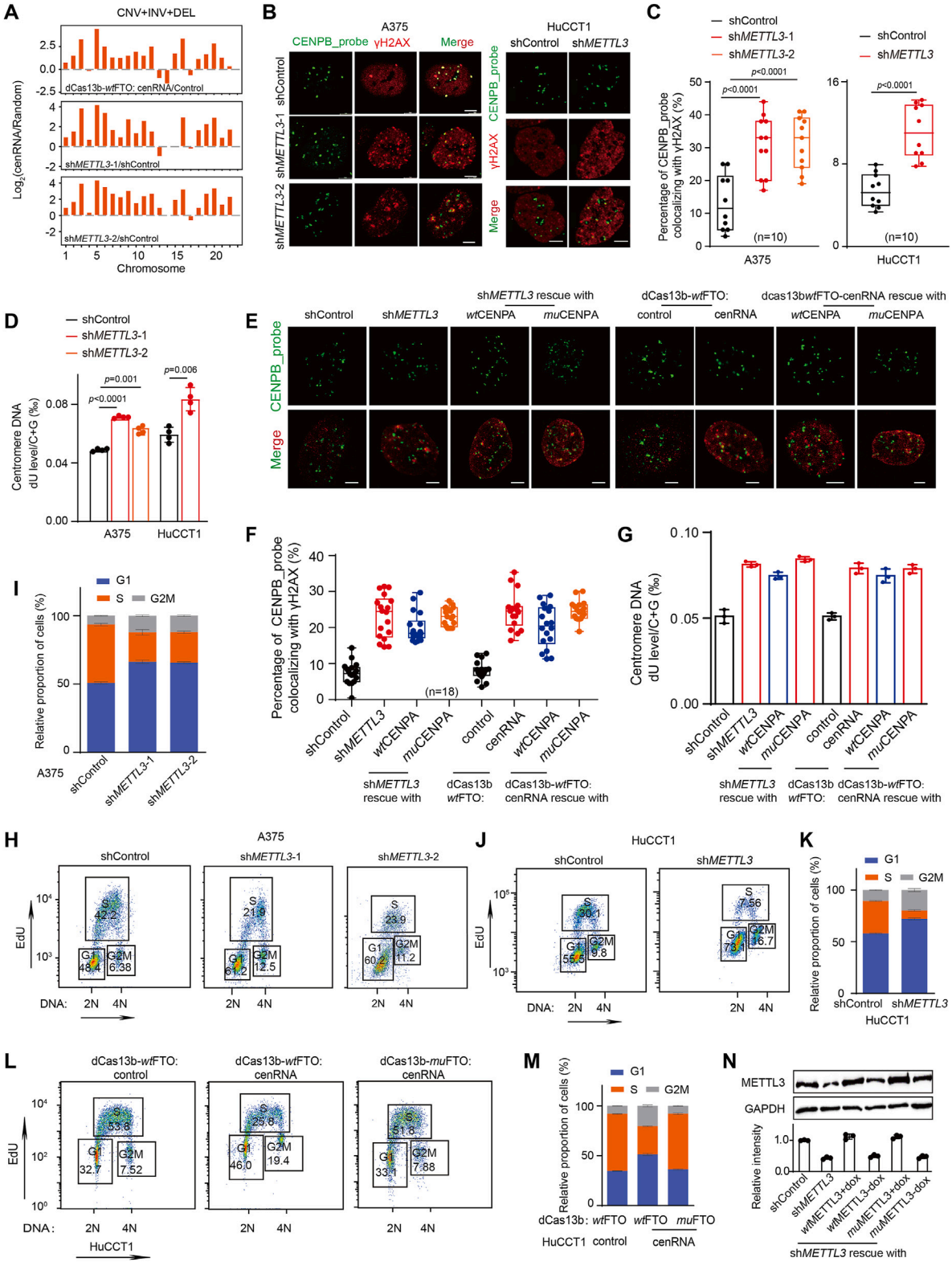

(legend on next page)

Figure S5. Disrupted CENPA-m^{6}A cenRNA interaction increases centromeric instability, related to Figure 5

(A) The centromere instability on each chromosome (log_2[$cenRNA_{mean}$/$Random_{mean}$]), measured by the occurrence of several variation types after either *METTL3* knockdown or dCas13b-FTO treatment, including copy number variations (CNVs) and two structural variation types, inversions (INV) and deletions (DEL). A value greater than 0 indicates increased centromere instability on that chromosome (STAR Methods).

(B and C) Centromeric immunofluorescence (CIF) assays in *METTL3* knockdown and control A375 and HuCCT1 cells. Immunofluorescence staining was carried out using anti-γH2AX antibodies (red), followed by FISH with centromeric (PNA-green) probes (B). The corresponding percentages of γH2AX colocalizing with centromeres were quantified using ImageJ (C).

(D) LC-MS/MS quantifying the dUMP levels of centromeric DNA in control and *METTL3* knockdown A375 and HuCCT1 cell, serving as an indicator of centromere damage (n = 4).

(E and F) CIF in A375 cells with *METTL3* knockdown or dCas13b-FTO treatment followed by overexpressing of *wt*CENPA or *mu*CENPA.

(G) LC-MS/MS quantifying the dUMP levels of centromeric DNA in A375 cells with *METTL3* knockdown or dCas13b-FTO treatment followed by overexpressing of *wt*CENPA or *mu*CENPA (n = 3).

(H–M) Cell cycle distribution was assessed via flow cytometry (H, J, and L), and the proportions of cells in distinct cell cycle phases were quantified (I, K, and M) in *METTL3* knockdown A375 and HuCCT1 cells (H–K) or dCas13b-FTO treatment A375 cells (L and M).

(N) METTL3 protein level in *METTL3* knockdown A375 cells and its rescue with wild-type and catalytically inactive mutant METTL3. The bar graph below represents the protein level quantified using Image J.

Error bars indicate mean ± SEM (D, G, I, K, M, and N). The n shown in the figures represents the total number of cells randomly selected and used for quantifications (C and F). Scale bar: 5 μm in (B) and (E).

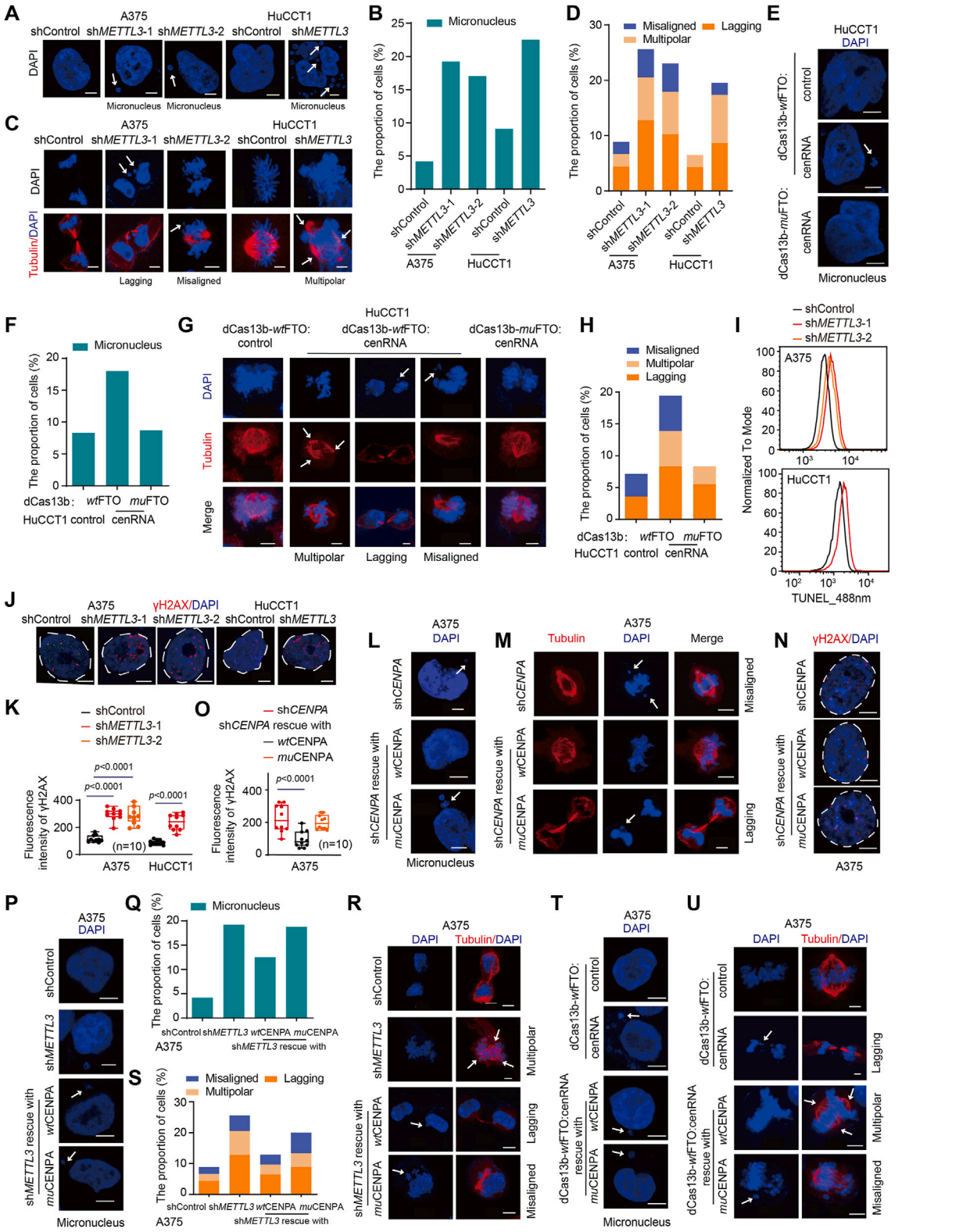

Figure S6. The interaction between CENPA and m^{6}A-cenRNA protects genomic stability, related to Figure 6

(A and B) Immunofluorescence analysis in A375 and HuCCT1 cells upon *METTL3* knockdown. Cells were stained with DAPI to perform a micronucleus assay (A) and quantification of cells with micronuclei (B) shown in (A). The arrows indicated the micronuclei of cell.

(legend continued on next page)

(C and D) Immunofluorescence analysis in A375 and HuCCT1 cells upon *METTL3* knockdown. Cells were stained with anti-tubulin (red) and DAPI (blue) to visualize mitotic defects (C) and quantification of cells with different types of chromosome defects (D) shown in (C). The arrows indicated the specific types of mitotic abnormalities.
(E and F) Immunofluorescence analysis in HuCCT1 cells upon dCas13b-FTO treatment. Cells were stained with DAPI to perform a micronucleus assay.
(G and H) Immunofluorescence analysis in HuCCT1 cells upon dCas13b-FTO treatment. Cells were stained with anti-tubulin (red) and DAPI (blue) to visualize mitotic defects.
(I) Assessment of DNA damage by TUNEL assay in A375 and HuCCT1 cells upon *METTL3* knockdown.
(J and K) The fluorescence intensity of γH2AX was detected (J) and quantified (K) in both control and *METTL3* knockdown A375 and HuCCT1 cells.
(L and M) Immunofluorescence analysis in *CENPA* knockdown A375 cells and rescued with *wt*CENPA or *mu*CENPA. Cells were stained with anti-tubulin antibodies (red) and DAPI (blue) to visualize mitotic defects (M) or stained with DAPI to perform a micronucleus assay (L).
(N and O) Detection of γH2AX fluorescence intensity (N) and its quantification (O) in *CENPA* knockdown A375 cells and those rescued with *wt*CENPA or *mu*CENPA.
(P and Q) Immunofluorescence analysis in A375 cells with *METTL3* knockdown followed by overexpressing of *wt*CENPA or *mu*CENPA. Cells were stained with DAPI to perform a micronucleus assay.
(R and S) Immunofluorescence analysis in A375 cells with *METTL3* knockdown followed by overexpressing of *wt*CENPA or *mu*CENPA. Cells were stained with anti-tubulin (red) and DAPI (blue) to visualize mitotic defects.
(T and U) Immunofluorescence analysis in A375 cells with dCas13b-FTO treatment followed by overexpressing of *wt*CENPA or *mu*CENPA. Cells were stained with anti-tubulin antibodies (red) and DAPI (blue) to visualize mitotic defects (U) or stained with DAPI to perform a micronucleus assay (T).
Scale bar: 5 μm in (A), (C), (E), (G), (J), (L)–(N), (P), (R), (T), and (U). The *n* shown in the figures represents the total number of cells randomly selected and used for quantifications (K and O).

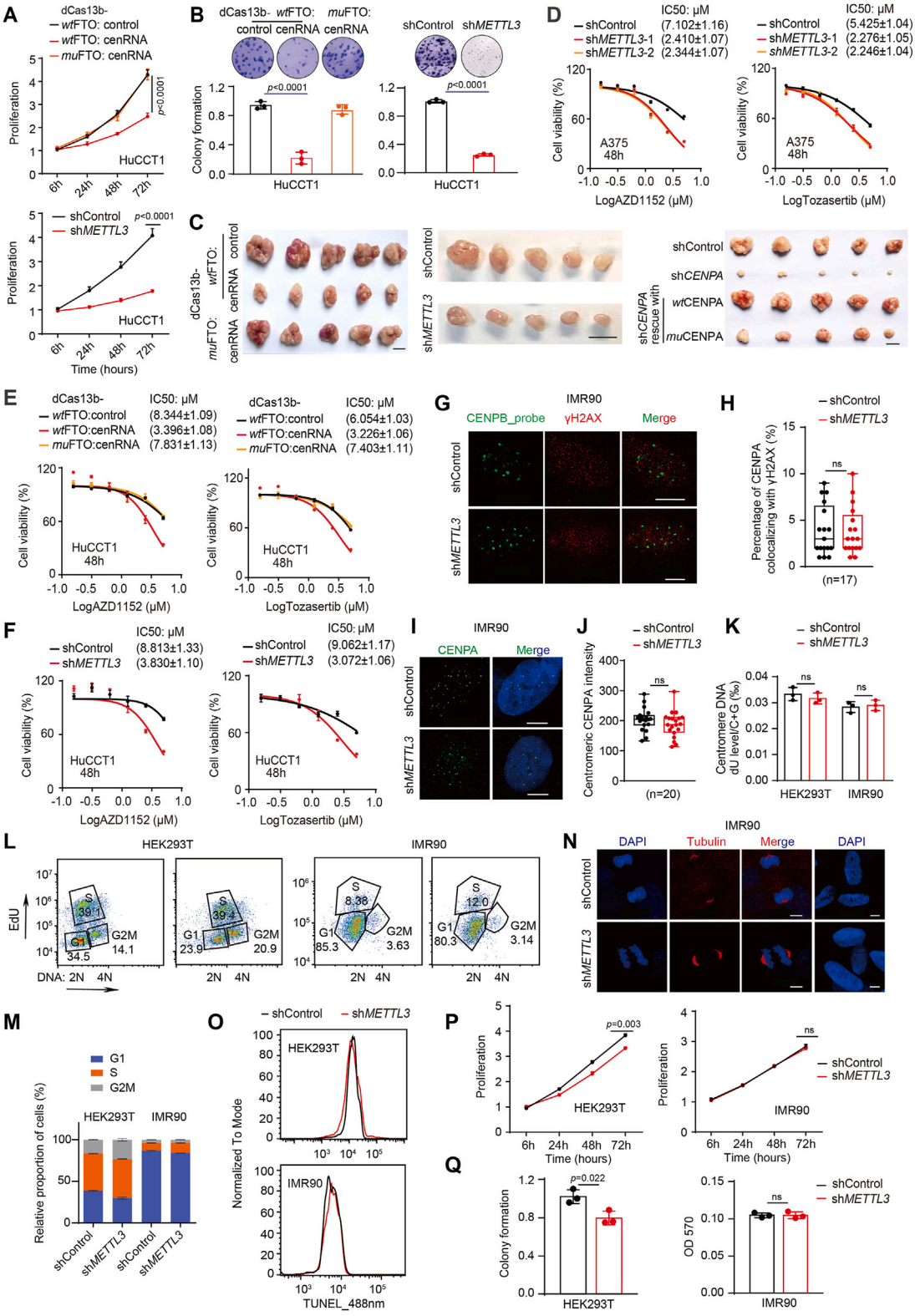

Figure S7. Methylated cenRNA had minimal impact on normal cells, related to Figure 7

(A and B) The cell viability and clonogenic potential evaluated by CCK-8 (A) and crystal violet staining (B) assay in HuCCT1 cells with dCas13b-FTO treatment or *METTL3* knockdown (n = 3).

(legend continued on next page)

(C) A375 cells with dCas13b-FTO treatment, *METTL3* knockdown, or CENPA knockdown followed by overexpressing *wt*CENPA or *mu*CENPA were subcutaneously injected into the flank of nude mice. Tumors were excised and photographed. Scale bar, 0.8 cm.
(D) Dose-response curves and corresponding half-maximal inhibitory concentration (IC_{50}) values for AZD1152 and Tozasertib treatment 48 h in A375 cells upon *METTL3* knockdown ($n = 3$).
(E and F) Dose-response curves and corresponding IC_{50} values for AZD1152 and Tozasertib treatment 48 h in HuCCT1 cells following dCas13b-FTO targeting (E) or *METTL3* knockdown (F) ($n = 3$).
(G and H) CIF in *METTL3* knockdown and control IMR90 cells. The cells were stained with anti-γH2AX antibodies (red) and subject to FISH using centromeric (PNA-green) probes (G). The corresponding percentages of γH2AX colocalization with centromeres are present in (H).
(I and J) Representative images illustrating the fluorescence intensity of CENPA (green) in both control and *METTL3* knockdown IMR90 cells via immunofluorescence staining (I) and the corresponding quantification using ImageJ (J).
(K) LC-MS/MS quantification of dUMP levels in centromeric DNA extracted from both control and *METTL3* knockdown HEK293T and IMR90 cells ($n = 3$).
(L and M) Cell cycle distribution assessed using flow cytometry (L), and the proportions of cells in distinct cell cycle phases quantified for HEK293T and IMR90 cells upon *METTL3* knockdown (M) ($n = 3$).
(N) Immunofluorescence analysis conducted on IMR90 cells following *METTL3* knockdown compared with control cells. The cells were stained with anti-tubulin antibodies (red) and DAPI (blue) to visualize mitotic defects or stained with DAPI only to perform a micronucleus assay.
(O) DNA damage assessed by TUNEL assay in control and *METTL3* knockdown HEK293T and IMR90 cells.
(P and Q) The cell proliferation and growth capacity measured by CCK-8 (P) and crystal violet staining (Q) assay in HEK293T and IMR90 cells with *METTL3* knockdown ($n = 3$).
Error bars indicate mean ± SEM (A, B, D–F, K, M, P, and Q). Scale bar: 5 μm in (G), (I), and (N). ns, not significant (H, J, K, P, and Q). The *n* shown in the figures represents the total number of cells randomly selected and used for quantifications (H and J).